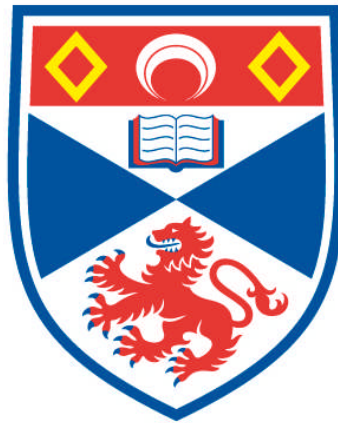


**PHOTONIC CRYSTAL CAVITY BASED ARCHITECTURE FOR
OPTICAL INTERCONNECTS**

Kapil Debnath

**A Thesis Submitted for the Degree of PhD
at the
University of St Andrews**



2013

**Full metadata for this item is available in
Research@StAndrews:FullText
at:**

<http://research-repository.st-andrews.ac.uk/>

Please use this identifier to cite or link to this item:

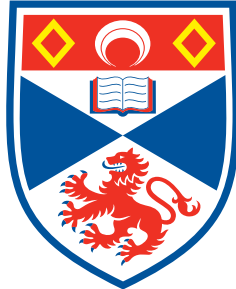
<http://hdl.handle.net/10023/3870>

This item is protected by original copyright

Photonic Crystal Cavity Based Architecture for Optical Interconnects

Kapil Debnath

Thesis submitted for the degree of
Doctor of Philosophy



University of
St Andrews

School of Physics & Astronomy

University of St Andrews

April 2013

for Amrita

Declarations

I, Kapil Debnath, hereby certify that this thesis, which is approximately 40000 words in length, has been written by me, that it is the record of work carried out by me and that it has not been submitted in any previous application for a higher degree.

I was admitted as a research student in October 2009 and as a candidate for the degree of Doctor of Philosophy in October 2009; the higher study for which this is a record was carried out in the University of St Andrews between 2009 and 2013.

Date:.....

Signature of candidate:.....

I hereby certify that the candidate has fulfilled the conditions of the Resolution and Regulations appropriate for the degree of Doctor of Philosophy in the University of St Andrews and that the candidate is qualified to submit this thesis in application for that degree.

Date:.....

Signature of Supervisor:.....

In submitting this thesis to the University of St Andrews I understand that I am giving permission for it to be made available for use in accordance with the regulations of the University Library for the time being in force, subject to any copyright vested in the work not being affected thereby. I also understand that the title and the abstract will be published, and that

a copy of the work may be made and supplied to any bona fide library or research worker, that my thesis will be electronically accessible for personal or research use unless exempt by award of an embargo as requested below, and that the library has the right to migrate my thesis into new electronic forms as required to ensure continued access to the thesis. I have obtained any third-party copyright permissions that may be required in order to allow such access and migration, or have requested the appropriate embargo below.

The following is an agreed request by candidate and supervisor regarding the electronic publication of this thesis:
Access to printed copy and electronic publication of thesis through the University of St Andrews.

Date:.....

Signature of Candidate:.....

Signature of Supervisor:.....

Acknowledgments

I am grateful to a number of people for their guidance and assistance during my PhD and here I would like to take the opportunity to express my deepest gratitude to them.

First of all, I would like to extend my sincere appreciation to my supervisor Prof. Thomas Krauss for giving me the opportunity to work in his research group. I have learned a tremendous amount from his roles as both a scientist and a leader. His openness, energy and enthusiasm inspired me for the last three and half years. I am also highly indebted to Dr William Whelan-Curtin (Liam O’Faolain) for sharing his technological expertise and constant flow of innovative ideas and thank him for spending an enormous amount of time with me over the past years.

A special thanks goes to Dr Karl Welna for introducing me to his “dispersion adapted” cavity design and helping me with simulation software at numerous occasions. I am also thankful to Dr Frederic Gardes from University of Southampton for helping me with device design and measurement and Dr Kieran Deasy from University of Sheffield for depositing silicon nitride.

Thanks to the EPSRC project UK Silicon Photonics for funding of my work.

I would like to thank all my colleagues and friends from the microphotonics research group who made my time at St Andrews as enjoyable and rewarding as it was. In particular, I would like to thank Dr Sebastian Kosmeier, Dr Mark Scullion, Bryan O’regan, and Annett Klemm. My special appreciation goes to Mr Steve Balfour, Mr Callum Smith and Mr George Robb for keeping the clean room up and running under any circumstances.

On a more personal level, I would like to thank my parents and my sister for all their love and support.

Finally, I express my special gratitude to my wife Amrita, for believing in me and encouraging me for all my endeavors.

List of Publications

Journal Papers

- **K. Debnath**, L. O’Faolain, F. Y. Gardes, A. G. Steffan, G. T. Reed, and T. F. Krauss, “Cascaded modulator architecture for WDM applications,” *Optics Express* 20, 27420-27428 (2012).
- **K. Debnath**, K. Welna, M. Ferrera, K. Deasy, D. G. Lidzey, and Liam O’Faolain, “Highly efficient optical filter based on vertically coupled photonic crystal cavity and bus waveguide,” *Optics Letters* 38, 154-156 (2013).
- **K. Debnath**, F. Y. Gardes, A. P. Knights, G. T. Reed, T. F. Krauss, and L. O’Faolain, “Dielectric waveguide with integrated all-silicon photodiodes for telecommunication wavelength,” *Applied Physics Letters* 102, 171106 (2013).

Conference Proceedings

- **K. Debnath**, L. O’Faolain, and T. F. Krauss, “Slowlight enhanced photonic crystal modulators,” *Group IV Photonics (GFP)*, 98-100 (2011).
- **K. Debnath**, L. O’Faolain, F. Y. Gardes, D. Thomson, G. T. Reed, and T. F. Krauss, “Low insertion loss modulator based on a vertically coupled photonic crystal resonator,” *Proc. SPIE 8267*, 82670I (2012).
- **K. Debnath**, K. Welna, M. Ferrera, K. Deasy, D. Lidzey, T. F. Krauss, and L. O’Faolain, “Highly efficient coupling between a monolithically integrated Photonic Crystal Cavity and a Bus Waveguide,” *Proc. of SPIE 8264*, 82640F-1 (2012).
- **K. Debnath**, K. Welna, M. Ferrera, K. Deasy, D. Lidzey, and L. O’Faolain, “Highly efficient coupling between a nanocavity and monolithic bus waveguide,” *Group IV Photonics (GFP)*, 102-104 (2012).
- **K. Debnath**, L. O’Faolain, F. Gardes, D. Thomson, J. Gellata, A. P. Knights, G. T. eed, and T. F. Krauss, “Photonic Crystal Cavity Based WDM Components,” *Group IV Photonics (GFP)*, 270-272 (2012).

-
- L. O’Faolain, **K. Debnath**, F. Y. Gardes, A. G. Steffan, E. Tasyurek, D. A. B. Miller, G. T. Reed, and T. F. Krauss, “Scalable optical transmitter and receiver based on cascaded nanoresonator modulators and multiwavelength laser,” Proc. of SPIE 8630, 86300P (2013).

Conferences Attended

- Photonics 2010, Guwahati, India Oral Presentation Title: “Broadband electro-optic photonic crystal modulator”
- GFP 2011, 8th IEEE international conference on group IV Photonics, London, UK Poster Presentation Title: “Slowlight Enhanced Photonic Crystal Modulators”
- Photonics West 2012, San Francisco, USA Oral Presentation Title: “Highly efficient coupling between a Photonic Crystal Cavity and a Bus waveguide”
- Photonics West 2012, San Francisco, USA Oral Presentation Title: “Photonic Crystal Cavity Based Cascaded Modulators for WDM Interconnects”
- GFP 2012, 9th IEEE international conference on group IV Photonics, San Diego, USA Poster Presentation Title: “Photonic Crystal Cavity Based Cascaded Modulators for WDM Interconnects”
- GFP 2012, 9th IEEE international conference on group IV Photonics, San Diego, USA Poster Presentation Title: “Highly efficient coupling between a nanocavity and monolithic bus waveguide”
- Photon12, Durham, UK Poster Presentation Title: “Photonic crystal cavity based cascaded modulators and demodulators for a WDM system”

Patent

- Application: The University of St Andrews, L. O’Faolain, T. F. Krauss, **K. Debnath**, K. Welna, “Wave vector matched resonator and bus waveguide system,” Application No. PCT/GB2012/000618.

Abstract

Today's information and communication industry is confronted with a serious bottleneck due to the prohibitive energy consumption and limited transmission bandwidth of electrical interconnects. Silicon photonics offers an alternative by transferring data optically and thereby eliminating the restriction of electrical interconnects over distance and bandwidth. Due to the inherent advantage of using the same material as that used for the electronic circuitry, silicon photonics also promises high volume and low cost production plus the possibility of integration with electronics.

In this thesis, I introduce an all-silicon optical interconnect architecture that promises very high integration density along with very low energy consumption. The basic building block of this architecture is a vertically coupled photonic crystal cavity-waveguide system. This vertically coupled system acts as a highly wavelength selective filter. By suitably designing the waveguide and the cavity, at resonance wavelength of the cavity, large drop in transmission can be achieved. By locally modulating the material index of the cavity electrically, the resonance wavelength of the cavity can be tuned to achieve modulation in the transmission of the waveguide. The detection scheme also utilizes the same vertically coupled system. By creating crystal defects in silicon in the cavity region, wavelength selective photodetection can be achieved. This unique vertical coupling scheme also allows us to cascade multiple modulators and detectors coupled to a single waveguide, thus offering huge channel scalability and design and fabrication simplicity.

During this project, I have implemented this vertical coupling scheme to demonstrate modulation with extremely low operating energy (0.6 fJ/bit). Furthermore, I have demonstrated cascadeability and multichannel operation by using a comb laser as the source that simultaneously drives five channels. For photodetection, I have realized one of the smallest wavelength selective detector with responsivity of 0.108 A/W at 10 V reverse bias with a dark current of 9.4 nA. By cascading such detectors I have also demonstrated a two-channel demultiplexer.

Contents

1	Optical Interconnects: Introduction and Background	1
1.1	Introduction	1
1.2	Interconnection dilemma	2
1.3	Migration to optical interconnects: motivations and challenges	5
1.4	Silicon photonics	7
1.4.1	Materials for silicon photonics	7
1.4.1.1	Silicon on insulator	7
1.4.1.2	Polycrystalline and amorphous silicon	10
1.4.1.3	Silicon nitride	10
1.4.1.4	Germanium	10
1.4.2	Passive optical components	10
1.4.3	Off-chip coupling	11
1.4.4	Modulation	13
1.4.5	Photodetection	16
1.4.6	WDM system on silicon	16
1.5	Aim of the Thesis	18
2	Fabrication Tools and Techniques	23
2.1	Introduction	23
2.2	Photolithography	23
2.3	Electron beam lithography	24
2.4	Reactive ion etching	28
2.5	Lift-off and metal evaporation	30
2.6	Summary	31
3	Photonic Crystal Cavity Based Optical Filter	33
3.1	Introduction	33
3.2	Photonic crystal	34
3.2.1	Origin of photonic bandgap: a 1D example	35
3.2.2	Two dimension photonic crystal	37
3.2.3	Localization of light using defects	37
3.3	High quality factor photonic crystal cavity	40
3.3.1	Gentle mode confinement	40
3.3.2	Gentle confinement in an Ln type cavity	41
3.3.3	Line defect photonic crystal cavity	44
3.3.3.1	Heterostructure cavity	44
3.3.3.2	Linewidth modulated cavity	44

3.3.3.3	Dispersion adapted cavity	46
3.3.4	Oxide clad photonic crystal cavity	47
3.4	Coupled waveguide-resonator system	49
3.4.1	Two-port analysis of a side coupled system	50
3.4.2	Limitations with conventional side coupling approach in photonic crystal	52
3.5	Vertical coupling	53
3.5.1	Condition for high coupling efficiency	54
3.5.2	Device fabrication	57
3.5.3	Measurement setup	59
3.5.4	Transmission characterization	60
3.5.5	Effect of k-space overlap on extinction ratio	62
3.5.6	Multiplexing	65
3.6	Discussion	66
4	Cascaded Modulator Architecture	69
4.1	Introduction	69
4.2	Wavelength tuning in photonic crystal cavities	70
4.3	Design and fabrication	73
4.3.1	Design consideration	73
4.3.2	Mask Design	74
4.3.3	Fabrication	77
4.4	Characterization setup	79
4.4.1	Optical setup	79
4.4.2	Electrical setup	80
4.5	Optical characterization	81
4.6	Electro-optic modulation	82
4.6.1	DC characterization	82
4.6.2	High speed measurement	84
4.6.3	Multi-wavelength operation using comb laser	85
4.7	Discussion	86
5	Cascaded Detector Architecture	89
5.1	Introduction	89
5.2	Sub-bandgap detection in silicon	90
5.3	Device design and fabrication	92
5.3.1	Design consideration	92
5.3.2	Mask design and fabrication	94
5.4	Characterization setup	95
5.5	Measurements	96
5.5.1	Effect of power and bias voltage	97
5.5.2	Demultiplexing	100
5.6	Discussion	100
6	Conclusions	103
6.1	Thesis summary	103
6.2	Future directions	106
6.2.1	Optimization of the filter response	106

CONTENTS

6.2.2	Optimization of the modulator design	107
6.2.3	Thermal stability	107
6.2.4	Optimization of the detector design	108
6.2.5	Tunable Lasers and directly modulated laser	110
	Bibliography	113
	List of Figures	127
	List of Tables	137

Chapter 1

Optical Interconnects: Introduction and Background

1.1 Introduction

In the last few decades, we have seen an unprecedented advancement in information and communication technology; its pervasive growth has influenced the shape of our society in a fundamental way. A major portion of this growth is due to the expansion of the internet. The emergence of Google, Facebook, Skype and so many other internet services has changed the way we interact and communicate with each other, share or access information, work collaboratively irrespective of the geographic location, thus making the world a true “global village” [1]. Besides the obvious social impact, the internet now also contributes 3.4% to the GDP in thirteen major countries [2]. Banks, companies, universities, and governments now require large and secure data centers connected to secure networks. At the consumer level, computers, tablets, mobile phones, HD TV and others have become an integral part of our daily life. While many of these gadgets have their own practical functions, most technological improvements today seem to revolve around interconnectivity. As a result, today’s information and communication industry is seeing increased demand for data transfer, internet downloads, online applications, video sharing and storage and the Internet has become a super-massive repository of data with ever more growth in sight. From the year 2005 to 2012, the number of worldwide internet users has almost tripled and by June 2012, it was estimated that over 2.4 billion people (34.3% of the world population) have access to the internet [3]. Figure 1.1 shows the internet penetration rates for different geographic regions. While not without negative aspects, the net effect of the internet has, undeniably, been a dramatic improvement in the standard of living. So much so that broadband access is being proposed as a basic human right [4]. A key challenge for the 21st century is therefore to provide billions of people with an efficient means to access, move and manipulate, to what has become a huge volume of information.

The internet experience is now, somewhat invisibly, built around data centers, huge warehouses of computers connected together, with their effi-

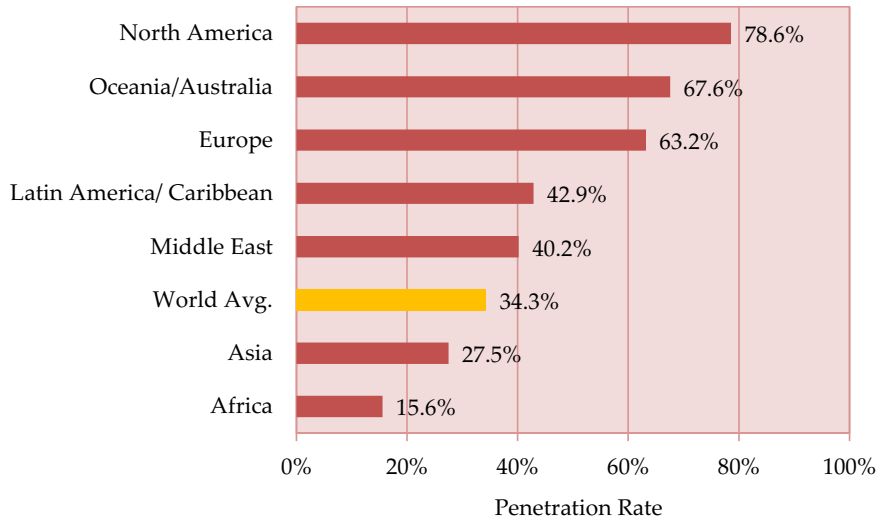


Figure 1.1 – World internet penetration rates by geographic regions [3].

cient operation being crucial. Two examples illustrate this: it has been estimated that a single internet search is passed through 5000 computers and may consume $1/10^{\text{th}}$ of the energy required to boil a kettle [5] and that a 100 ms delay in page loading decreases Amazon’s sales by 1 % [6]. These facts highlight both the social and economic implications—the power consumed by Information Technology now matches that consumed by the airline industry and is growing rapidly; the cost of the energy consumed over three years is greater than the capital cost of a datacenter. Therefore, in order to meet future demands, there is a need for faster and more energy efficient computers and communication networks.

1.2 Interconnection dilemma

Since the birth of integrated electronics, the performance of microprocessors has been enhanced by scaling down the size of the transistors inside the microprocessors. Thus, as each successive generation of photolithographic technology has yielded smaller feature size, it also has enabled an overall faster microprocessor. This trend of scaling in device size and performance was predicted by Gordon Moore in 1965, then director of Fairchild Semiconductor’s Research and Development Laboratories, and has become known as Moore’s law. According to Moore’s law, the on-chip transistor density doubles approximately every two years [7]. Over the last five decades, this prediction has remained a guideline to which the electronics industries adhere impressively in order to meet market demand and to take advantage of the economies of scale achievable by packing more devices per chip [8].

According to the “universal scaling” rule, with a scaling factor of α (<1), the density of transistors within a unit area scales up by $1/\alpha^2$, while the

switching delay and power consumption for individual transistors scales down by the same factor α . All of these consequences are desirable and led to a performance enhancement of each new generation of microprocessors. This scaling of device size, however, imposes a negative impact on the performance of the interconnect, which is a complex network of metal wires transporting data and distributing the clock signal within and outside the microprocessor. Today, a typical microprocessor employs over 10 km of metal tracks in a three dimensional network which is often spread over number of separate layers. Metal tracks in different layers have different thicknesses ranging from many micrometers on the top layers to tens of nanometers at the device level, which provides access to nanometer-scale transistors in silicon. Figure 1.2a illustrates the electrical interconnect system for the 45 nm technology node, where 9 metal layers are used [9]. As more and more transistors are packed into a given area on a computer chip, the interconnect system is also getting more and more complicated and imposing a serious bottleneck for the further advancement of IC technology.

In 1984, Goodman et al. suggested that if the interconnect network scales down by α in all the three dimensions, then the RC time constant and delay caused by the interconnects will remain constant [12]. Since the microprocessor chip size and the distance which the interconnect system needs to cover will most likely remain unchanged, the interconnect delay will then increase as transistors continue to scale down. Figure 1.2b shows the relative delay of gate, local interconnects and global interconnects for different technology nodes [10]. Relative delays due to the gate and the local interconnects reduce as the technology node gets smaller, while the global interconnect delay increases superlinearly as the transistors scale down. The discrepancy between the gate delay and the global interconnect delay also imposes further complexities in the chip architectures for design engineers [13].

In addition to delay, the transmission bandwidth of the existing interconnect is another performance bottleneck. The bandwidth of an electrical wire is proportional to its cross section and inversely proportional to the square of its length and is essentially decided by the aspect ratio of the wire [14]. While with each successive technology node, the speed of the transistors became faster, the bandwidth of the interconnect remained roughly constant. In the current technology node, there is already a severe scarcity in channel bandwidth for global interconnects. The use of repeaters joining shorter interconnect lengths somewhat mitigated this problem, but only at the cost of on-chip area and increased power density [15]. Moreover, crosstalk between the interconnects at high frequencies is also becoming a serious concern. As clock speeds reached into the gigahertz regime and signal wavelengths into the centimeter scale, the interconnects are starting to act as antennae and both radiate and receive signals from nearby metal tracks. This led to interference or crosstalk between the interconnects such that even higher signal power is needed to combat the increase in both transmission loss and noise. Coupling between adjacent metal tracks also increased the signal propagation delay.

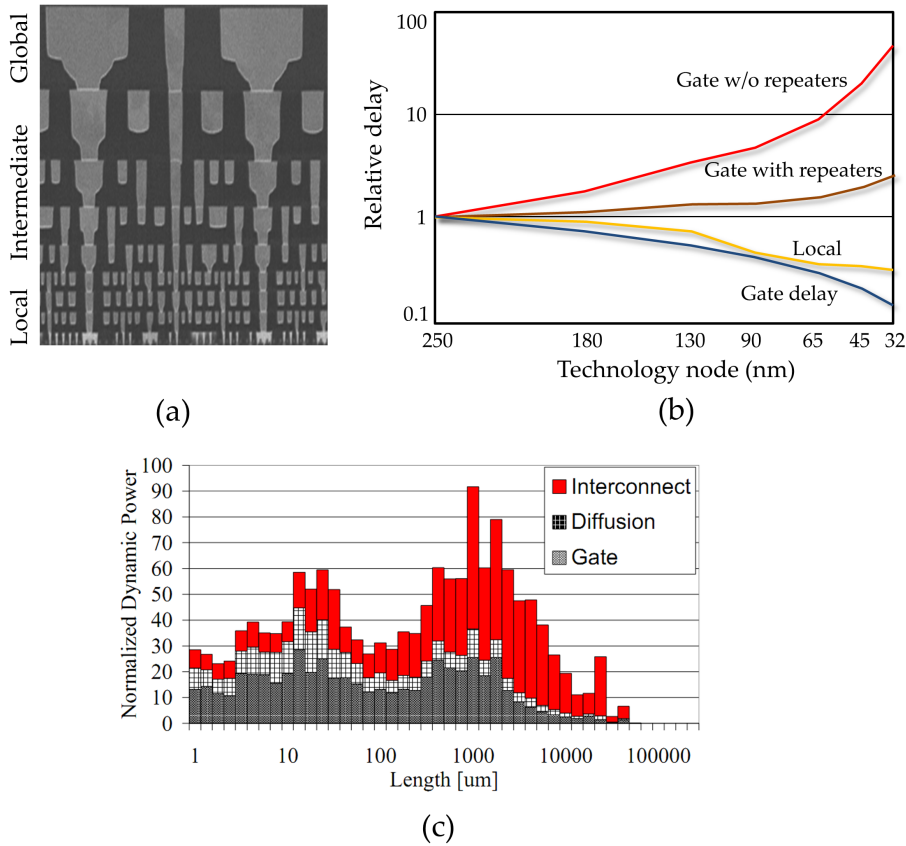


Figure 1.2 – (a) Cross sectional SEM image of the Intel 45 nm technology process. The interconnect layers are divided into three regions: (a) Local, (b) intermediate and Global (reproduced from [9]). (b) Comparison of delays due to gate and interconnects at different technology nodes (data taken from [10]). The gate delay, also called propagation delay, corresponds to the time required for the output of a logic gate to make a transition from one stable state to another. With each successive technology nodes, as the device size and the gap between devices shrink, the gate delay and the delay due to local interconnect reduces. In contrast, the delay due to the global interconnect increases super-linearly. Global interconnects with repeaters can be incorporated to mitigate the delay but at the cost of more power consumption and chip area. (c) Dynamic switching power breakdown versus interconnect length (reproduced from [11]). Over 50% of the dynamic power consumption results from the capacitance associated with the metal interconnection, whereas capacitance of the CMOS circuit (gate capacitance) contribute another 34% and rest comes from the diffusion capacitance of the source and drain. The plot also reveals that the contribution of the interconnection to the total dynamic power consumption increases with increasing length of the interconnect. There are two power peaks, correlated with the total wiring. The peak at the shorter length is dominated by the gate and diffusion capacitance, while the second peak is mainly dominated by the interconnect capacitance.

Another major issue with the electrical interconnects now is the power consumption. Although the power dissipated from each transistor reduces with the scaling of its size, the power dissipation from the interconnects increases per unit length due to the increased resistivity of the thinner metal interconnects. This is further escalated by the increase in the length of the interconnect, as the resistance and the capacitance of an interconnect are proportional to its length. Figure 1.2c shows the percentage of dynamic power lost in the interconnect of a typical processor versus channel length. The dynamic power dissipation on the chip arises from periodic switching of different capacitors and obeys the relation $P_{dyn} \approx CV^2f$, where C is the capacitance, V is the supply voltage and f is the signal frequency [11]. As the interconnect length increases, its contribution to the total dynamic power dissipation also increases. In fact, [11] estimated that over 50% of the dynamic power consumption is due to the interconnects. While many clever tricks, mostly material-related, have been played over the years to improve on this fundamental limitation of electric transmission lines, the limit itself turns out to be “scale-invariant” [14]. Scale invariance means that the problem cannot be solved just by making the wires thicker or thinner, but that power loss becomes worse with increasing speed, bandwidth, and particularly, length.

Currently the lithographic tools used to expose the patterns limit the microprocessor size to around 1-2 cm², which in turn limits the total amount of heat that can be dissipated from a microprocessor to about 200 W. The contribution of interconnects to this power dissipation ceiling increases superlinearly as the data rate increases. This is the primary reason for performance saturation in the single-core microprocessors since 2004. The computer industry has since migrated from single core processor to multi-core processor architectures to maintain the pace of increasing computational capability while at the same time maintaining the power dissipation below the maximum power ceiling. As the maximum bit rate of an electrical wire scales inversely with the square of its length [16], the greater link length required in multicore architectures aggravates, rather than solves, the problem.

To overcome the delay, power and bandwidth limitations of traditional metal interconnects, the International Technology Roadmap for Semiconductors (ITRS) has identified several alternatives such as carbon nanotubes, graphene nanoribbons, superconducting wires, or optical waveguides etc. [10]. In this thesis, I explore the potential of optical interconnects as an alternative solution.

1.3 Migration to optical interconnects: motivations and challenges

The advantage of transmitting data optically has been known for a while. For example, in telecommunication networks, fiber optic cables have already completely replaced electrical lines. Coincidentally, both the computation and communication technologies were first developed around 1970’s, with Intel’s first commercial microprocessor chip being launched in 1971 and, a few years later, the first fiber-optic service established in Chicago that car-

ried voice, data and video signals over 1.5 miles of underground cables [17]. Such a communication technology soon became necessary to connect large sections of the population together, which generate large amounts of data that need to be carried over thousands of miles. As an example, today a single fiber-optic communication link can carry 300,000 two-way voice channels simultaneously (e.g. Transatlantic cable TAT-13). That's impressive and explains why fiber-optic communication systems form the backbone of modern telecommunication systems.

In the current telecommunication and datacommunication networks, optical fibers are usually installed in the backbone and backhaul network, while copper wire or coaxial cable still dominates short distance communication networks. As the demand for transmission bandwidth increases, metal interconnects are becoming inefficient even for short distance communication, requiring an optical solution not only for local data communication networks but increasingly also for intra-computer and even on-chip data transmission.

In contrast to electrical interconnects, optical interconnects transmit information in the optical domain, mostly in the form of light pulses. The electrical data generated from the electronic circuitry is encoded into a beam of light using an electro-optic modulator, transmitted via an optical cable/waveguide and converted back into electrical data using photo-detectors at the receiving end. Optical interconnects have many advantages compared to electrical interconnects [15]. While in practice, the electrical signals in the RC lines can only propagate at a small fraction of the speed of light, optical signals propagate at a speed very close to the speed of light in the medium. This can substantially reduce the interconnect delay and latency.

Another major advantage of optical over electrical interconnects is the possibility of wavelength division multiplexing (WDM). Due to the extremely high carrier frequency (10^{14} Hz) of the optical signal, multiple high-bandwidth optical signals can be carried in the same waveguide, simply by using different carrier frequencies for each channel. As a result, the aggregate bandwidth can be well beyond the modulation rate on any one channel. This is impossible in electronic systems, where each high-bandwidth signal must be allocated to its own wire. Optical signals are also largely free from resistive or capacitive issues and hence also from the RC time constant and ohmic loss issue which dominates the propagation loss and signal distortion in electrical interconnects. Therefore in optical interconnects, the Nyquist frequency rather than an RC time constant becomes the bandwidth limiting factor. But since the optical frequency is at several hundred terahertz, the Nyquist limits for such signals is so high as to be of no concern.

To replace electrical interconnects by optical interconnects, however, there are certain challenges which need to be overcome. As highlighted by the ITRS [10], major hurdles are the production and integration cost of optical components with existing CMOS circuits, the size and power consumption of the optical components such as the optical source, the electro-optic modulator and the photodetector.

Traditionally, devices for optical communications have been predominantly made of compound semiconductor materials such as gallium arsenide

and indium phosphide and electro-optic materials such as lithium niobate. Optical components based on these “exotic” materials have demonstrated excellent performance, but suffer from high cost and large size; these properties relate to complex processing, low yield and difficulty to integrate. A common material platform for both electronics and optics is, therefore, a necessity to reducing the production cost and to increasing the possibility of opto-electronic integration.

Regarding power consumption, the power in an optical interconnect is consumed mainly by the active components, such as optical source, modulator and photodetector, whereas ideally no power is lost in routing the signal via optical waveguides and fibers. For optics to replace electrical interconnects for short distance communication, the energy consumption of optical devices has to be very low. [16, 18] gave an extensive review of the energy consumption for existing electrical interconnects, and proposes values for the energy consumption for both the overall system and individual device components for viable optical interconnects. Based on the ITRS projections of 2022, for off-chip communication, the system energy consumption should be less than 1 pJ/bit, whereas any individual device should not consume more than 20 fJ/bit. For the case of on-chip interconnects, the system energy limit is set at 200 fJ/bit with the individual device energy requirement at 10 fJ/bit. To meet these challenging specifications, the choice of an optimum system architecture and device design is crucial. At the same time, the technologies developed along the way should also be scalable to longer distance optical interconnects.

1.4 Silicon photonics

Every transition from an established technology to a new one involves cost; however, this cost can be minimized by maximizing compatibility with the established technology. For over five decades, silicon has continued to be the preferred material for electronics industry, such that any technological improvement in CMOS microprocessor has been adopted based on its compatibility with silicon technology. Therefore, the most economically viable way of achieving opto-electronic integration is to leverage the CMOS infrastructure and to use silicon technology for optical devices as well. This driver is the primary motivation behind silicon photonics research, which began in mid-1980s with the seminal works from Soref and Lorenzo [19, 20] and has continued ever since.

1.4.1 Materials for silicon photonics

1.4.1.1 Silicon on insulator

The most commonly used material platform in silicon photonics, for both active and passive optical devices, is silicon on insulator (SOI). An SOI wafer consists of a silicon dioxide (buried oxide) layer sandwiched between two layers of crystalline silicon. Besides the fact that silicon is transparent, the large refractive index contrast between crystalline silicon (~ 3.5) and the

buried oxide (~ 1.4) at telecommunication wavelengths enables strong light confinement in the top silicon layer. By etching the silicon layer to form a rib or a wire waveguide, excellent lateral confinement can also be achieved such that optical waveguides with small bend radii and thus compact photonic circuit architectures are feasible. SOI is also commonly used in many semiconductor circuits, which makes it a suitable platform for achieving integration of electronic and optical components on the same chip. There are currently three common techniques to produce SOI wafers:

SIMOX (Separation by Implanted Oxygen): In this technique, the buried oxide layer is formed by implanting high doses of oxygen ions into the wafer. A high temperature anneal is then used to form a continuous layer of silicon dioxide and to recrystallize the damaged silicon. The complete process is shown in Fig. 1.3a. A major limitation with the SIMOX process is that it is difficult to achieve a thick buried oxide layer greater than $0.4 \mu\text{m}$ and it has a relatively large amount of threading dislocations (10^4 - $10^6/\text{cm}^2$) in the top silicon that do not heal even after the annealing process.

BESOI (Bond and Etch-back SOI): The BESOI process involves bonding two silicon wafers together. One of them is called seed, of which the top SOI silicon layer is created, and the other is called handle, which serves as the substrate. The seed wafer is first implanted with a high concentration of boron as the etch stop. Then both the wafers are oxidized and placed one on top of one another with the oxidized layers in direct contact. The exposed seed wafer is then etched up to an etch stop. Another implementation of this process is to use polishing or grinding to remove the excess silicon from the seed layer and to control the top silicon layer thickness, thereby avoiding the need for the etch stop layer (Fig. 1.3b). While the BESOI process has more flexibility in terms of oxide thickness compared to SIMOX, it is difficult to attain thin and highly uniform silicon active layers because of the layer thinning process.

SmartCut SOI [21]: This process starts by oxidizing a seed wafer to form the desired buried oxide layer. The wafer is then implanted with hydrogen to form a uniform hydrogen-rich layer underneath the top oxide. The seed wafer is then flipped upside down onto a handle wafer. A thermal annealing process bonds the two wafers together. During this annealing process, hydrogen implanted in the seed wafer forms molecular hydrogen and micro-cavities, thereby building up pressure in the hydrogen-rich region. In this way the wafer can be split along the implanted plane and polished using chemical-mechanical planarization (CMP) process (Fig. 1.3c). This method has many advantages as it enables a very accurate control of both the buried oxide and the top silicon layer thickness and quality. Furthermore, unlike BESOI process, no wafer is wasted in grinding and thinning operations and the same time high quality seed wafers can be reused many times, thus reducing the cost of the fabrication process. It is also possible to achieve a high yield and level of control, with silicon layers ranging from 5 nm to $1.5 \mu\text{m}$ thickness with the buried oxide thickness varying from 5 nm to $5 \mu\text{m}$. This large variety is crucial for silicon photonic devices, as submicron cross-section waveguides require thicker ($>1.5 \mu\text{m}$) buried oxide layers to avoid leakage of

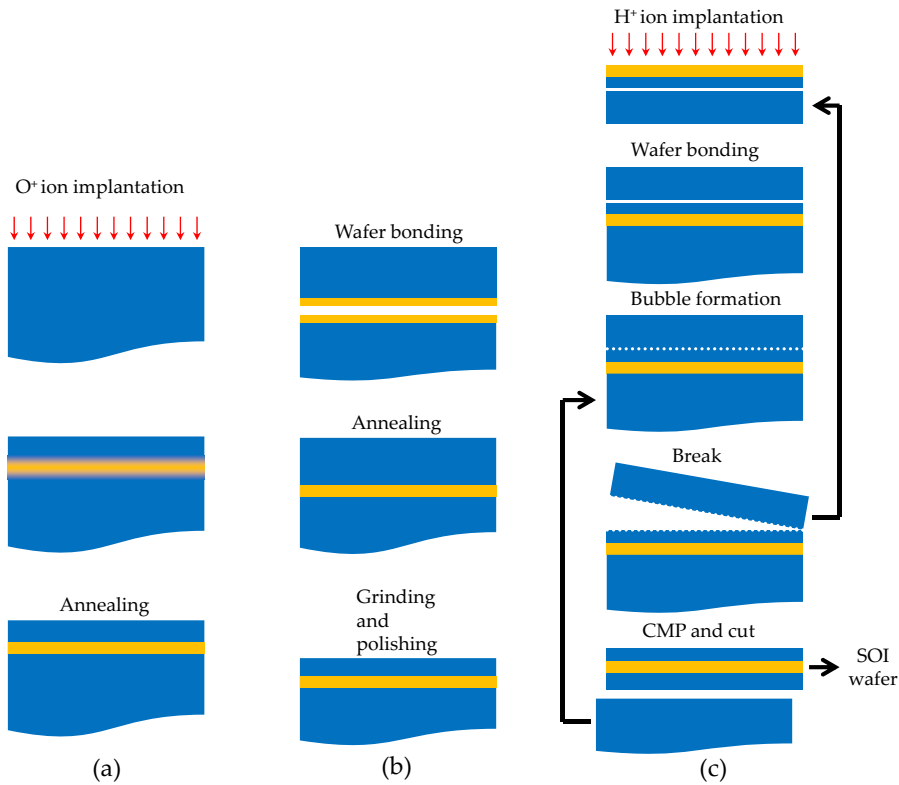


Figure 1.3 – Fabrication process of SOI: (a) SIMOX, (b) BESOI, (c) SmartCut

the light into the silicon carrier wafer.

Most of the proposed interconnect designs in silicon photonics use the SOI platform to realize passive and active optical devices and thereby maintain CMOS compatibility [6, 22, 23, 24, 25, 26, 27, 28]. Many of these designs demonstrated that optical data transmission can substantially enhance the overall system performance; however, there are several challenges inherent in the SOI platform, including optical interface loss resulting from fiber-to-chip coupling, waveguide propagation and waveguide crossings and optical nonlinearities such as two photon absorption (TPA), and the resulting free-carrier absorption (FCA) as well as free carrier dispersion (FCD) effects [29]. Moreover, the crystalline silicon used here can only be grown epitaxially from another crystalline silicon seed, thus making it impossible to deposit crystalline silicon directly onto a spacing layer (e.g. silicon dioxide) that is required for any 3D integration. Therefore, using only crystalline silicon for integrated photonic circuits restricts the design and fabrication of optical devices to a single device layer. One way to improve the design flexibility is to stack different optical components vertically by using other CMOS-compatible materials, such as polycrystalline silicon or silicon nitride [30, 31]. The advantage of using these materials is that they can be deposited at relatively low temperature (below the CMOS back-end thermal budget) and form multiple photonic layers analogous to metal wiring in CMOS circuits.

1.4.1.2 Polycrystalline and amorphous silicon

Polycrystalline silicon (polysilicon) is commonly used as a gate material for transistors in the CMOS fabrication process. For photonic applications polysilicon can be deposited as an electrically conductive light-guiding material. Unlike crystalline silicon, polysilicon does not have a homogeneous crystalline structure, but instead consists of crystalline grains separated by thin disordered grain boundaries. These grain boundaries cause scattering and absorption of light; however, by carefully controlling the fabrication process, the size of the crystalline grains and the nature of the grain boundaries can be optimized to achieve acceptable optical and electrical properties. Due to its electrically conductive nature, active optical components such as modulators and photodetectors have also been demonstrated using deposited polysilicon layers [32, 33]. Deposited hydrogenated amorphous silicon (a-Si:H) is also used to demonstrate waveguiding. The refractive index (3.5) and waveguide propagation loss (2-3 dB/cm) are comparable to crystalline silicon, but the propagation loss can increase dramatically with time and/or temperature if hydrogen diffuses out [34], making it a less stable material.

1.4.1.3 Silicon nitride

Recently, silicon nitride has been considered as an alternative material for optical transmission and passive optical components [30, 31, 35]. In the CMOS fabrication process, silicon nitride (Si_3N_4) is used as a masking layer. Although silicon nitride is not useful for electrically active optical components, its relatively high refractive index (~ 2), in comparison to silicon dioxide, allows for light confinement in submicron waveguides. Moreover, silicon nitride as a waveguiding material can exhibit lower linear propagation loss [36] and lower nonlinear loss [37] mechanisms than crystalline silicon.

1.4.1.4 Germanium

In CMOS foundries, germanium is used to create strained silicon and silicon-germanium (SiGe) transistors. In silicon photonics, germanium is extensively used as the material for photodetection. Germanium is an indirect bandgap semiconductor with bandgap energy of 0.67 eV, which enables strong absorption at around $1.55 \mu\text{m}$. The most popular way of integrating germanium on an SOI platform is by using selective epitaxial growth of germanium on silicon. The primary challenge for germanium integration is the 4% lattice mismatch with silicon, which makes it difficult to grow high-quality germanium material [38]. Back-end thermal budget may also be a limiting factor for germanium integration, as epitaxial growth process generally requires a high temperature.

1.4.2 Passive optical components

For any optical interconnect, optical waveguides are the most basic component to carry optical signals from one point to another. As discussed above, silicon photonic materials, such as SOI and silicon nitride offer excellent

confinement properties, thus enabling very compact waveguides and optical circuits.

The first demonstration of a silicon based planar waveguide was reported in [20, 19], for the infrared communication wavelengths of $1.3\ \mu\text{m}$ and $1.6\ \mu\text{m}$. For waveguiding, they used single-crystal silicon epitaxially grown on heavily doped silicon substrate. The observed propagation loss ranged from 5 to 13 dB/cm in the slab waveguides and from 15 to 20 dB/cm in the rib waveguides [19]. In 1991, standard SOI was used to fabricate rib waveguides and a propagation loss of 5 dB/cm was demonstrated [39]. Since then, improvements in SOI quality and waveguide fabrication process have led to single-mode rib waveguide losses of less than 0.5 dB/cm [40] and wire waveguide losses of less than 0.92 dB/cm [41]. Currently, the major contributor to propagation loss is the side-wall roughness. Different fabrication methods have been proposed in order to reduce the surface roughness by avoiding waveguide etching process, such as, local oxidation of silicon (LOCOS) [42] and selective oxidation [43, 44]. Due to its low nonlinearity and transparency in both the visible and infrared spectrum, silicon nitride is being considered as the ideal material for passive optical components [30, 31, 45]. Ultra-low loss waveguiding (0.1 dB/cm) in silicon nitride has been demonstrated in loosely confined [46] or multi-mode [47] waveguides, suggesting almost an order of magnitude improvement over SOI based waveguides.

Motivated by this low loss transmission, researchers around the world have tried to build every integrated optical component using silicon or silicon based materials. As a result, a tremendous amount of literature has been published over the last years on passive components such as filters, switches, coupling devices etc.

1.4.3 Off-chip coupling

To transfer light in and out of a photonic chip, single mode optical fiber is generally used, which has a typical core dimension of $8\ \mu\text{m}$. Due to mode mismatch, such transfer of light often leads to optical losses, known as coupling loss or insertion loss. The amount of coupling loss depends on the difference in refractive index and cross sections of the fiber and the optical waveguide. Typically, a direct coupling between a single mode fiber and a single mode silicon waveguide (with typical dimensions of $220\ \text{nm} \times 400\ \text{nm}$) leads to more than 20 dB coupling loss. For multimode silicon waveguide ($220\ \text{nm} \times 3\ \mu\text{m}$), which is usually used as an access waveguide, coupling loss reduces to around 10 dB. For silicon nitride waveguides, due to its relatively large cross section ($500\ \text{nm} \times 3\ \mu\text{m}$) and low refractive index coupling loss comes down to around 3 dB. For polymer waveguides (e.g. SU-8) this coupling loss becomes almost insignificant ($< 1\ \text{dB}$), due to very low refractive index contrast (~ 1.57) and large cross section ($2\ \mu\text{m} \times 5\ \mu\text{m}$). The relative dimensions of access waveguides and single mode photonic wires in different materials with respect to a single mode fiber core is shown in Fig. 1.4.

The coupling loss associated with high index material waveguides (e.g. silicon or silicon nitride) is definitively a big concern as it is directly linked with performances of the overall optical system, such as the link reach, power

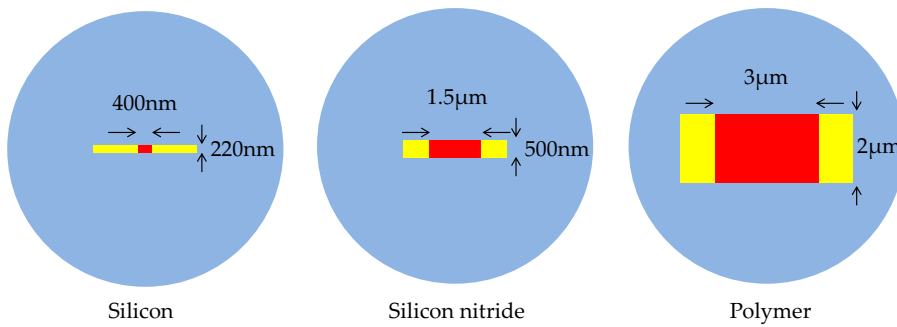


Figure 1.4 – Sketch showing the relative size of a single mode fiber core (blue), wide access waveguides (yellow) and single mode photonic wires (red) in different materials.

consumption, receiver sensitivity, and so on. Consequently, many different techniques have been proposed to overcome the waveguide-fiber coupling issue, following mainly two approaches: grating based coupling and spot size conversion.

Grating couplers are typically one-dimensional gratings that redirect light from a vertically positioned optical fiber into a waveguide using the principles of diffraction (Fig. 1.5a). Several different grating coupler designs have been proposed to minimize the coupling loss to silicon waveguides [48, 49, 50]. In 2006, Luxtera Inc. reported an insertion loss of 1-1.5 dB over a wavelength range of 1537-1557 nm for coupling to a single mode silicon waveguide using a curved one-dimensional grating, which they refer to as a holographic lens [51] (Fig. 1.5b). Such grating couplers can be very compact (10-20 μm) and allow inputs/outputs to be positioned anywhere on the chip, thus offering design flexibility. Although, grating couplers can significantly improve the coupling efficiency, it has some serious drawbacks. The major disadvantages with this coupling scheme are the low 3 dB bandwidth (typically 50 nm) and high polarization dependence. For their application in WDM systems, the 3 dB bandwidth of the grating couplers will essentially restrict the scalability of the overall system. Besides, this coupling scheme requires high refractive index contrast to increase the diffraction efficiency. Hence, grating couplers in low index materials, such as silicon nitride, usually have a very low efficiency [52].

Coupling using spot size conversion can avoid such limitations entailed by the grating couplers. Spot size conversion is essentially an end-fire or butt coupling technique, where the relatively large optical mode from a fiber is transformed into the small mode of a waveguide using a tapered interface section (Fig. 1.5c). Consequently, the wavelength and polarization dependence of such coupling schemes is low. Besides this coupling method does not put any restriction on waveguide material. Spot size conversion can be achieved by using inverse tapers as reported by Shoji et al. [53]. A silicon wire waveguide is tapered down laterally until its tip width is of 60 nm and taper length was 200 μm . Thus, the mode is forced out of the silicon waveguide and into the low-index cladding. A mode conversion loss from a

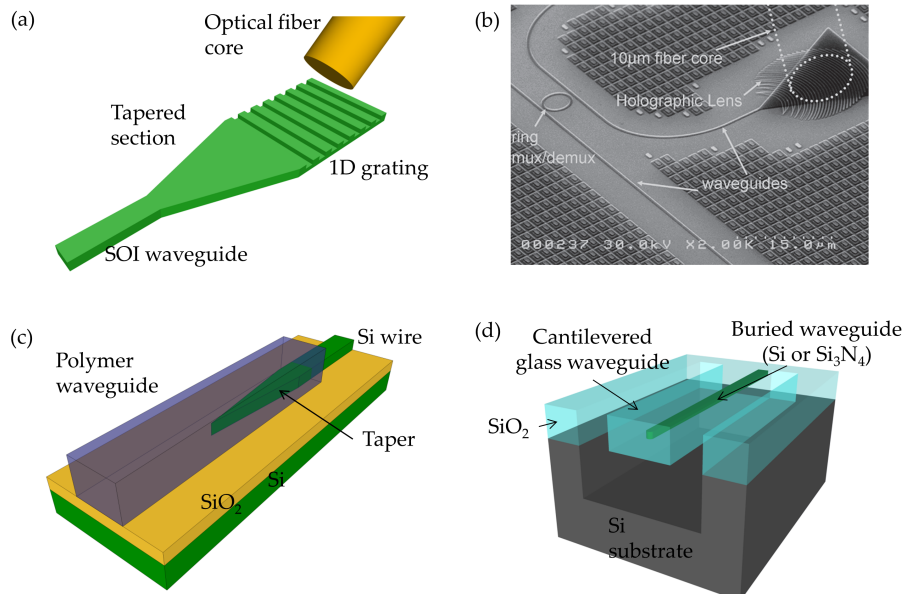


Figure 1.5 – (a) Grating coupler to an SOI wire waveguide, (b) Holographic lens coupler (reproduced with permission of the IEEE from [51], Copyright 2006), (c) Inverse taper to an SOI wire waveguide, (d) Cantilever coupler [54].

single-mode fiber to a silicon waveguide of less than 1 dB was achieved. As a further development, Chen et al. recently reported a coupling technique based on cantilever couplers [54] (Fig. 1.5d). Due to a more symmetric modal distribution in the low index waveguide, the coupling loss can be reduced further. By creating a cantilevered glass waveguide surrounding a high index inverse taper and low index cladding around the glass waveguide, they demonstrated coupling loss of 0.7 dB/facet for silicon nitride waveguides and 1.5-2 dB/facet loss for silicon waveguides. Spot size conversion is an obvious choice when large wavelength range and low index material waveguides are required.

1.4.4 Modulation

An electro-optic modulator is one of the most critical devices in an optical interconnect, as it enables high-speed conversion of an electrical signal to an optical signal. In silicon photonics, the most common way of achieving this conversion is by encoding electrical data onto an optical carrier wave through optical intensity modulation or on-off keying, where each electrical bit “1” or “0” is represented by the presence or absence of light, respectively. Intensity modulation is achieved by changing the complex refractive index, $n_e + ik$, of the modulator material. The real part n_e is the refractive index and the imaginary part k is the optical extinction coefficient. A change in n_e can be translated into an intensity modulation by using an interferometer, such as Mach-Zehnder interferometer (MZI) (Fig. 1.6a) or resonant device such as ring resonator (Fig. 1.6b), microdisc resonator, photonic crystal cavity or Fabry-Perot resonator. In contrast, a change in k leads to an

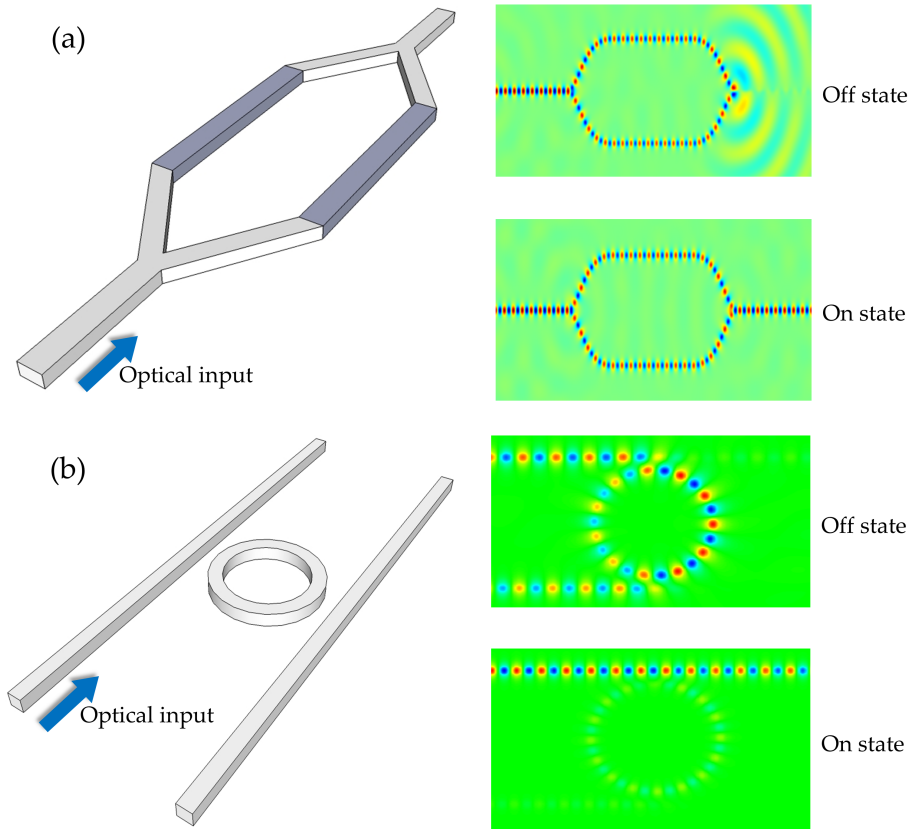


Figure 1.6 – (a) MZI modulator: when the refractive index difference between the two arms corresponds to π destructive interference occurs and as a result no light transmits to the output port (Off state), on the other hand when the refractive index difference is zero, constructive interference occurs and all the incoming light is transmitted to the output port (On state). (b) Resonance based modulator: when the resonance wavelength of the ring matches with the wavelength of the incoming light, light coupling to the drop port through the ring and no transmission occurs at the output port (Off state). If the resonance wavelength of the ring is shifted by changing the refractive index, no coupling takes place and all the incoming light is transmitted to the output port (On state).

intensity modulation directly. In silicon, modulation is generally achieved by changing the refractive index via the free carrier plasma dispersion effect, where a change in free carrier density results in a change of both the real and the imaginary refractive index.

The first experimental demonstration of electro-optic modulation in silicon using the plasma dispersion effect was reported by Teryz et al. in 1991 [55]. They used an MZI-type interferometric modulator to demonstrate a modulation depth of 4.9 dB with a response time of less than 50 ns which corresponds to a bandwidth of ~ 10 MHz, using an operating wavelength of $1.3 \mu\text{m}$. Since then, many different designs have been suggested. The breakthrough occurred in 2004, when Liu et al. first experimentally demonstrated GHz operation of a silicon based modulator [56]. They used the plasma

dispersion effect to achieve phase modulation by employing a novel design based on a Metal Oxide Semiconductor (MOS) capacitor geometry. For an input optical wavelength of $1.558\ \mu\text{m}$ and an rms voltage of $0.18\ \text{V}$, the measured 3 dB modulation bandwidth exceeded 1 GHz. This result gave a much needed impetus to the research on silicon modulators. In 2005, Gardes et al. proposed a different design for a MZI modulator based on depletion of a pn junction [57]. The authors showed that the switching time could be improved from $0.1\ \text{ns}$ for MOS capacitor based devices to $0.014\ \text{ns}$ for depletion type pn diode based devices. A similar design was later used by Liao et al. to experimentally demonstrate a modulator with 40 Gbit/s data transmission capability [58]. Since then, several research groups have reported modulation speeds of 40 Gbit/s [59], 50 Gbit/s [60, 61] and very recently 60 Gbit/s [62] by optimizing the optical and electrical designs of MZI-based modulators. All these designs are based on silicon rib waveguides of millimeter length, which is rather long and requires a lot of actuation energy, as a large capacitance needs to be switched. One way to reduce the phase shifter length is to replace the rib waveguide geometry with 2D photonic crystal waveguides. The highly dispersive 2D photonic crystal waveguides offer the possibility of reducing the group velocity by a factor larger than 100 [63], consequently increasing light-matter interaction. Hence, the active length of the phase shifter can be reduced by the same factor. This effect was first demonstrated by Jiang et al. [64], where an $80\ \mu\text{m}$ long photonic crystal phase shifter demonstrated π phase shift with $0.15\ \text{mA}$ driving current. The modulation speed of this device, however, was relatively low (300 MHz) because they used the thermo-optic effect to achieve modulation. Recently high speed modulation in photonic crystal waveguide based MZI modulator was reported by Nguyen et al. [65, 66]. By using a pn diode in depletion mode, they managed to achieve modulation speed up to 40 Gbit/s with a phase shifter length of only $90\ \mu\text{m}$.

Interference based modulation has certain advantages, such as high speed operation and large operating wavelength range, which corresponds to a large thermal stability, but they also suffer from serious drawbacks. Primarily, their large size prohibits their use in on-chip or chip-chip optical interconnects, this also leads to large energy consumption (in pJ/bit [59, 65]). Consequently, these modulator designs are more suitable for long distance communication, e.g. rack-rack communication or telecomm access networks, where the requirements for device footprint and energy consumption are relatively relaxed and high speed transmission is the priority. To reduce the device footprint which is more suitable for chip-scale integration, Xu et al. proposed and demonstrated a modulator design based on a ring resonator [67]. The basic principle of such a modulator is that of a tunable filter and to tune the ring in and out of resonance by changing the refractive index of the ring. Using a ring with $12\ \mu\text{m}$ diameter, they demonstrated a modulation speed of 1.5 Gbit/s [67]. Later on, by improving the electrical design, they increased the modulation speed to 3 Gbit/s and also demonstrated a switching energy (energy required to make a transition from “0” state to “1” state) of 55 fJ [68]. Due to their compactness and simplicity, ring resonators

have become very popular for intra- and inter-chip communications. High modulation bandwidths (up to 20 GHz [69]), low driving voltage (1 V [70]) and very low switching energy (50 fJ/bit [71]) have all been demonstrated. Simultaneously, there has also been some report on resonant modulators based on photonic crystal cavities [72]. Due to their ability to confine light strongly both in time and space, the switching energy required to modulate such cavities can be one to two orders of magnitude lower than the conventional ring resonators. The device reported in [72] has capacitance as low as 5.6×10^{-18} F. Along with low power operation, the large free spectral range of single mode photonic crystal cavities [73, 74] can overcome the bandwidth limitations, which is common in ring resonator based devices. Thus, a proper implementation of photonic crystal cavities in WDM systems can potentially meet the required interconnect density and low energy specifications.

1.4.5 Photodetection

At the other end of the optical interconnect, photodetectors translate incoming optical signals back into the electrical domain. Since crystalline silicon does not exhibit linear absorption in the telecommunication wavelength bands, germanium is typically used as the absorbing material for this purpose [38]. Germanium-on-silicon photodetectors integrated on SOI rib waveguide were first demonstrated by Vivien et al. in 2007 [75] with a 25 GHz bandwidth and 1 A/W responsivity. Since then, using this material system, bandwidths exceeding 40 GHz [76, 77], responsivities above 1 A/W [76, 78], quantum efficiencies higher than 90 % [77, 78], dark currents below 200 nA [78], and energy consumption around 33 fJ/bit [77], have all been demonstrated.

Although germanium performs extraordinarily well as a photodetector, the 4 % lattice mismatch with silicon imposes design and fabrication complexities. In order to avoid such complexities, an all-silicon approach is more desirable. Due to its relatively large bandgap, silicon is most commonly used as detectors for visible wavelengths. By creating crystal defects in bulk silicon, the infrared absorption in silicon can be significantly enhanced [79]. Defect based detection has some obvious advantages over germanium based techniques; first they are completely CMOS compatible and secondly fabrication of defect detectors does not require any complex fabrication technique and only requires a single ion-implantation step. With a reported detection bandwidth as high as 20 GHz and a responsivity of 0.8 A/W [80], this detection technique is proving to be a viable alternative to germanium-based detection.

1.4.6 WDM system on silicon

Energy efficient WDM is the key to satisfying the requirements of interconnect density and reach. Based on the modulation scheme available, there are two popular implementations of WDM system on silicon. One of them is based on broad band modulators (e.g. MZI) with arrayed waveguide gratings (AWG) and the other one is based on cascaded ring resonators. Figure

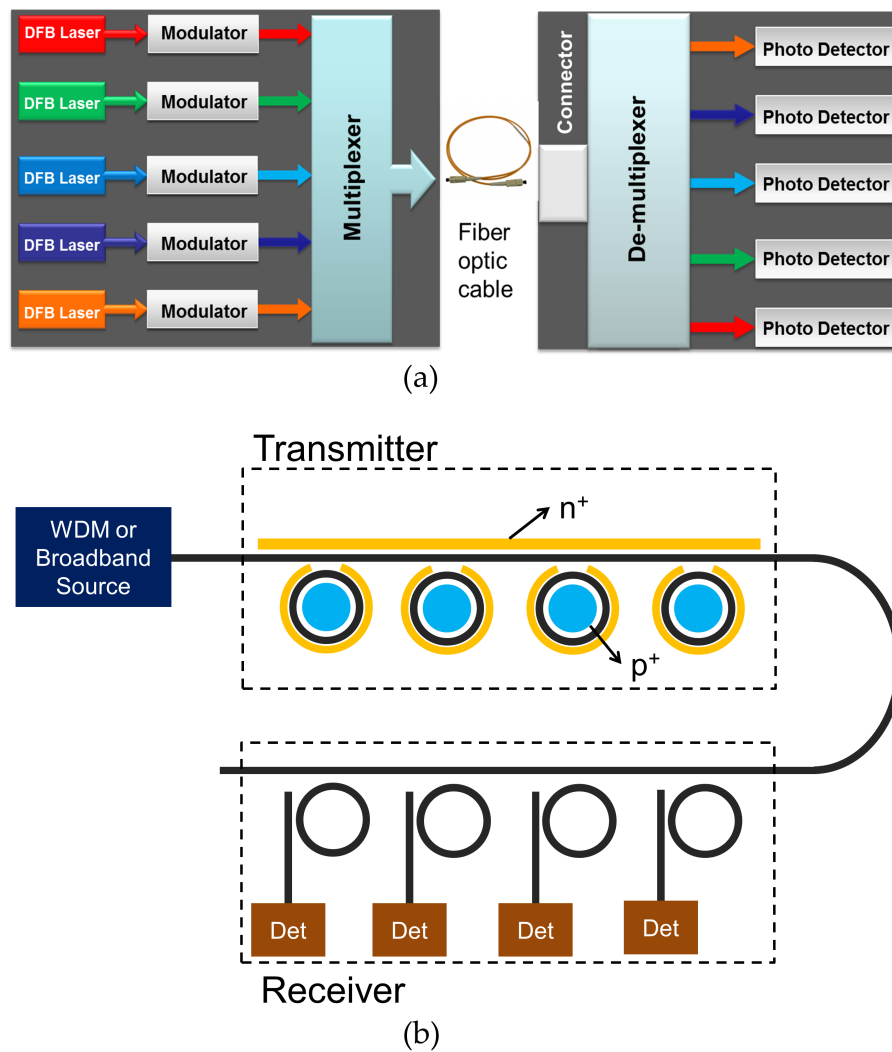


Figure 1.7 – WDM system based on (a) broadband modulators, (b) ring resonator modulator [81].

1.7a shows the schematic of the WDM system based on broadband modulators. Individual modulators are fed by separate narrow linewidth lasers and the modulated signals are then multiplexed into a single channel using an AWG. At the receiver end, the individual channels are demultiplexed and detected using separate germanium photodetectors. In the resonance based architecture (shown in Fig. 1.7b [81]), multiple ring resonators are cascaded to a single bus waveguide. Due to the wavelength selective nature of the ring resonators, each channel gets modulated while in the bus, thus obviates the need for any multiplexer. At the receiver end, individual channels are routed to different germanium detectors by separate ring resonator filters, which are matched to different wavelength channels.

The MZI modulator based BLAZAR transceiver developed by one of the first Silicon Photonics companies, LUXTERA, provides a long reach (up

to 4 km) at probably the lowest power consumption commercially available (~ 20 pJ/bit). The key to this efficiency, however, is the use of a single narrow linewidth laser that is spatially multiplexed into multiple single mode fibers [82]. Thus, it is essentially a point-to-point optical link, with fiber cost, volume and bending radius serious issues. True WDM systems are due to become available shortly [83] but with higher energy per bit values (~ 30 pJ/bit), leaving cost per length of fiber as the only advantage. One major contributor to the power consumption is the light source itself. Working at higher bit rates is an obvious solution (more bits for the same laser power), however, this then requires serialization/deserialization (SerDes), with additional costs in terms of electronic power and complexity. Germanium electroabsorption modulators are promising for compactness and low modulation energy, however incorporating them efficiently with other devices is challenging [84].

Ring resonator based systems can also provide very low modulation energies ~ 10 s of fJ/bit [68], as compared to the ~ 1 pJ/bit limit for an MZI and naturally provides some of the wavelength selectivity required for WDM. Recently, such a link with an impressive on-chip power consumption 2 pJ/bit has been reported [85], but once again the light source is a major problem and the electrical power consumed is excluded from the power budget. Receiver power consumption is also a major concern. This is often as high as 8 pJ/bit [86] despite the very high responsivities of germanium photodiodes; the bulk of this occurs in the transimpedance amplifier (TIA), required to amplify the detected signal. Notably, the loss of the optical link was 25.5 dB arising from the high number of components and interfaces, putting pressure on both source and receiver. Finally, there was no wavelength selective component on the receiver side. This would have introduced another 3 dB of loss [87] compounding the issues with the source output. In short, there are three primary issues, the light source power, the power consumed by the receiving circuit and the complexity and optical loss introduced by the WDM components. These are inter-related, for example, a reduced laser output power (thus reducing the electrical power) increases the requirements on the receiver.

A WDM optical link with a total of 1 pJ/bit will be a major milestone. It would be difficult for existing systems to approach this number, let alone beat it. Incremental steps will not deliver these improvements, marking the need for an “outside the box” solution.

1.5 Aim of the Thesis

In this thesis, I aim to develop a new framework for optical interconnects with the ability to realize ultimate reduction in cost and power consumption for Dense WDM applications. A conceptual design of the proposed architecture is shown in Fig. 1.8. This architecture is based on a vertically coupled photonic crystal-waveguide system. At the transmitter end, multiple photonic crystal cavity modulators are coupled to a single bus waveguide and different wavelength channels are modulated and multiplexed while in the bus by separate cavity modulators. Essentially, this cavity-waveguide system acts as a

highly wavelength selective reflector. By suitably designing the waveguide and the cavity, at resonance wavelength (of the cavity), light propagating through the waveguide can be completely reflected back towards the input end of the waveguide, thus providing almost zero transmission and complete reflection. By locally modulating the refractive index of the cavity via free carrier plasma dispersion effect, the resonance wavelength of the cavity can be modulated, which results in a modulation of the transmittance of the waveguide. At the receiver end the same vertically coupled system is used to demultiplex and detect individual channels. Photodetection is achieved by creating defect states in silicon to enhance infrared absorption. Due to the wavelength selective nature of the device, light only at a certain wavelength gets detected.

Due to its ability to strongly confine light both in time and space, operating energy for photonic crystal modulators can be significantly small, more than three orders of magnitude smaller than MZI modulators and one to two orders of magnitude smaller than ring resonators. Moreover, due to its small mode volume, the photodiodes based on photonic crystal cavities can have ultra-small capacitance [72], this potentially obviates any need for transimpedance amplifiers at the end of the detectors. Our unique vertically coupling scheme allows us to couple multiple photonic crystal cavities to a single waveguide, thus offering huge channel scalability (potentially up to 200 channels/ fiber) without compromising the design complexity of the overall system. Besides having a waveguide integrated on top of the cavity modulators promises better design optimization for the optoelectronic integration in case of on-chip interconnects and incurs low optical loss due to minimum number of optical interfaces.

Finally, in order to avoid the prohibitive power consumption entailed by banks of individual lasers used in state-of-the-art WDM system, here I rely on a single multiwavelength comb laser. Multiwavelength light sources have been highlighted as key components in such WDM networks [16, 18, 88]. As calculated in [88], a 1-2 W laser can potentially run a terascale network. Advances in multiwavelength lasers are putting such numbers within reach [89]. A centrally located, amplified comb laser provides such an option, with the added advantage that the light source heat dissipation is kept off the computing chip [16].

This thesis is organized as follows: Chapter 2 gives a brief description of different fabrication tools and techniques used to realize the proposed architecture. Chapter 3 presents a detailed discussion about the vertical coupling scheme and the conditions for high coupling efficiency between the waveguide and the photonic crystal cavity. Chapter 4 demonstrates a five channel WDM transmitter with ultra-small operating energy. Demonstration of dense WDM is also performed by operating all the five channels using a single multiwavelength comb laser. Chapter 5 demonstrates a cascaded detector architecture with two channels. A discussion about detection efficiency is also presented. Finally, Chapter 6 gives an overall summary of the thesis highlighting the potential advantages of the proposed architecture in comparison to different state-of-the-art architectures and concludes with

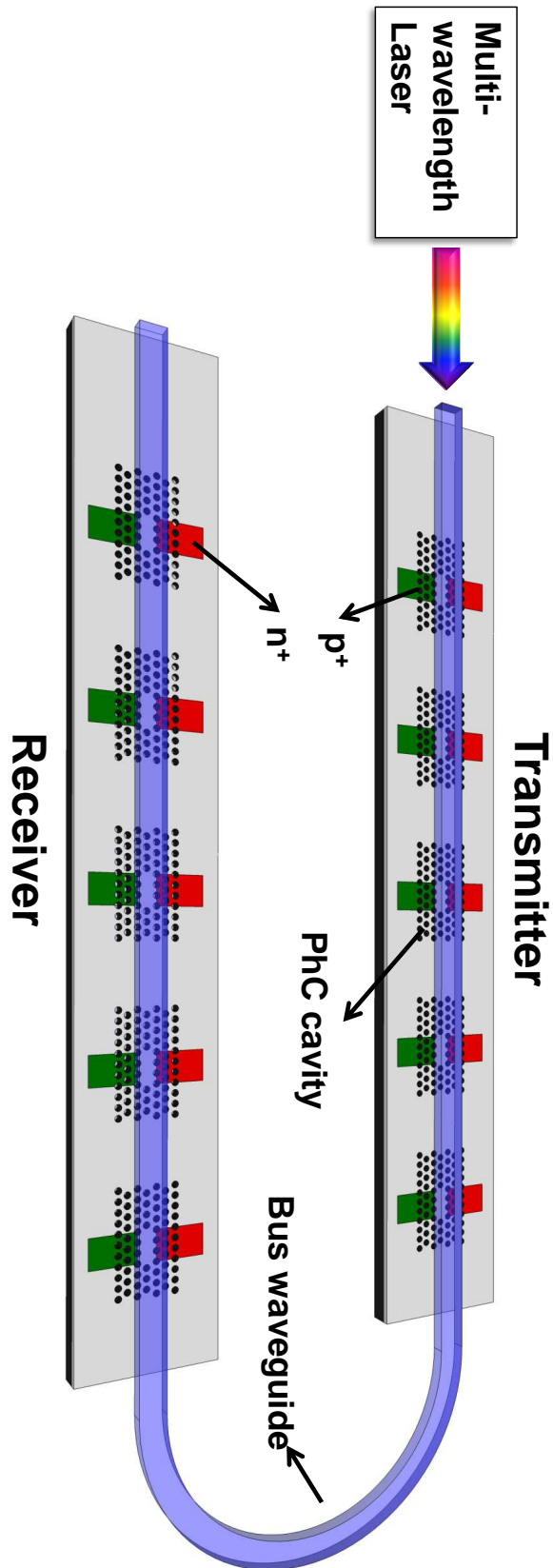


Figure 1.8 – Optical interconnect based on the vertically coupled photonic crystal cavity-waveguide system.

possible future research goals.

Chapter 2

Fabrication Tools and Techniques

2.1 Introduction

This chapter gives a brief overview of the main fabrication tools and techniques that were used throughout this work. For the pattern generation, both photolithography and electron beam lithography techniques were used. A conscious effort was made to reduce the use of electron beam lithography wherever possible and use photolithography instead, in order to reduce the demand on our tool and also with an eye to future mass production (also known as “mix and match lithography”). So electron beam lithography was only used for structures with submicron features. I begin this chapter by introducing the two lithography techniques. I then continue to the reactive ion etching process, which was used for transferring patterns to different materials, such as silicon, silicon dioxide, silicon nitride. Finally, I discuss the metal contact formation using thermal evaporation.

2.2 Photolithography

Photolithography involves exposing a substrate through a photosensitive material, called “photoresist”, according to a desired pattern. Photolithography is a simple and parallel process, hence much faster than electron beam lithography, and is used where the requirement for high resolution and high alignment accuracy is less stringent. I use photolithography for exposing large areas (with minimum feature size greater than $1\ \mu\text{m}$), such as alignment marks, ion implantation windows, contact vias, or lift-off windows for metal contacts. The exposure process is based on the photochemical reaction of the resist to UV photons; in the case of a positive photoresist, the exposed areas become soluble in the developer, while for a negative photoresist, the exposed areas cross-link and become resistant to the developer and only the unexposed areas dissolve. The process is depicted in Fig. 2.1.

In the fabrication process, I used an EVG620 mask aligner. The exposure wavelength is 365 nm with lamp power of 500 W and the exposure resolution

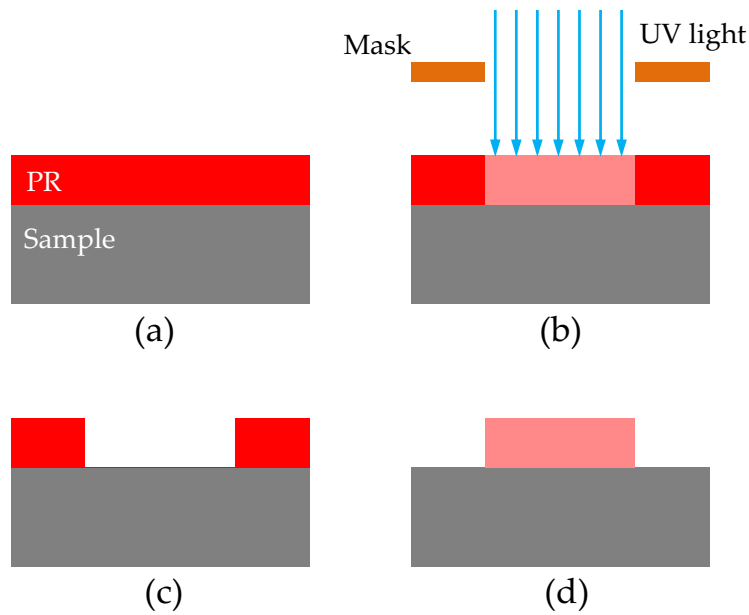


Figure 2.1 – Photolithography process flow: (a) Sample is spun with photoresist (PR). (b) Sample is then exposed under UV light through a photomask. (c) In the case of positive photoresist, the exposed part is dissolved during the development. (d) For negative photoresist, the exposed part remains after development.

is $\sim 1\ \mu\text{m}$ in “soft-contact” mode. In the “soft-contact” mode, the substrate is brought into contact with a photomask by a preset force during exposure. The photomask is used to selectively expose the photoresist with the desired patterns. This photomask consists of a quartz plate, one side of which is coated with UV blocker (iron oxide in our case) into which the required pattern has already been transferred. For most of our photolithography steps (except the lift-off process), a single layer of the positive photoresist S1818 is used. The substrate is first spin-coated with S1818 at 5000 rpm to produce $\sim 2\ \mu\text{m}$ thick layer and then baked for 90 seconds at 100°C to drive off the solvent. The sample is then aligned to a desired pattern on the photomask using the mask aligner and exposed under UV light for 5 seconds. After the exposure, the sample is developed for 35 seconds in MF319 developer and finally cleaned with deionized water.

2.3 Electron beam lithography

Unlike photolithography, in electron beam (e-beam) lithography, the patterns are defined using a beam of electrons to expose an electron sensitive resist, known as e-beam resist. The e-beam is steered and focused by a set of magnets en route to the sample surface. The magnets are controlled by computer to define the desired pattern. To achieve high resolution patterns, e-beam lithography is preferred over photolithography, as it allows the definition of features down to a few 10s of nm in size. E-beam lithography,

Resist	Spin Speed (rpm)	Resist thickness (nm)	Baking Temperature (°C)	Baking time (nm)
ZEP	3200	320	180	10
SU-8	5000	2000	100	3
PMMA	5000	600	180	5

Table 2.1 – Spin coating recipe for different e-beam resists.

however, is more time consuming than photolithography, since every feature has to be written separately. As an example, a photonic crystal pattern of $200\ \mu\text{m} \times 10\ \mu\text{m}$ typically takes about 3 minutes to be exposed. Consequently, in this work, e-beam lithography is only used where structures with high resolution features, such as photonic crystals or submicron waveguides, are needed. For all the e-beam lithography steps, I have used a hybrid RAITH ELPHY Plus/Leo Gemini 1530 electron beam writer, which has a maximum acceleration voltage of 30 kV and a maximum write field size of $200 \times 200\ \mu\text{m}^2$.

In e-beam lithography process, the physical structure of the e-beam resist changes when exposed to electrons. The resist requires a certain amount of electrons per unit area, called the exposure dose (measured in $\mu\text{A}\cdot\text{s}/\text{cm}^2$), to get exposed. Following exposure, the resist is developed to generate the desired pattern. Similar to photoresists, e-beam resists can be classified into two groups, positive and negative. In this work, the most common resist used is Zeon Chemicals ZEP 520A resist (ZEP). ZEP is a high resolution positive resist allowing the definition of very small (10s of nm) features such as photonic crystal holes. Other e-beam resists used here are Microchem SU-8 (negative resist) and Polymethyl Methacrylate (PMMA, positive photoresist). SU-8 was used to define waveguides and PMMA was used for the lift-off process in some initial test devices. The recipe for resist preparation and development is summarized in Table 2.1 and 2.2.

While writing large areas, the e-beam system breaks the design patterns into multiple segments, known as write fields. Each write field is written separately and the sample stage is moved in order to write the adjacent write fields. The content of each write field is written on an exposure grid where individual grid represents the smallest pixel that can be written. The pixel size is dependent on the resolution of the digital to analogue converter (DAC) and the write field size. Figure 2.2a shows a relationship between write field size and achievable resolution. The red lines show the maximum angle that the electron beam can be deflected to and the dotted lines show the minimum deflection angle possible ($\delta\phi$). It is obvious that a smaller write field would give a better resolution (δx). Our e-beam system has a 16 bit resolution, which means that each write field can be divided into $64,000 \times 64,000$ grids. The smallest write field that can be realized with our system is $50 \times 50\ \mu\text{m}^2$,

2. FABRICATION TOOLS AND TECHNIQUES

Resist	Developer	Develop time (sec)	Developer Temperature (°C)	Developer remover	Resist Stripper
ZEP	Xylene	45	23	IPA	1165
SU-8	EC Solvent	15	Room Temperature	IPA	1165
PMMA	H ₂ O:IPA (3:7)	50	23	IPA	Acetone

Table 2.2 – Development recipe for different e-beam resists. For SU-8 a post-exposure bake at 100°C for 2 minutes is necessary.

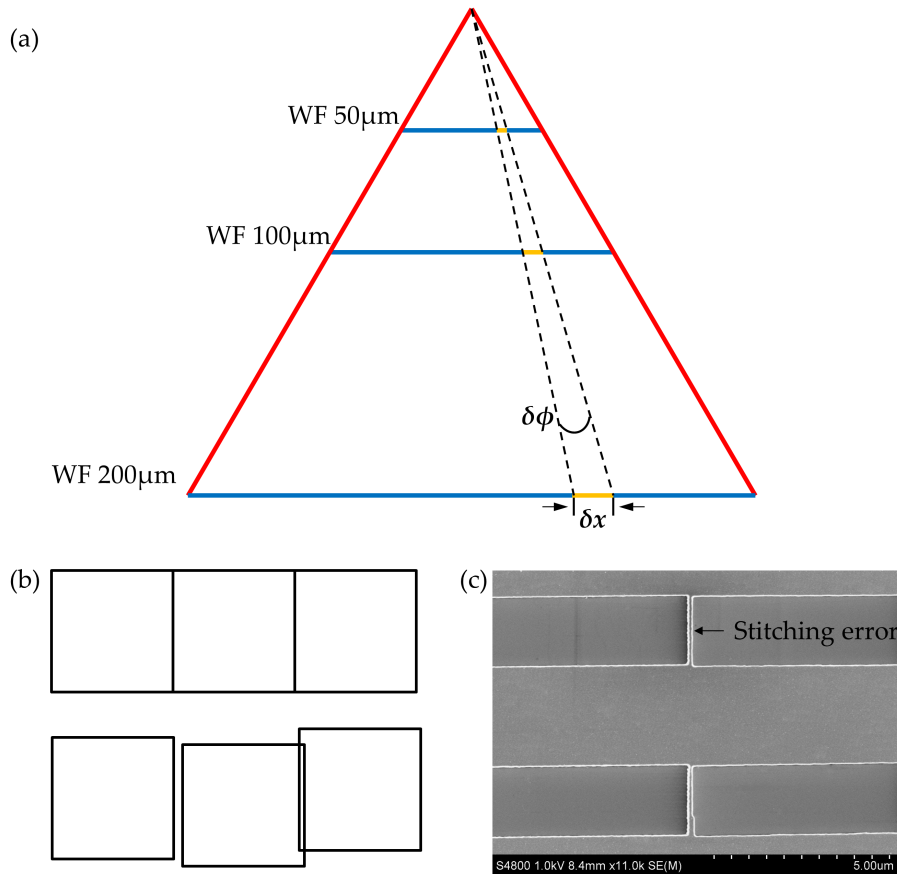


Figure 2.2 – (a) Relationship between write field (WF) and minimum resolution. (b) Relative positions of the write fields with no stitching error and with stitching error, caused by imprecise positioning of the sample stage, respectively. (c) SEM image of a section of a bus waveguide with large stitching error.

which results in a minimum grid spacing of 0.78 nm. For $100 \times 100 \mu\text{m}^2$ write field the minimum grid spacing is 1.56 nm and for the largest available write field of $200 \times 200 \mu\text{m}^2$ the minimum grid spacing is 3.3 nm. Although smaller write fields offer better resolution, it is not always possible to use the smallest available write field, especially while writing a structure larger than the chosen write field. In such case the sample stage is moved to a new position to continue exposing the pattern. This movement is less accurate than the deflection of the e-beam and can lead to positioning errors at the borders between two write fields, known as stitching error. Stitching error often leads to high scattering loss. Figure 2.2b shows the ideal and more realistic positions of the adjacent write fields. In this work, the size of the photonic crystal cavities used was only $20 \mu\text{m} \times 10 \mu\text{m}$. Therefore, the cavity patterns were written using the smallest write field ($50 \times 50 \mu\text{m}^2$) to achieve best resolution without experiencing any stitching error. For writing the mm-long bus waveguides, however, the stitching error could not be avoided. In order to minimize the number of stitching errors, the largest write field ($200 \times 200 \mu\text{m}^2$) is used while writing the waveguides. An example of stitching error in the bus waveguide is shown in Fig. 2.2c.

Another important issue with e-beam lithography is the interaction of the electrons with the e-beam resist and the underlying substrate. When electrons are incident on the resist, they undergo a large series of small scattering events, known as forward scattering, when they transfer energy to the resist and expose it. Besides exposing, the forward scattering also leads to a broadening of the initial beam diameter. The thicker the resist, the stronger is the beam broadening effect due to forward scattering. It is therefore necessary to use the thinnest possible layer of e-beam resist. Such forward scattering also happens inside the substrate. The substrate is also responsible for back scattering a part of the incident electrons, as shown in Fig. 2.3a and 2.3b. By increasing the acceleration voltage, the forward scattering can be minimized, but this increases the amount of back scattering from the substrate to the resist. These back scattered, lower energy, secondary electrons are responsible for undesirable exposure of the surrounding resist. This exposure of surrounding resist leads to the proximity effect. This proximity effect results in incorrect feature sizes in a given pattern. This is very undesirable in photonic crystals and other periodic structures as it changes the spectral response of the structure. A solution to the proximity effect is therefore required to fabricate devices with the designed feature sizes and consequently well-defined spectral features. In our research group, the proximity error correction is done using NanoPECSTM (**P**roximity **E**rror **C**orrection **S**oftware from RAITH), software that calculates the proximity effect and adjusts the exposure dose of each object in the design pattern accordingly. As an example, Fig. 2.3c shows a typical photonic crystal cavity structure used in this work, after proximity error correction. The holes at the center region of a photonic crystal design are assigned low exposure dose to compensate for the back scattered electrons from the neighboring sites, whereas for the holes away from the center relatively higher exposure dose is assigned.

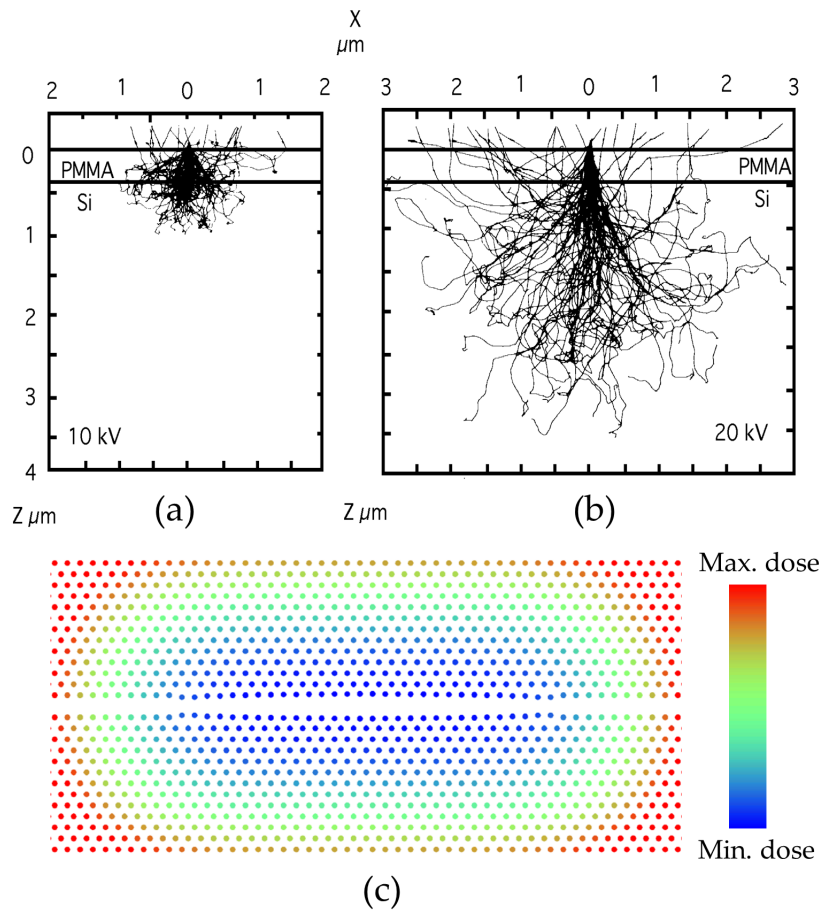


Figure 2.3 – Monte Carlo simulations of the electron distribution during (a) 10kV and (b) 20kV electron beam lithography (both reproduced with permission of the AIP from[90], Copyright 1975). (c) Example of proximity error correction for a photonic crystal cavity structure.

2.4 Reactive ion etching

Once the pattern has been generated by lithography, it is transferred into the material of interest (here: silicon, hydrogen silsesquioxane or silicon nitride) by reactive ion etching (RIE). The sample is placed in a vacuum chamber between two electrodes, as shown in Fig. 2.4a. The top electrode contains a ring, through which the reactive gases are injected into the chamber. By controlling a butterfly valve, the gas pressure inside the chamber is precisely controlled. When an RF field is applied between the two electrodes, the gas mixture ionizes and leads to the formation of a plasma that contains reactive ions that etch the sample. The RF field generates a negative DC component and this DC bias accelerates the positively charged ions towards the sample. Unlike some other dry etching techniques, such as chemically assisted ion beam etching (CABIE), the chemical and physical components of the RIE are interlinked. The DC bias provides a downward directionality and introduces the physical component to the etching process. This DC bias is directly

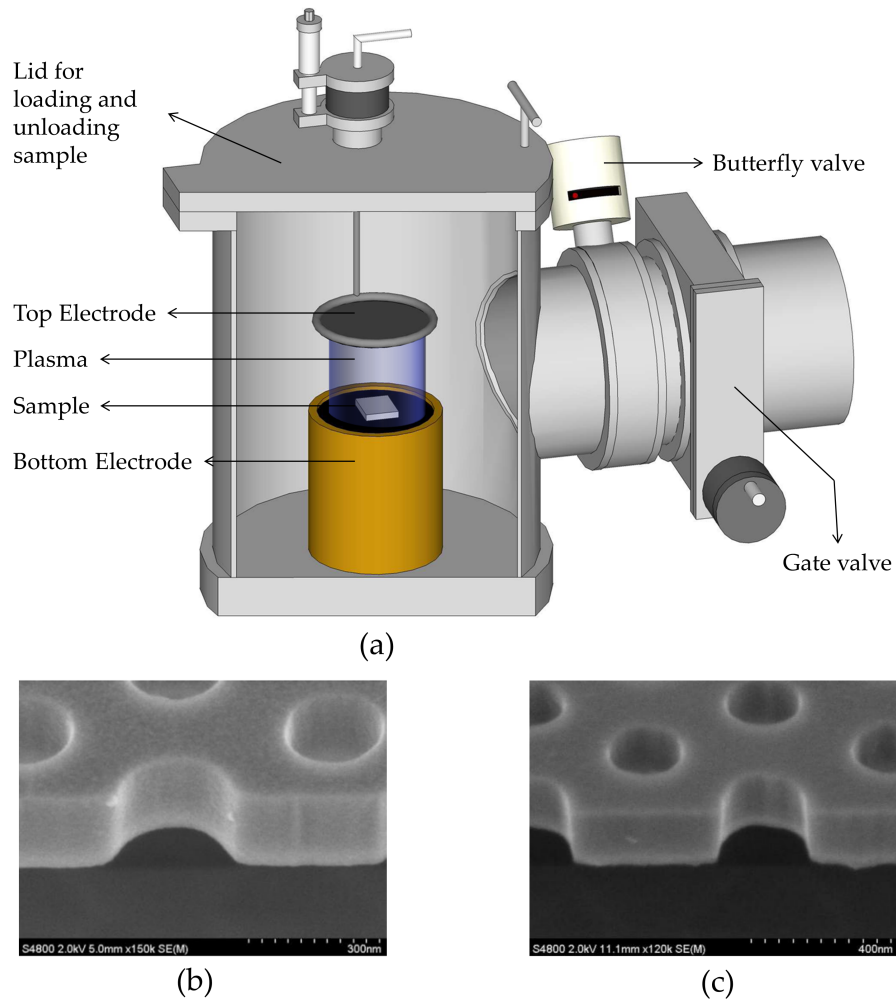


Figure 2.4 – (a) Schematic of the RIE chamber. The gate valve connects the RIE chamber to a turbo pump and the butterfly valve controls the chamber pressure during the etch process. (b) SEM image of a photonic crystal etched with the optimized parameters. Observe the low side wall roughness and the straight side walls. (c) SEM image of a photonic crystal etched with increased RIE chamber pressure. Observe the angled side walls.

dependent on the RF power, which in turn also causes the plasma formation and, therefore affects the chemical component of the etching process.

The gas mixture and etching recipes depend on the corresponding substrate materials. For silicon, a mixture of SF_6 and CHF_3 gases are used. The SF_6 is responsible for the etching and CHF_3 is used to passivate the etched side walls. CHF_3 can polymerize on the sidewalls and thereby protects the sidewalls from being etched. This leads to the desired vertical side walls. Hydrogen silsesquioxane, commercially known as FOx 14 (Flowable Oxide), is very similar to silicon dioxide in composition and contains mostly silicon and oxygen atoms. The reactive gas used for etching hydrogen silsesquioxane is CHF_3 . In this process, the carbon atoms from CHF_3 gas forms the protective coating on the sidewalls as etching proceeds. For silicon nitride

2. FABRICATION TOOLS AND TECHNIQUES

Substrate	Gas mixture	Flow rate (sccm)	Etch pressure (mBar)	RF power (W)	DC bias (V)	Etch rate (nm/min)	Resist Selectivity
Silicon	SF ₆ , CHF ₃	100, 100	5e ⁻²	19	-210	110	1:1
FOx	CHF ₃	100	4e ⁻²	41	-500	20	3:2
Silicon nitride	CHF ₃ , O ₂	100, 25	5e ⁻²	70	-625	40	1:1

Table 2.3 – RIE recipes for different substrates.

etching I also used CHF₃ gas. To facilitate the passivation of the side walls, a small amount of O₂ is added.

As mentioned before, the RIE process consists of both physical and chemical etching components. In order to achieve a good etch result, especially vertical sidewalls, it is necessary to balance both of these components. Any deviation would result in a poorly etched sample. For example, if the etching process is dominated by the chemical component, it loses directionality and consequently leads to an under-etch of the resist mask and angled (“undercut”) side walls. On the other hand, if the physical component of the etching process dominates, then etched materials are sputtered and not properly removed from the sample, which causes angled side walls (“overcut”) or re-deposition on the side walls themselves. Table 2.3 summarizes the optimized RIE recipes used for different substrates.

2.5 Lift-off and metal evaporation

The lift-off process is a simple technique to produce patterned layers of material on a substrate. It is an alternative to etching and is therefore useful in process steps where etching is difficult or not feasible. The primary use of lift-off in this work is the patterning of electrical contacts for active devices, such as modulators and detectors.

In the lift-off process, the substrate is first spin coated with a layer of lift-off resist (LOR 7B) at 4000 rpm and baked at 180°C for 5 minutes. A layer of S1818 is then spin coated on the sample. The desired pattern is then exposed onto the resist using photolithography. The sample is developed for approximately 25 % longer than normal. Here the LOR is also soluble in the S1818 developer MF319. The exposed part of the resist will wash away as usual and the LOR layer in this region will also dissolve. The longer development time leads to an undercut of the photoresist. The desired material (aluminium) is then evaporated onto the sample. The sample is then exposed to the solvent 1165 that will dissolve the photo-resist. The photo-resist washes away, taking the unwanted areas of the evaporated material with it. Finally the LOR layer is removed using acetone and the entire sample is cleaned in IPA. The complete lift-off process is outlined in Fig. 2.5.

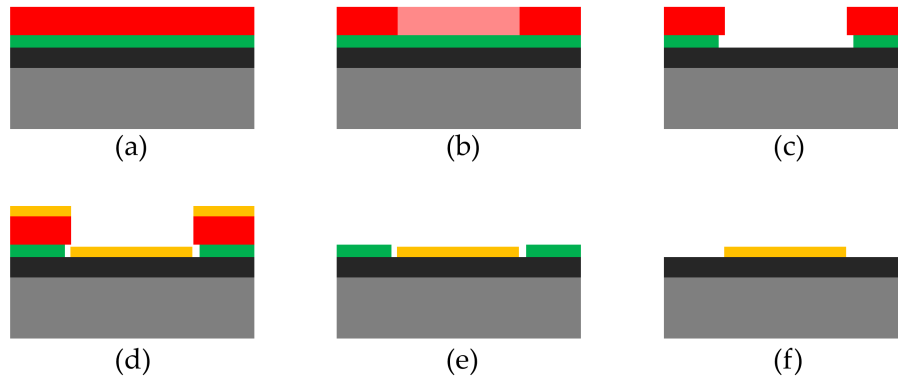


Figure 2.5 – Lift-off process flow: (a) Sample is spun with LOR followed by S1818 photoresist. (b) Sample is exposed under UV light through a photomask. (c) Sample is developed in MF319, which washes away the exposed resist as well as the LOR creating an undercut. (d) Aluminium is evaporated onto the sample. (e), (f) S1818 and LOR is stripped of using solvent 1165 and acetone respectively.

I used a resistive thermal evaporation technique to deposit aluminium. Resistive thermal evaporation is one of most commonly used metal deposition techniques. It consists of vaporizing a solid material (pure metal, eutectic or compound) by heating it to sufficiently high temperatures and recondensing it onto a cooler substrate to form a thin film. As the name implies, the heating is carried out by passing a large current through a filament container (usually in the shape of a coil, boat or crucible) which has a finite electrical resistance. The choice of this filament material is dictated by the evaporation temperature and its inertness to alloying/chemical reaction with the evaporant. This technique is also known as “indirect” thermal evaporation since a supporting material is used to hold the evaporant.

An Edwards E306 thin film coating system was used for the deposition of aluminium as contact metal. A schematic diagram of the system is shown in Fig. 2.6. The system is fitted with an acoustic crystal monitor, which is linked to an Edwards film thickness monitor for controlling the amount of metal deposit. All filament coils used consist of tungsten material. Prior to commencing the evaporation, the base pressure was maintained below 1×10^{-6} mBar. A 200 nm thick layer of aluminium is deposited at a deposition rate of 0.1 nm/sec. The average current required to evaporate the metal was 1 A.

2.6 Summary

In this chapter I have discussed the main fabrication processes needed to fabricate the samples described in other chapters. A description of the complete fabrication process specific to an individual device is discussed later in the relevant chapters. For exposing large areas such as alignment marks, ion implantation windows, contact vias, lift-off windows photolithography technique is used and for exposing submicron features, such as photonic crystals

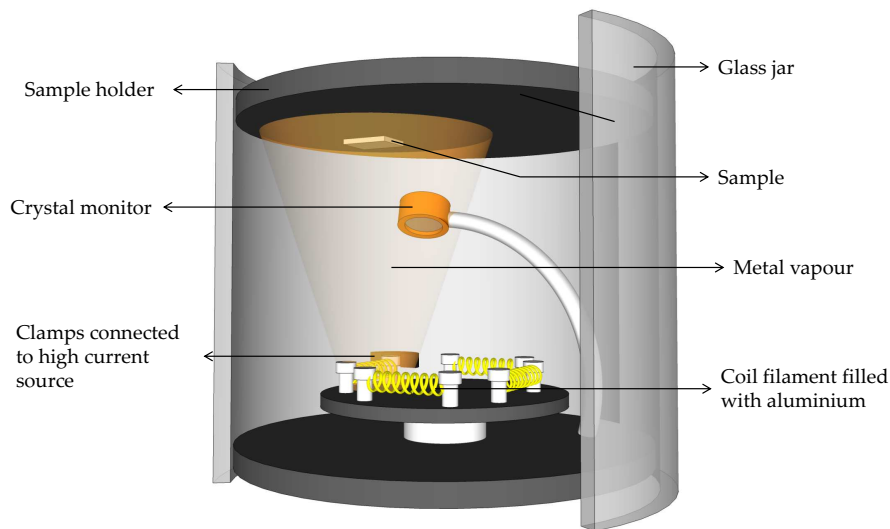


Figure 2.6 – Schematic of the thermal evaporator chamber

and waveguides e-beam lithography is used. For transferring some of the exposed patterns (e.g. alignment marks, photonic crystal structure, waveguide structure, contact vias), RIE technique is used. The aluminium contact formation was carried out using thermal evaporation. Some of the fabrication steps were carried out in collaboration with other universities. For example, the ion implantation system of University of Surrey was used for doping purposes. Silicon nitride deposition was done in University of Sheffield using plasma-enhanced chemical vapor deposition (PECVD) system. The ion implantation process required for defect detectors was carried out in McMaster University.

Chapter 3

Photonic Crystal Cavity Based Optical Filter

3.1 Introduction

In the field of integrated photonics, miniaturization of the optical components is one of the key motivations for research. Reduction in device size offers significant improvement in terms of integration density and energy consumption. Such reduction can be achieved by increasing the light-matter interaction through resonances; as a result, we are seeing a growing interest in resonance based devices for different optical components, such as narrow band optical filters [91], modulators [67, 72], detectors [92], multiplexers [81] and routers [93]. In integrated photonic circuits, resonance based devices are traditionally implemented as a planar configuration using coupled waveguide-resonator architectures. Their wavelength selective nature also makes them ideal for dense wavelength division multiplexing (WDM) applications. So we can summarize the key attributes of an ideal waveguide-resonator system as:

- Small device foot print (to increase the integration density)
- High quality factor (for narrow band operation)
- Low mode volume (for low energy operation)
- Large extinction ratio (to increase the system SNR)
- Low coupling loss (to reduce the insertion loss)
- Large Free Spectral Range (for channel scalability)

There are primarily two types of resonators used in such systems: traveling wave resonators e.g. micro-ring resonator and micro-disk resonator, and standing wave resonator e.g. Fabry-Pérot resonator and photonic crystal cavity resonator. Waveguide-resonator systems based on traveling wave resonators, where both the resonator and the waveguide are monolithically fabricated on the same platform, have been the subject of a large volume of recent research. The primary reasons behind their popularity are their high

extinction ratio and high quality factor. However, their limited Free Spectral Range (FSR) restricts the scalability i.e. the number of channels that can be multiplexed when used in a WDM system. Besides, silicon based planar structures incur considerable optical coupling loss due to the large refractive index mismatch between silicon waveguide and the optical fiber.

On the other hand, photonic crystal cavities have the ability to strongly confine light in both space and time [94]. This provides compact devices with high quality factors and enhanced light matter interaction. The design of two dimensional photonic crystal cavities with ultra-low mode volume and ultra-high quality factor [73, 95, 96] and large FSR operation (in case of single mode cavity [73, 95]) is relatively mature. Nevertheless, due to their ultra-small mode volume, efficient coupling of light in and out of the cavity is challenging making the overall extinction ratio of such device low for any practical application.

This chapter introduces a new coupling technique by which the overall performance of a waveguide-resonator system can be significantly improved. This design is based on a low refractive index waveguide vertically coupled to a photonic crystal cavity. The motivation behind using photonic crystal cavity is threefold, namely (a) high quality factor, (b) low mode volume and (c) large free spectral range (FSR). Additionally, the vertically coupled architecture I introduce offers some unique advantages, such as high extinction ratio, reduction in optical loss and ease of multiplexing of several waveguide-resonator systems. This chapter begins with a brief introduction to some fundamental concepts concerning photonic crystals in general and two dimensional photonic crystal cavities in particular. Using temporal coupled mode theory, I formulate the design requirements for an efficient waveguide-resonator system. Then I discuss the fundamental limitations associated with existing coupling techniques for photonic crystal cavities and how vertical coupling can resolve these issues. And finally I experimentally demonstrate the efficient optical filter response of a photonic crystal cavity using the vertical coupling technique.

3.2 Photonic crystal

A photonic crystal structure (also referred to as photonic band gap material) is an artificial periodic structure of dielectric materials that control electromagnetic wave in the same way as the periodic potential in a semiconductor material affects the motion of electrons in a crystalline material by defining allowed and forbidden electronic energy bands. The concept of optical periodic structures and their effect on electromagnetic waves is not new and has been studied for over 100 years. The earliest study of electromagnetic wave propagation in a periodic medium can be traced back to the year 1888, when Lord Rayleigh studied the unusual reflective properties of a crystalline mineral [97]. Throughout the twentieth century, one-dimensional periodic multilayer structures have been studied extensively [98] and nowadays have several applications, for instance as anti-reflection coating, as Fabry-Pérot filter, and in distributed feedback lasers. Traditionally, periodic multilayer

dielectric structures were studied as ideal reflectors and were analyzed by considering the sum of multiple reflections and refractions that occur at each interface. In 1987, however, Yablonovitch [99] first investigated such dielectric periodic structures using the language of solid state physics and comparing periodic optical structures with the periodic potential experienced by electrons in semiconductor materials. He then established that this kind of periodicity can give rise to forbidden gap in the electromagnetic spectrum just as the electronic spectrum has a band gap in crystalline semiconductors. By extending the periodicity to higher dimensions, photonic band gaps can be achieved in a plane (for two dimensional periodicity) or in all directions (for three dimensional periodicity).

3.2.1 Origin of photonic bandgap: a 1D example

Following a similar analysis presented in [100], here we explore qualitatively the formation of a photonic bandgap for the simplest one-dimensional case. Figure 3.1a shows a multilayer film, in which the dielectric function varies periodically with periodicity a in z direction (i.e. $\varepsilon(z)=\varepsilon(z+la)$) and is homogeneous in xy plane. The wave vector \vec{k} of the electromagnetic wave propagating through the structure is parallel to the z direction.

In any periodic structure, the propagation of wave obeys Bloch-Floquet theorem [101]. And in case of a multilayer film the optical modes can be expressed in the form of Bloch waves as

$$E_k(z) = u_k(z)e^{-ikz} \quad (3.1)$$

$u_k(z)$ is a periodic envelope with periodic property $u_k(z) = u_k(z+la)$, where l is an integer. If we now replace the wavenumber k with $k + 2\pi/a$ in Eq. 3.1, we get

$$E_{k+2\pi/a}(z) = \left(u_{k+2\pi/a}(z)e^{-i2\pi z/a}\right) e^{-ikz} \quad (3.2)$$

Here we can recognize that the term inside the parenthesis is a periodic function, which suggests that k is also a periodic function satisfying the condition $k' = k + 2m\pi/a$, where m is an integer.

If we consider a homogeneous medium with $\varepsilon = 1$, the dispersion relation will simply be $\omega(k) = ck$ as shown by the solid blue lines in Fig. 3.1b. If we also imagine an arbitrary periodicity a within the medium, then the dispersion relation will replicate itself at $k' = k + 2m\pi/a$, as shown by the dashed blue lines in Fig. 3.1c. Due to this artificial periodicity, the dispersion curves cross at $k = \pm\pi/a$, creating a degeneracy. We can express the two degenerate modes as $E(z) \sim e^{\pm i\pi z/a}$ or equivalently in linear combinations $e(z) = \cos(\pi z/a)$ and $o(z) = \sin(\pi z/a)$, both with frequency $\omega = c\pi/a$.

If ε is then perturbed with periodicity a , for example with a sinusoid $\varepsilon(z) = 1 + \Delta\cos(2\pi z/a)$, the artificial degeneracy between $e(z)$ and $o(z)$ will be broken. And due to the discrete translation symmetry imposed by the nontrivial periodicity, there are only two possible ways we can place the modes in the structure, as shown in Fig. 3.1a. We can either position the nodes (of the modes) in each low- ε region or in each high- ε region. In general,

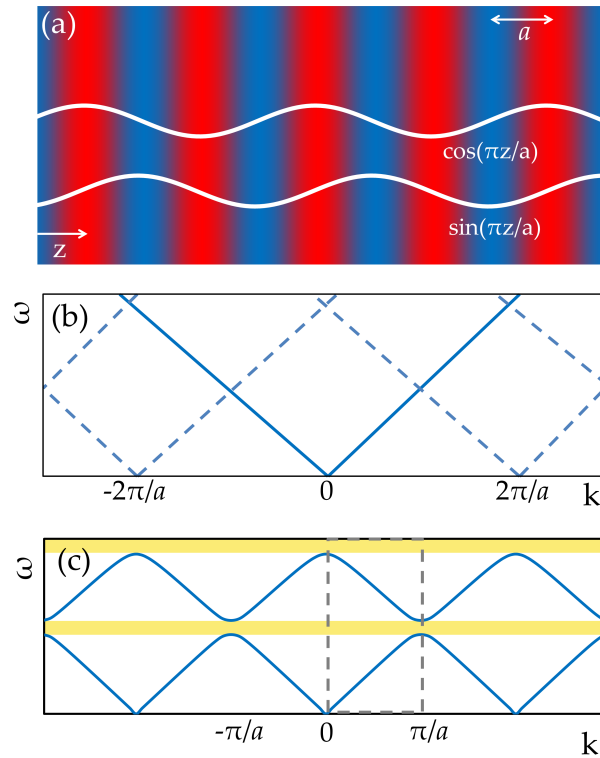


Figure 3.1 – (a) A sinusoidal distribution of ϵ , where red denotes the higher ϵ region and blue denotes the lower ϵ region. Two possible mode distributions at $k = \pm\pi/a$ relative to the structure are also shown. Lower frequency tends to concentrate in the higher ϵ region and higher frequency tends to concentrate in the lower ϵ region. (b) Dispersion relation between ω and wavenumber k of a homogeneous one dimensional medium (solid blue lines), any assumed periodicity will replicate the dispersion relation at $k' = k + 2m\pi/a$ (dashed blue lines). (c) Dispersion relation of a real periodic variation of ϵ , where a photonic band gap (yellow region) is opened due to the splitting of the degeneracy at $k = \pm m\pi/a$.

low frequency modes tend to concentrate their energy in high index material and high frequency modes concentrate theirs in low index material [100]. As a result, a frequency range will be created where no mode is allowed as shown in Fig. 3.1c. This frequency range is called photonic bandgap and the gap increases as refractive index contrast Δ increases.

In the dispersion relation (also known as the band diagram), we can identify a region $k = \pm\pi/a$, which replicates itself periodically with a period $k = 2\pi/a$. Hence, to study any reciprocal periodic medium it is sufficient to consider only this region, which is called the first Brillouin zone. Further, inside the Brillouin zone, the bands have mirror symmetry with respect to $k = 0$, hence the first Brillouin zone can further be reduced to the irreducible Brillouin zone ($0 < k < \pi/a$), as shown by the dashed box in Fig. 3.1c.

3.2.2 Two dimension photonic crystal

One of the most commonly used periodic structures in planar integrated photonic circuits is the two dimensional triangular lattice structure. A two dimensional photonic crystal has dielectric periodicities along two of its axes (say, the xy plane) and is homogeneous along the third axis (say, z axis). The optical fields in two dimensional photonic crystals can be divided into two polarization groups: TM (transverse magnetic), in which the electric field is perpendicular to the plane of periodicity and the magnetic fields are parallel and TE (transverse electric), in which electric fields are parallel to the plane of periodicity and the magnetic field is perpendicular [100].

The band diagram of a triangular lattice is shown in Fig. 3.2 for both TE and TM polarizations. The structure considered here is a triangular lattice of air holes in a high index material ($n=2.8$). The hole radius is $r = 0.28a$, where a is the period of the lattice. The band diagram is calculated using the plane wave expansion method. The left inset shows the unit cell of the triangular lattice and the right inset shows the first Brillouin zone (hexagone) with the irreducible Brillouin zone shaded in yellow (due to the six-fold symmetry of the lattice). The irreducible Brillouin zone is a two-dimensional region of wave vectors, so the bands are actually surfaces. Here the band diagram is calculated only for those wave vectors which lie on the side of the irreducible Brillouin zone, i.e. along Γ -K-M- Γ . These points in the irreducible Brillouin zone are called key symmetry points. Most of the time, photonic band gap arises between key symmetry points. So it has become a common practice to calculate the band diagram along the side of the irreducible Brillouin zone. Here, we note that unlike in one-dimensional photonic crystals, where any periodic variation of ε will produce a photonic band gap, two dimensional photonic crystals may or may not achieve complete photonic band gap under all circumstances. This is apparent in Fig. 3.2, where the TE polarization (red curves) has a complete band gap in the range $0.25 < a/\lambda < 3$, while the TM polarization does not.

3.2.3 Localization of light using defects

In the previous section, we saw that the TE polarization can experience a complete photonic band gap in the triangular lattice structure. Within this band gap, no modes are allowed to propagate in any direction in the xy plane and the density of states (number of modes per unit frequency) is zero. The true meaning of a band gap is that the wave vectors in this region are complex and an electromagnetic wave, with frequency inside the band gap, will simply decay exponentially inside the structure.

From semiconductor physics, we know that once any defects are inserted in an otherwise perfect lattice structure, new electronic states appear inside the band gap, associated to the breaking of symmetry in the lattice structure. Similar effects can be seen in photonic crystals. By perturbing the symmetry of the lattice structure, say by removing a hole from a triangular lattice (point defect), a localized mode can be created with its frequency inside the forbidden gap of the photonic crystal. This defect related photonic mode

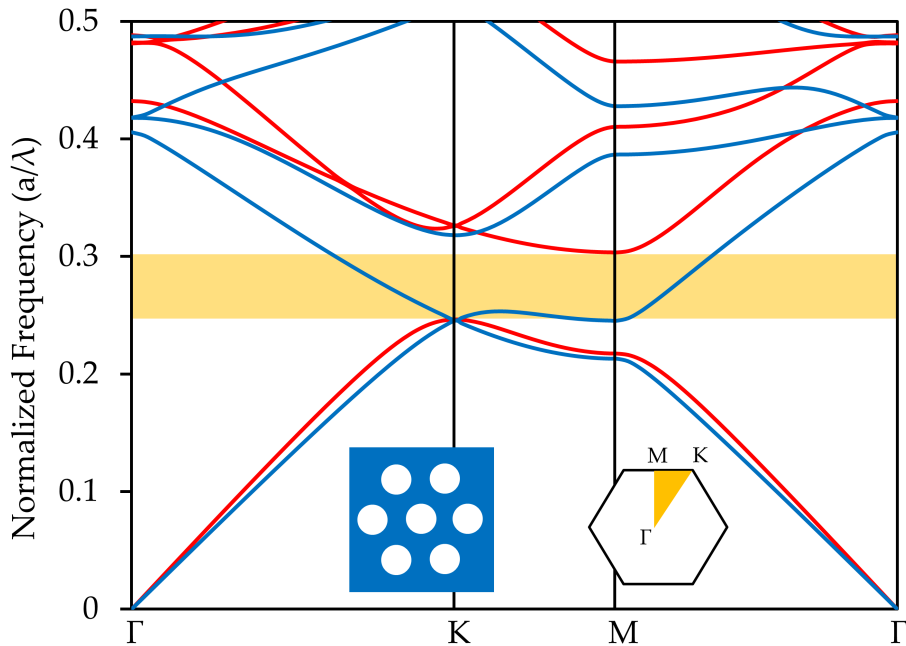


Figure 3.2 – Band diagram of a triangular lattice structure with background material index $n=2.8$ and hole index $n=1$. The band diagram is calculated for the wave vectors lying on the sides of the irreducible Brillouin zone (highlighted by yellow). The red and blue bands correspond to TE and TM polarizations respectively.

cannot propagate in rest of the crystal, because there it falls within the band gap. Therefore this mode is spatially localized where the physical defect lies. So the mode decays exponentially and evanescently out of the defect. The boundaries of the defect actually act as mirrors and therefore the point defect is nothing but a cavity for the photons, because light cannot escape from it.

Figure 3.3a shows a triangular lattice of holes with a single missing hole at the center. This structure forms a micro-cavity at the defect site, which can confine a localized state. Without the defect, a complete band gap appears in the frequency range of $0.25 < a/\lambda < 3$ for TE polarization, as shown by the green curves in Fig. 3.3b. After the defect is introduced, an optical mode (shown in red) appears inside the band gap. Essentially, this suggests that the mode inside the cavity will experience a photonic band gap in all directions (for any value of k) and will be forced to localize within the cavity, as shown in Fig. 3.3c.

Mode volume and quality factor are the two most important properties of any cavity. The mode volume¹ represents the spatial extent and the energy density of the optical mode inside the cavity, while the quality factor of a cavity represents the strength of confinement of the optical mode inside the cavity and is generally defined in terms of the ratio of energy stored in the

¹Mode volume is defined as $V = \int \epsilon(r) |E(r)|^2 d^3r / \max[\epsilon(r) |E(r)|^2]$, where $\epsilon(r)$ is the dielectric constant and $E(r)$ is the electric field.

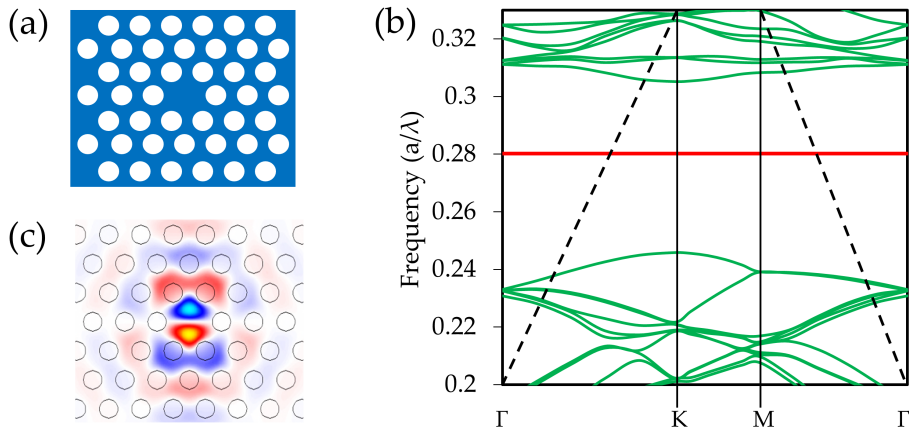


Figure 3.3 – (a) A point defect cavity formed by removing one hole from an otherwise perfect two dimensional triangular lattice structure. (b) Due to the introduction of the defect, a new photonic band appears inside the band gap, which corresponds to the localized mode in the cavity. The bands corresponding to the perfect lattice are shown in green and the defect mode is shown in red. The dashed lines (known as light line) denotes the boundary between bound modes and radiation modes for a three dimensional structure (c) This point defect cavity has three trivial degenerate modes, corresponding to the three symmetry axes of the triangular lattice, one of them is shown here.

cavity to the energy lost per cycle². Cavities with large quality factor and small mode volume are particularly interesting in many fields of photonics because they afford an increase in light-matter interaction. Due to the unique photonic band gap property that translates into very high mirror reflectivity, an extremely small mode volume, of the order of the wavelength of the electromagnetic wave, can be achieved while maintaining a very high quality factor. For instance, if we consider an ideal situation where a point defect cavity is located in an infinitely extended two dimensional photonic crystal, the optical mode is completely confined within the defect and unless there is any other loss mechanism present, the quality factor of the cavity will be infinity and at the same time will not depend on the size of the defect.

So far we have only discussed two dimensional photonic crystals that are infinitely extended in the direction perpendicular to the plane of periodicity. In reality, photonic crystals are fabricated with a finite height and known as photonic crystal slabs that confine light in the vertical direction by total internal reflection. If we consider a two dimensional photonic crystal slab which is suspended in a medium with refractive index n_{clad} , the optical mode confinement inside the slab is only possible if the vertical component of the wave vector i.e. \vec{k}_z is imaginary outside the slab. Therefore, we can define a condition for which the optical confinement in the structure is possible

$$k_{in-plane} = \sqrt{k_x^2 + k_y^2} > n_{clad}\omega/c \quad (3.3)$$

²Quality factor is also defined as $Q = \omega_o/\Delta\omega$, where ω_o is the angular frequency at resonance wavelength and $\Delta\omega$ is the full width at half maxima. The relationship between quality factor and the mode decay rate (Γ) in the cavity is expressed as $Q = \omega_o/2\Gamma$.

This condition is shown by the dashed line in Fig. 3.3b, which is called the light line. For a two dimensional photonic crystal cavity, the region of the dispersion relation, where Eq. 3.3 is not satisfied is called the light cone. Any optical mode outside the light cone is guided in the structure and modes inside the light cone are able to radiate into the surrounding material.

If we go back to the photonic band (red curve) corresponding to the point defect cavity, we notice that a large section of this band lies within the light cone, which implies that the cavity mode contains plane wave components with in-plane wave vectors that do not satisfy the condition in Eq. 3.3. As a result, although the cavity mode is perfectly confined in the xy plane by the in-plane photonic band gap, its energy will be lost due to vertical radiation.

We can describe the contribution of the different decay rates to the total quality factor by simply adding up the decay rates and realizing that $\Gamma \sim 1/Q$, i.e.

$$\frac{1}{Q_o} = \frac{1}{Q_{\parallel}} + \frac{1}{Q_{\perp}} \quad (3.4)$$

Where Q_o is the total quality factor of the cavity and Q_{\parallel} and Q_{\perp} are the quality factors associated with in-plane and vertical energy decay, respectively. For a point defect, a high value of Q_{\parallel} can easily be obtained by increasing the number of lattice periods of the photonic crystal surrounding the point defect. Due to the presence of a large number of plane wave components inside the light cone, however, Q_{\perp} is relatively small which leads to an overall low quality factor of the cavity. As a result, achieving a high quality factor in an ordinary point defect is not possible. In the next section we will discuss some of the techniques that are used to reduce the vertical energy decay and hence increase the quality factor of a cavity based on photonic crystal slab.

3.3 High quality factor photonic crystal cavity

3.3.1 Gentle mode confinement

Because of the photonic band gap effect, optical modes in the photonic crystal cavities are highly localized in real space, which leads to a broad distribution in Fourier space or k-space. In other words, these cavity modes contain a large number of plane wave components. The general rule for designing a high quality factor cavity is therefore to reduce the number of plane wave components of the cavity mode that lie within the light cone.

Let us consider a cavity of a dielectric material in the xy plane. The cavity is closed on both sides by two perfect mirrors which confine light in the x direction; along the y-direction, light is confined by index guiding (Fig. 3.4a). The strength of the optical mode confinement along the y-axis can be studied by decomposing the electric field in the cavity into a set of plane wave components by spatial Fourier transformation. According to Eq. 3.3, if the tangential component (\vec{k}_x) of the wave vector of any plane wave lies

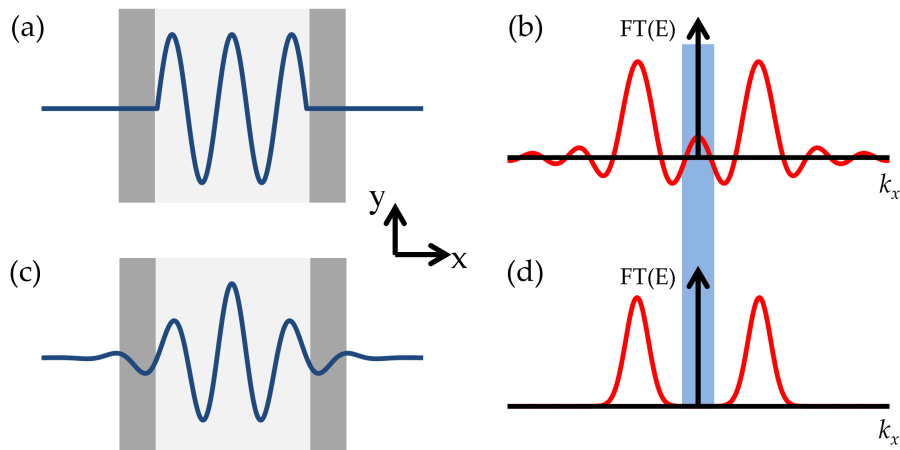


Figure 3.4 – (a) Electric field distribution inside a cavity with rectangular envelope function and (b) spatial Fourier transform of the electric field. (c) Electric field distribution inside a cavity with Gaussian envelope function and (d) the spatial Fourier transform of the electric field. The blue area indicates the leaky region ($0 < k < n_{clad}2\pi/\lambda_o$).

within 0 to $n_{clad}2\pi/\lambda$, the wave can escape into the surrounding cladding layer leading to weak confinement.

The electric field distribution inside the cavity can be expressed as a product of the fundamental sinusoidal wave with resonance wavelength of the cavity (λ_o) and an envelope function $F(x)$ that is determined by the structure of the cavity. In this case, the envelope function is a unit rectangular function. Hence the Fourier transform of this electric field distribution is a superposition of two sinc functions located at $k_x = \pm n_{mode}2\pi/\lambda_o$. In Fig. 3.4b, we can see that even though the plane wave component with peak intensity is outside the leaky region, due to the abrupt change in the envelope function at the edges of the cavity, plane wave components inside the leaky region also have significant intensity which leads to a large radiation loss.

Therefore, we can conclude that in order to reduce the intensity inside the leaky region, the envelope function should have a gentler profile at the edges rather than an abrupt one. For example, if the envelope function has a Gaussian profile, the Fourier transform of the electric field distribution will also be composed of a superposition of two Gaussian functions located at $k_x = \pm n_{mode}2\pi/\lambda_o$. As we can see in fig. 3.4c and 3.4d, this changes the situation drastically and the plane wave components inside the leaky region have very small intensity distribution. This analysis suggests that the quality factor of a cavity can be increased significantly by tailoring the structure of the cavity while maintaining a small mode volume.

3.3.2 Gentle confinement in an Ln type cavity

Ln type cavities are realized by removing n holes completely along the Γ -K direction of a triangular lattice. The point defect cavity discussed in Section 3.2.3 is a L1 type cavity, which shows a single localized mode within the

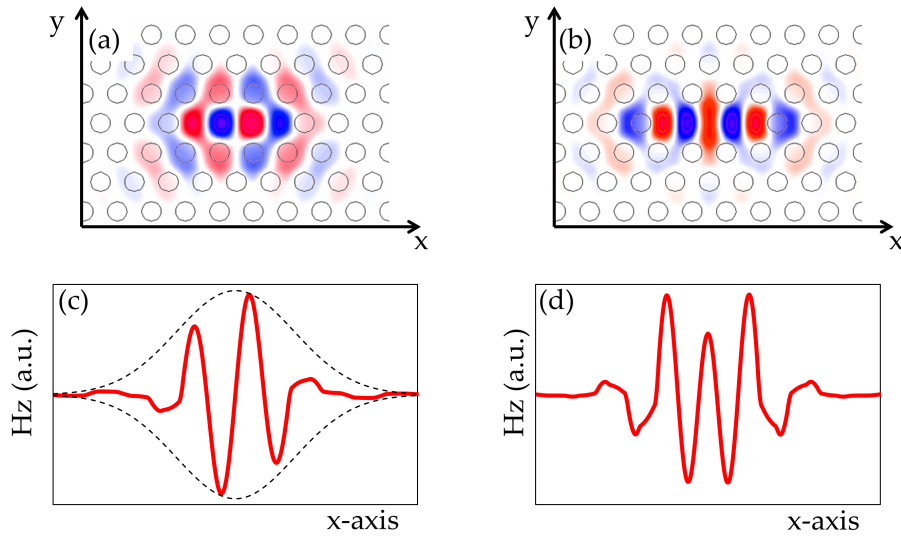


Figure 3.5 – Magnetic field (H_z) distribution of (a) the first order mode and (b) second order mode of an L3 cavity. (c) Profile of (a) along the center line of the cavity (red curve) and the profile of an ideal Gaussian envelope (dashed curve). (d) Profile of (b) along the center line of the cavity.

photonic band gap. Due to its small mode volume, it contains significant amount of plane wave components inside the leaky region. As a result, the quality factor of an L1 cavity cannot be high. One way to improve the quality factor is to remove a few more holes, so that most of the electric field can be accommodated inside the cavity and the electric field experiences less of an abrupt transition at the edges of the cavity. The removal of more holes has an adverse effect on the mode volume and the mode number of the cavity, however. For example, when three holes are removed (referred to as an L3 cavity) more modes appear inside the photonic band gap because a larger cavity can accommodate more modes. Typically, however, the increase in mode volume is more than compensated by the increase in Q-factor, which is why L3 and similar type cavities have proven to be very popular in the field.

Regarding the Q-factor of the different modes accommodated by the cavity, the lowest frequency mode (first order mode) tends to be the mode with the highest Q-factor. This can be understood by considering the mode profile inside the cavity. For the first order mode, the combination of the guided mode at the center of the cavity and the exponentially decaying part at the boundaries results in a Gaussian like field distribution (as shown in Fig. 3.5a and 3.5c), resulting in a high Q-factor. For higher order modes, however, the field profiles are more complex and their envelopes do not follow a simple Gaussian profile (as shown in Fig. 3.5b and 3.5d). As a result, the Q-factor of the cavity at these modes is lower.

The envelope of the field distribution of the first order mode follows a Gaussian profile at the center of the cavity. Due to the strong interaction between the field and the holes at the boundaries in the lateral direction

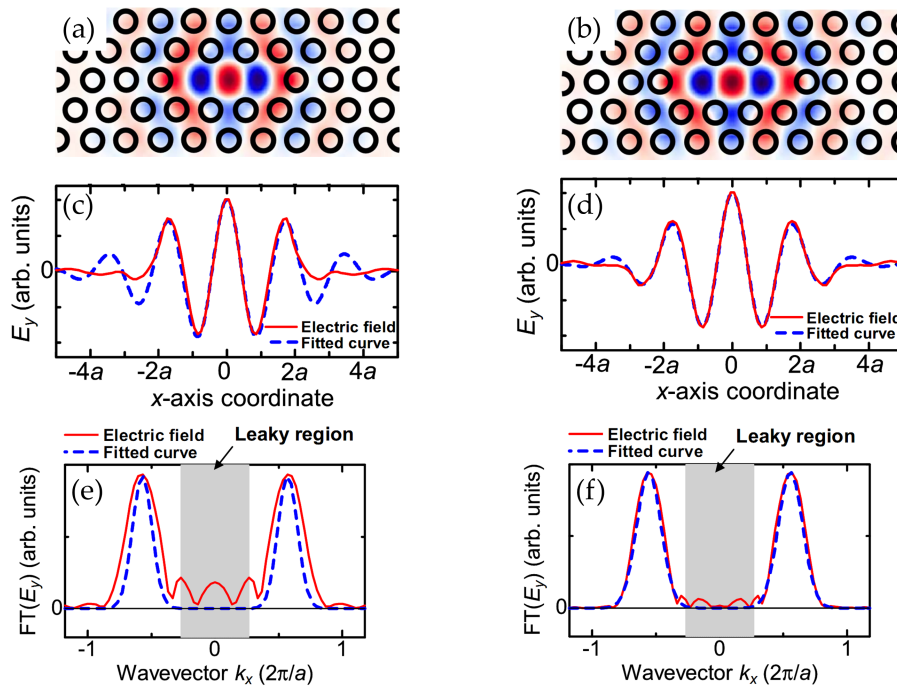


Figure 3.6 – (a), (b) Electric field (E_y) distribution of the fundamental mode of an L3 cavity without and with displacement of air holes at both edges. (c), (d) The profile of (a) and (b) along the center line of the cavity (red curves) and the Gaussian fit (dashed curve). (e) and (f) 1D Fourier transform of the field profiles (red curves) with Gaussian fit (dashed curve). (reproduced with permission of the OSA from [103], Copyright 2005)

(x -axis), the envelope deviates significantly from an ideal Gaussian function, as shown in Fig. 3.5c, which introduces radiation inside the leaky region. One possible way to improve the shape of the field envelope is to fine-tune the parameters (such as position or size) of the holes at the cavity boundary.

The concept of gentle confinement was first proposed by Akahane et al. [102], where they showed that by tuning the position of the first two holes on both sides of an L3 cavity, it was possible to achieve a more Gaussian-like field envelope and thereby to reduce the intensity inside the leaky region. Fig. 3.6 shows the dominant electric field (E_y) profiles in the cavity and their corresponding k -space distribution, with and without the displacement of the air holes at both edges. Due to this modification in the cavity structure, fewer Fourier components appear inside the leaky region (compare Fig. 3.6e and 3.6f). By optimizing the position of the air holes Akahane et al. showed that the quality factor of the cavity can be increased from 2,500 to 45,000, while keeping the mode volume almost constant at $0.69(\lambda_o/n)^3$. They have also shown that further improvement in the quality factor can be achieved by tuning the positions of more holes. In [103] they reported a quality factor of 100,000 by tuning six holes at the cavity edges.

3.3.3 Line defect photonic crystal cavity

Although a significant improvement in quality factor can be achieved by fine tuning the air-holes in an Ln type cavity, uniform and precise control of the electric-field distribution throughout the cavity is difficult, which is a necessary requirement to form a Gaussian like profile. The reason lies in the fact that the tails of the electric field still experiences a strong index modulation arising from the presence of air holes. One way to achieve a more Gaussian-like field profile is by confining the cavity mode via a mode gap rather than via the photonic band gap effect directly.

3.3.3.1 Heterostructure cavity

The concept of mode gap was first introduced by Song et al. [95] using a double-heterostructure photonic crystal. The basic photonic crystal environment exploited to construct the double-heterostructure was a two dimensional silicon photonic crystal slab with a triangular lattice and a line-defect waveguide formed by a missing row of air holes in the Γ -J direction (this is similar to the Γ -K direction on the Brillouin zone shown in Fig. 3.2a), as shown in Fig. 3.7a. The corresponding band diagram is shown in Fig. 3.7b. It can be seen that a waveguide mode is formed within the band gap region. The upward arrow indicates the transmission region, where propagation is allowed through the waveguide, and the downward arrow indicates the mode-gap region, where propagation is prohibited. Fig. 4.7c shows the double-heterostructure formed by two triangular-lattice photonic crystals (PhC-I and PhC-II) with different lattice constants. The lattice constant of PhC-I is a_1 . For PhC-II, the lattice constant is a_2 ($a_2 > a_1$) in the Γ -J direction but still a_1 in the Γ -X direction in order to maintain the lattice continuity. This lattice constant difference between PhC-I and PhC-II leads to different transmission and mode-gap regions, thus forming a region where photons are confined in the waveguide of PhC-II, as shown in Fig. 3.7d. It is very interesting to note that, by using this design, the photonic confinement in Γ -J direction is not directly provided by the photonic bandgap effect, but it is instead a consequence of the mode-gap effect in the waveguide of PhC-I, which is due to the mismatch in lattice constant between the two regions. The theoretically calculated Q-factor of the double-heterostructure cavity is $>24 \times 10^6$, i.e. two order of magnitude higher than that of the modified L3 cavity. The corresponding modal volume is as small as $1.2(\lambda_o/n)^3$. The experimentally demonstrated Q factor of this photonic double-heterostructure cavity was 6×10^5 in silicon with air cladding.

3.3.3.2 Linewidth modulated cavity

In 2006, Kuramochi et al. demonstrated that ultra-high Q can be achieved by modulating the width of a line defect locally [73]. The design concept is to increase the waveguide width at the center of the cavity by shifting the surrounding holes away from the waveguide. The corresponding design is shown in Fig. 3.8a, where holes labeled as A, B and C are moved away

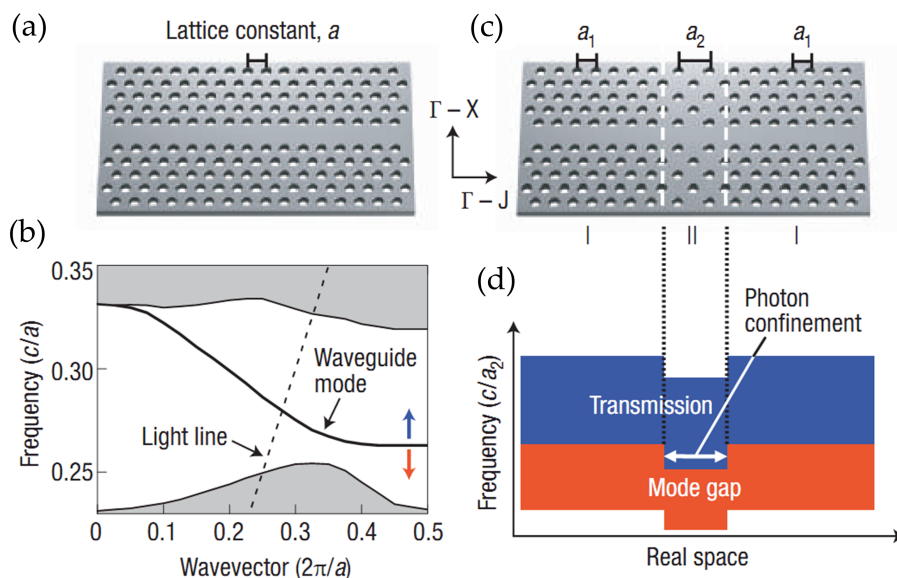


Figure 3.7 – (a) A line defect in a triangular lattice formed by a missing row of air holes in the Γ -J direction. (b) The calculated band structure of (a). (c) Double heterostructure formed by assembling the basic PhC structures I and II with different lattice constants. (d) Schematic of the band diagram along the waveguide direction. (reproduced with permission of Macmillan Publishers Ltd: Nature Materials from [95], Copyright 2005).

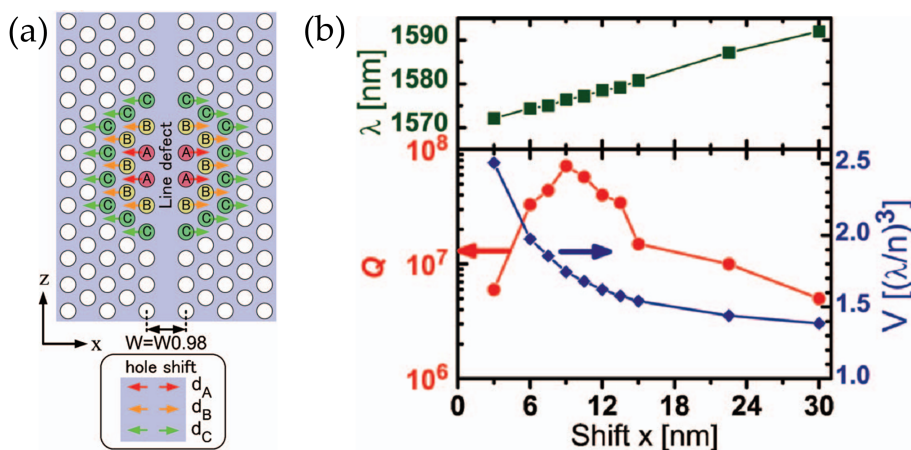


Figure 3.8 – (a) A line width modulated cavity created by shifting holes outwards in a W0.98 waveguide, where shift $d_A = x$, $d_B = 2x/3$ and $d_C = x/3$. (b) Shift in resonance wavelength and calculated Q-factors and mode volume for different values of x . The maximum Q-factor is achieved at about $x = 9$ nm with decreasing mode volume. (Reproduced with permission of the AIP from [73], Copyright 2006).

from the center by a distance of d_A , d_B and d_C ($d_A > d_B > d_C$) respectively. Using this line width modulation technique, Kuramochi et al. experimentally demonstrated a record quality factor value of 2×10^6 . The theoretical quality factor was 7×10^7 with an estimated mode volume of $\sim 2.5(\lambda_o/n)^3$.

Both the heterostructure and linewidth modulated cavities give an extremely high quality factor with a very small mode volume. In addition, due to the small physical size of these cavities, they confine only one optical mode within a very large wavelength range. The single mode operation of these cavities offers a significant advantage over other resonators, such as ring or micro-disc, when used as optical components in WDM systems, because of the very large free spectral range and the low energy required to actuate the cavity. For example single mode operation with these cavities over a wavelength range of more than 100 nm [73, 74] has been demonstrated, hence the channel scalability of a WDM system improves significantly.

One disadvantage with these cavity designs is that they require a very precise electron-beam writing and fabrication. For example, in case of a linewidth modulated cavity, the maximum quality factor is achieved with $d_A = 9$ nm, $d_B = 6$ nm and $d_C = 3$ nm, which suggests that a very small positional error will have a significant influence on the cavity characteristics. The fabrication imperfection may explain why the theoretical quality factor of this cavity is 7×10^7 with an experimental value of about 2×10^6 [73]. For the double heterostructure cavity as well the quality factor drops from 24×10^6 to 6×10^5 [95]. For most practical purposes, however, a quality factor of the order of 10^4 is sufficient.

3.3.3.3 Dispersion adapted cavity

Although both the heterostructure and the linewidth modulated cavities offer high quality factors, the design rules for both of them are somewhat unsystematic. For example, in both cases, the optimum design parameters for maximum quality factor are decided either by modifying the lattice period or by shifting the holes arbitrarily. In 2012, Welna et al. [96] proposed a new photonic crystal cavity design which is based on a more systematic approach of combining numerical and analytical methods. This design is an extension of the linewidth modulated cavity design. The idea is to use hole-shifts for a non-arbitrary mode confinement, where individual hole-shifts are applied to adapt the dispersion curve for a Gaussian mode envelope to achieve high quality factor. Figure 3.9a shows the mode profile (dominant electric field) of the first order cavity mode superimposed onto the cavity design and Fig. 3.9b shows the cross section of the intensity profile of the electric field along $y=0$. We notice that the field profile matches quite nicely with a Gaussian envelope function. One major advantage of this cavity design is that it employs a relatively large hole-shift (10s of nm) in comparison to the heterostructure or line width modulated cavities that require nm-level precision. As a result, this design is less prone to fabrication errors. The experimental quality factor was around 5×10^5 with a theoretically predicted quality factor of around 3×10^6 and a mode volume of $1.8(\lambda_o/n)^3$. Welna et al. also demonstrated that their cavity is more tolerant to fabrication disorder compared

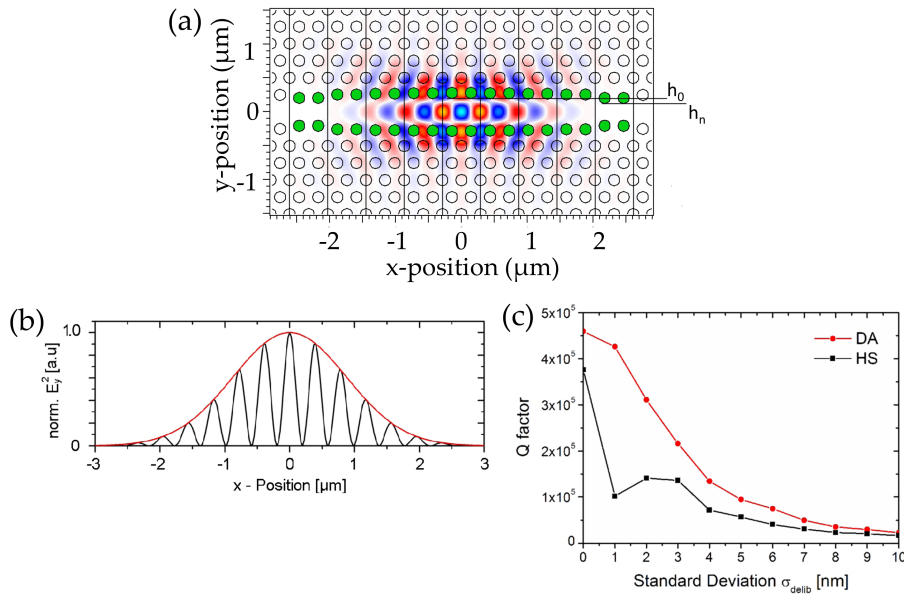


Figure 3.9 – Dispersion adapted (DA) cavity with confined first order mode (E_y field). The shifted holes are denoted by green circles. Hole-shifts starting from h_0 in the first section to h_n in the last section (in this case 5 sections are used). The waveguide continues as a W1 after the last section. (b) Intensity profile of the first order mode $y=0$ with a Gaussian envelope function (red) overlaid. (c) Measured quality factors as a function of the standard deviation of the deliberate hole-diameter disorder for dispersion adapted cavity and heterostructure cavities. (Reproduced with permission of the IEEE from [96], Copyright 2012)

to a heterstructure cavity (Fig. 3.9c). One major disadvantage of this cavity design is that it is not a single mode cavity and it contains number of cavity modes. Therefore, this type of cavity has a smaller FSR.

3.3.4 Oxide clad photonic crystal cavity

All the high quality factor cavity designs discussed above use the symmetric air-clad silicon membrane configuration. The use of air as the cladding material maximizes the index contrast to silicon thus maximizing the size of the photonic band gap and minimizing the coupling to radiation modes due to the strong total internal reflection. The mechanical and thermal instabilities of air-membrane structures have been major obstacles to their application and heterogeneous integration. Furthermore, when air-membrane structures are exposed to air, continuous oxidation and unavoidable contaminations can affect the characteristics of photonic devices [104]. A more robust alternative is to retain the silica substrate beneath the silicon, creating an asymmetric structure with air above. In addition to the improved mechanical stability, this silicon-on-insulator (SOI) geometry can be fabricated entirely using CMOS fabrication methods [105], and is thus more suited to monolithic integration with electronics than membrane structures. From an optical perspective, however, the performance of the photonic devices can

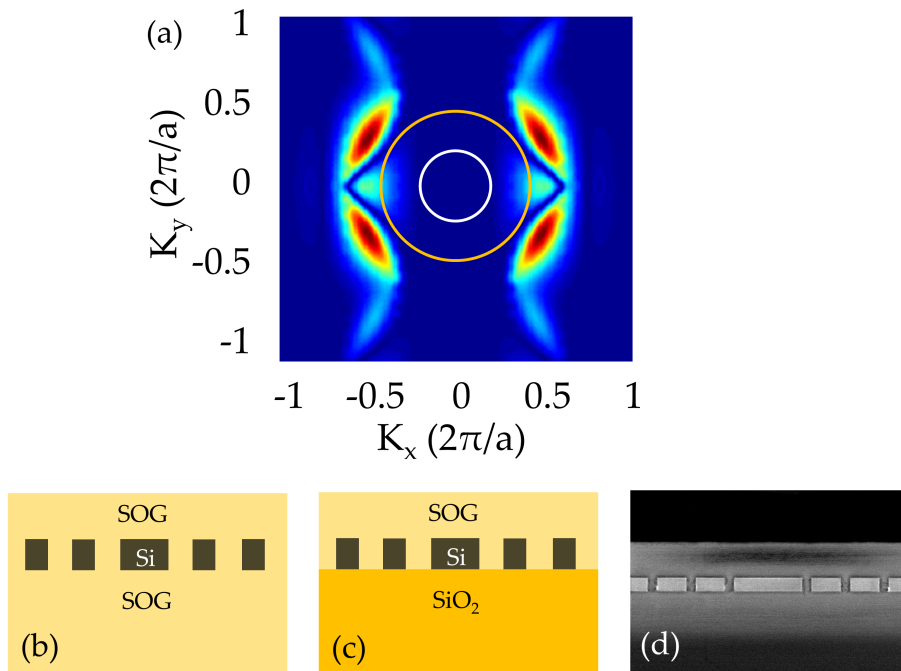


Figure 3.10 – (a) k-space distribution of the first order cavity mode of an L3 cavity. The white and yellow circles correspond to the boundaries of the leaky region corresponding to the air- and oxide-cladding respectively. (b) Cross-sectional schematic of a completely SOG-clad photonic crystal structure (c) Cross-sectional schematic of a partially SOG-clad photonic crystal structure (d) SEM image of the same structure as in (c).

degrade because of coupling between the transverse electric (TE) and transverse magnetic (TM) modes in asymmetric structures [106, 107]. To avoid such coupling loss between TE and TM modes, and at the same time to improve the mechanical stability of the photonic crystal devices, oxide-clad structures have been proposed [108, 109, 110].

In oxide-clad-structures, due to the reduction in index contrast between silicon and the cladding layer, more light couples to the radiation mode or the cladding mode from a photonic crystal cavity mode, resulting in a reduction in the quality factor of the cavity. This can be understood by considering the k-space distribution of a photonic crystal cavity. Fig. 3.10a shows the k-space distribution of an L3 cavity. The white and yellow circles correspond to the boundaries of the leaky region due to air cladding and oxide-cladding, respectively. It is apparent from the figure that the leaky region corresponding to oxide-cladding covers more intensity distribution than the air-cladding boundary. As discussed earlier, the lower the intensity in the leaky region in k-space, better the quality factor of the cavity. Therefore, the quality factor of a photonic crystal reduces when it is clad with oxide.

Photonic crystal structures can be oxide-clad either by partially covering the structure (where the bottom oxide layer of the SOI remains intact) or by fully covering the structure (where the bottom oxide layer is removed) using spin-on-glass (SOG) or depositing SiO_2 [65]. The partially clad structures are

easy to fabricate, due to the fact that they do not require additional etch steps to remove the bottom oxide layer, but they are inferior to fully clad structure due to their asymmetry [110]. Jeon et al. [109] carried out a study on the effect of oxide-cladding on the quality factors of different photonic crystal cavities. They experimentally demonstrated a quality factor of only $Q \approx 1000$ for an L3 cavity, which is rather low. Therefore, oxide clad L3 cavities are usually avoided. For oxide-clad heterostructure cavities, however, a quality factor as high as $Q \approx 1.6 \times 10^5$ was achieved. By further modification of the structure, Song et al. [110] demonstrated a further improvement to $Q \approx 1 \times 10^6$. As we will see later, both linewidth modulated cavity and dispersion adapted cavities also achieve quality factors in the order of 10^5 when oxide-clad. Although the oxide cladding reduces the quality factor, these numbers are well above the requirements for many applications, such as modulation and switching.

3.4 Coupled waveguide-resonator system

In this section, we will discuss the operation principle of a coupled waveguide-resonator system where the individual components are evanescently coupled to each other. There are two generic configurations for such a coupled waveguide-resonator system: side coupling and resonance coupling, as shown in Fig. 3.11a and 3.11b, respectively.

In the side-coupling configuration, when light is launched at one end of the waveguide and if the wavelength of the propagating wave matches with the resonance wavelength of the resonator, light couples evanescently from the waveguide mode to the resonator mode. Some of the coupled light gets lost due to radiation/scattering loss or due to absorption in the resonator, while the rest couples back to the waveguide mode contributing to the reflection and transmission in the waveguide. When the wavelength of the propagating mode does not match with the resonance wavelength of the resonator, no coupling between the waveguide mode and the resonator mode takes place and light simply propagates through the waveguide.

The resonance coupling configuration consists of two waveguides coupled to each other by a resonator. When the wavelength of the propagating wave in one of the waveguides matches with the resonance wavelength of the resonator, light couples from the input waveguide to the cavity and then from the resonator to the output waveguide. Non-resonant wavelengths will simply be reflected back. In this case, light only couples from the input waveguide to the output waveguide on resonance, hence called “resonant coupling”. Most of the time, in the resonance coupling configuration, all the components share a common symmetry axis, which is why this configuration is also referred to as the “in-line” coupling configuration.

Hence, by definition, a side-coupled system acts as a channel drop filter, while a resonance-coupled system acts as an add filter by only allowing a specific wavelength to pass. For WDM applications, side coupled systems are particularly interesting, as off-resonant wavelengths are transmitted allowing for the cascading of multiple devices. Transmitting multiple channels

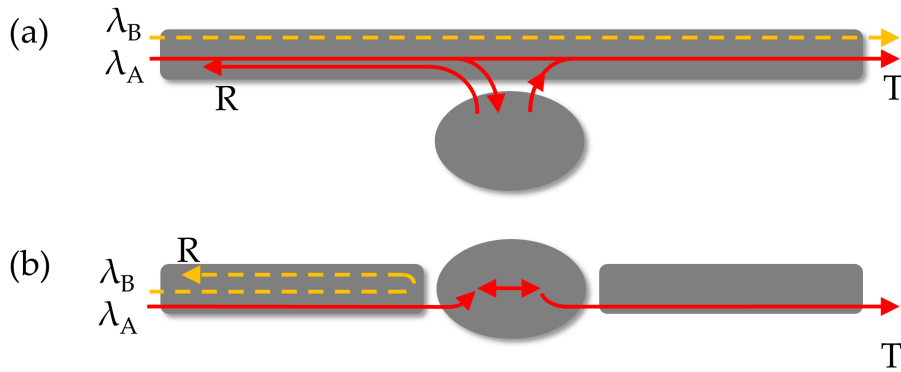


Figure 3.11 – (a) The side coupling case, where a resonator is side coupled to a waveguide. (b) The resonant coupling case, where two waveguides are coupled by a resonator.

through the same waveguide would require an additional multiplexer in case of in-line coupling. Therefore, in the following discussion we will consider only the side-coupled case.

3.4.1 Two-port analysis of a side coupled system

To formulate the transmission and reflection properties of a side coupled system, we will consider it as a two port system and use a temporal coupled wave analysis. A general assumption in coupled mode theory is that the overall system is described in terms of a set of a weakly coupled systems, each of which can be analyzed using general principles [100]. For example, a resonator can be considered as an oscillator in time. Here we make the further assumption that the system possesses a mirror-symmetry with respect to $x = 0$ plane. We also assume that the resonator and the waveguide only support single modes and that the dispersion of the waveguide is negligible in the frequency range of interest. These assumptions are valid for all the photonic crystal cavity designs studied in this thesis.

Here we express the amplitude of the field inside the resonator by a variable A . The amplitudes of the incoming (outgoing) waves in the waveguide are expressed as S_{+1} (S_{-1}) and S_{+2} (S_{-2}) respectively, which are normalized such that their squared values correspond to the incoming (or outgoing) power in the waveguide. For a standing wave cavity, the cavity mode will decay into forward and backward propagating waveguide modes over a finite interaction length, where the resonator mode physically overlaps with the waveguide fields. We consider that the region where the modes interact is fully contained within the input and output reference planes, defined on either side of the resonator, as shown in Fig. 3.12a. The intrinsic decay rate of the cavity mode is denoted by Γ_o and the decay rates into the forward and backward propagating wave are denoted by Γ_{c+} and Γ_{c-} , respectively. Using the mirror symmetry assumption, we can write $\Gamma_{c+} = \Gamma_{c-} = \Gamma_c/2$, where Γ_c is the total decay rate into the waveguide.

The time evolution of the cavity mode can be described by a set of tem-

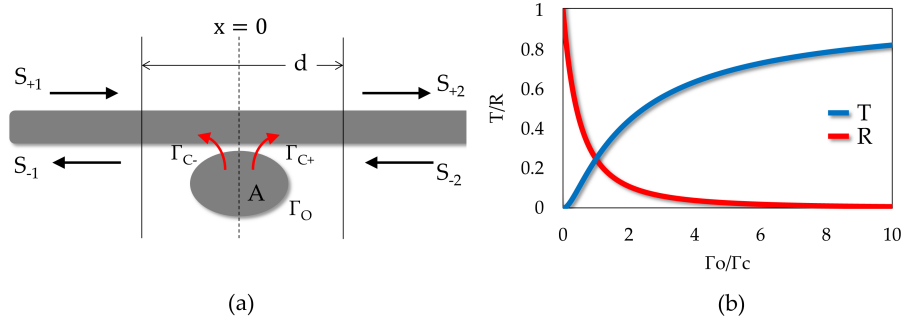


Figure 3.12 – (a) A single mode resonator is coupled to a single mode waveguide. The dashed line represents the mirror symmetry axis. The solid lines represent the input and output reference plane. (b) The reflection (red) and transmission (blue) coefficients at resonance wavelength as a function of Γ_o/Γ_c

poral coupled mode equations [111]

$$\frac{dA}{dt} = (j\omega_o - \Gamma_o - \Gamma_c)A + \sqrt{\Gamma_c}e^{j\theta}S_{+1} + \sqrt{\Gamma_c}e^{j\theta}S_{+2} \quad (3.5)$$

$$S_{-1} = e^{-j\beta d} \left(S_{+2} - e^{-j\theta} \sqrt{\Gamma_c} A \right) \quad (3.6)$$

$$S_{-2} = e^{-j\beta d} \left(S_{+1} - e^{-j\theta} \sqrt{\Gamma_c} A \right) \quad (3.7)$$

where ω_o is the resonance wavelength of the resonator and θ is the phase of the coupling coefficient from the incoming wave to the resonator mode. β is the propagation constant in the waveguide. Without the presence of the cavity, the incident light will appear at the output unperturbed, with a phase shift due to the finite distance d between the two reference planes.

If we now consider that light is launched into the waveguide from the left ($S_{-2} = 0$) and that S_{+1} has an $e^{j\omega t}$ time dependence, then at steady state, the cavity mode is

$$A = \frac{\sqrt{\Gamma_c}e^{j\theta}}{j(\omega - \omega_o) + \Gamma_o + \Gamma_c} S_{+1} \quad (3.8)$$

By substituting Eq. 3.8 into Eq. 3.6 and Eq. 4.7, we can express the reflection and transmission coefficients of the system as

$$R = \frac{|S_{-1}|^2}{|S_{+1}|^2} = \frac{\Gamma_c^2}{(\omega - \omega_o)^2 + (\Gamma_o + \Gamma_c)^2} \quad (3.9)$$

$$T = \frac{|S_{-2}|^2}{|S_{+1}|^2} = \frac{(\omega - \omega_o)^2 + \Gamma_o^2}{(\omega - \omega_o)^2 + (\Gamma_o + \Gamma_c)^2} \quad (3.10)$$

Figure 3.12b shows the reflection and transmission coefficients as functions of Γ_c/Γ_o on resonance ($\omega = \omega_o$). We can notice that when $\Gamma_c/\Gamma_o = 0$, the transmission coefficient T becomes zero, and the reflection coefficient is unity. On the other hand, when the intrinsic loss of the cavity is much

larger than the cavity-waveguide coupling (i.e. $\Gamma_c/\Gamma_o \gg 1$) the transmission coefficient approaches unity and the reflection coefficient almost vanishes.

Sometimes, it is more convenient to express the transmission and reflection coefficients in terms of quality factors, as they are readily available from the wavelength spectra. Therefore, for the following discussion the system performance will be analyzed in terms of quality factors rather than decay rates. The relationship between quality factor and decay rate is $\Gamma = \omega_o/2Q$. Using this we can express the transmission and reflection coefficients in terms of quality factors at resonance as

$$R = \frac{1/Q_c^2}{(1/Q_o + 1/Q_c)^2} = \frac{Q_t^2}{Q_c^2} \quad (3.11)$$

$$T = \frac{1/Q_o^2}{(1/Q_o + 1/Q_c)^2} = \frac{Q_t^2}{Q_o^2} \quad (3.12)$$

where Q_c is the quality factor associated with the waveguide-resonator coupling and Q_t is the overall quality factor of the system and expressed as

$$1/Q_t = 1/Q_o + 1/Q_c \quad (3.13)$$

It is clear from the above equations that in order to use this side coupling waveguide-resonator system as an ideal drop filter, one necessary condition has to be satisfied, i.e. $Q_o \gg Q_c, Q_t$. In other words, when a cavity with high quality factor is employed, the coupling efficiency between the waveguide mode and the cavity mode should increase without affecting the high quality factor of the cavity in order to increase the drop efficiency (i.e. extinction ratio) of the filter.

3.4.2 Limitations with conventional side coupling approach in photonic crystal

Despite their unique properties, photonic crystal cavities have not been exploited as extensively as ring resonators or micro-disc resonators. The primary reason behind this is that the traditional coupling schemes available to couple light in and out of the cavity are not efficient enough to provide high drop efficiency along with high overall quality factor required for optical filters. Conventionally, in photonic crystals the side coupling scheme is realized by incorporating both the cavity and the waveguide in the same photonic crystal lattice, a configuration we refer to as “in-plane configuration”. In general, for a side-coupled configuration, the drop efficiency can be improved by increasing the coupling efficiency between the waveguide mode and the cavity mode. For the in-plane configuration, an increase in coupling efficiency can be achieved by reducing the physical separation between the cavity and the waveguide, which in turn increases the overlap between the evanescent tails of the two modes. The presence of the line defect presented by the adjacent waveguide, however, perturbs the symmetry of the photonic crystal lattice which introduces additional k-components into the leaky region and reduces the intrinsic quality factor of the cavity. Hence, the drop efficiency of such

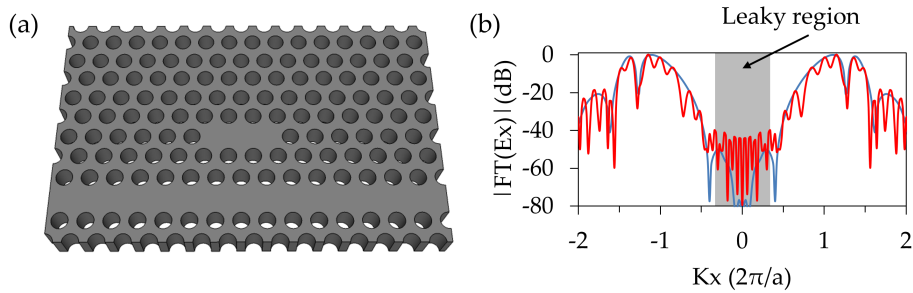


Figure 3.13 – (a) An L3 cavity coupled to a photonic crystal waveguide. (b) K-space distribution along $k_y=0$ before (blue) and after (red) the introduction of the waveguide. The gray region represents the leaky region.

filter cannot be improved because as we increase the coupling efficiency between waveguide and cavity this adversely affects the property of the cavity and violates the weak coupling approximation. This can be explained by an example. Figure 3.13a shows an L3 cavity with a line defect formed in a triangular lattice of air holes in a silicon slab with periodicity of $a = 420$ nm. The thickness of the slab and the radius of air holes are $0.52a$ and $0.28a$ respectively. Without the presence of the line defect the intrinsic quality factor of the cavity is 4982 with a resonance wavelength at 1557 nm. But when a line defect is introduced three rows away ($\sim 1.1 \mu\text{m}$) from the cavity, the resonance wavelength decreases by 10 nm and the intrinsic quality factor of the cavity drops to 2690 (calculated using Eq. 3.12). We should expect a similar trend as we bring the waveguide closer to the cavity. The reason behind this deterioration in the intrinsic quality factor of the cavity can be explained by examining the k-space distribution of the two structures. In Fig. 3.13b, the blue and red curves show the k-space distribution at $K_y=0$ for L3 cavity without and with the line defect respectively. It is evident that more k-space components appear inside the leaky region when the waveguide is introduced, which reduces the intrinsic quality factor of the cavity. This clearly demonstrates why in-plane coupling configuration is not suitable to realize optical filter with high drop efficiency. It is important to note here, that a similar effect can be expected in case of resonance coupling structure with both the waveguides and the cavity realized in the same photonic crystal lattice.

Moreover, the physical separation between the waveguide and the cavity is discrete and is decided by the periodicity of the photonic crystal. As a result, precise control of the coupling efficiency is difficult. The coupling waveguide, when realized in the photonic crystal geometry also tends to be more lossy than a comparable conventional waveguides, mainly due to the high index contrast which amplifies fabrication disorder.

3.5 Vertical coupling

Vertical coupling is an alternative side coupling scheme which avoids the problems associated with in-plane coupling, where the waveguide is placed

on top of the photonic crystal cavity, as shown in Fig. 3.14. In this configuration, the waveguide mode and the cavity mode are coupled vertically to each other and are separated by a low index buffer layer where their evanescent tails overlap. Unlike in-plane coupling scheme, here we can precisely control the separation between the waveguide and the cavity by controlling the thickness of the buffer layer. Furthermore, the cavity design and the optimum coupling condition to the waveguide can be optimized independently. Also, the incorporation of active components, such as pn junction, in the vertical coupling configuration is much easier in comparison to in-plane coupling. Finally in vertical coupling scheme, the waveguide can be placed much closer to the cavity in order to increase the coupling efficiency without severely affecting the symmetry of the photonic crystal cavity, thereby maintain weak coupling condition intact. Albeit placing a waveguide close to the photonic crystal cavity will break its symmetry; however, as we saw in Section 3.3, most of the 2D high Q photonic crystal cavity designs incorporate gentle confinement of light in the cavity mode by locally modifying the lattice structure in order to avoid any k-space field components inside the leaky region, whereas the vertical confinement is achieved simply by index guiding. Hence any in-plane perturbation will have more serious impact on the characteristic of the cavity than any vertical perturbation.

Previously, the vertical coupling configuration has been implemented via fiber tapers mainly for the characterization of photonic crystal cavities [112, 113]. A fiber-coupled photonic crystal cavity has also been used to realize active devices such as modulators [114]. Due to the large index mismatch between the fiber and the photonic crystal cavity, efficient coupling is often quite difficult between the two modes. Moreover, for any practical applications mechanical stability and monolithic integration is preferable. In [91], a different optical filter design was proposed where a silicon bus waveguide is vertically coupled to a silicon photonic crystal cavity. Here we develop insights into such optical filters, and show that very efficient transfer of light can be achieved, even between modes with dissimilar modal refractive indices, thus achieving an optical filter with a high extinction ratio. As a consequence, low refractive index waveguides with large mode areas may be used allowing very efficient interfacing with optical fibers. A similar approach was used previously in our group to couple light from a vertically placed polymer waveguide to a photonic crystal waveguide [115].

3.5.1 Condition for high coupling efficiency

From Eq. 3.11 and Eq. 3.12, it is clear that in order to increase the drop efficiency of a side coupled filter, Q_c should decrease whereas Q_o should remain unaltered, so that Q_c/Q_o becomes smaller. In other words we need to increase the coupling efficiency while maintaining a high quality factor of the cavity. The coupling efficiency depends mainly on two factors: (a) degree of the spatial overlap of the evanescent modes of the cavity and the waveguide and (b) degree of overlap of the k-space distributions of the two modes. The spatial overlap between the two modes can be optimized by controlling the thickness of the barrier layer. The k-space overlap is particularly interesting

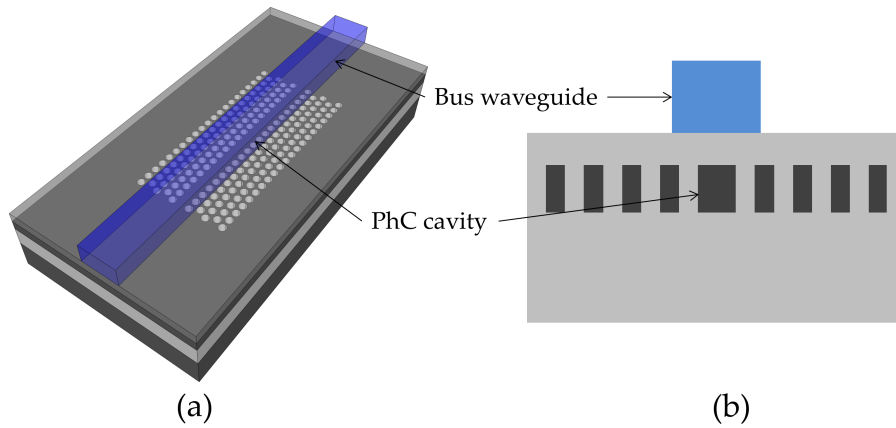


Figure 3.14 – (a) Schematic diagram of the optical filter, where a bus waveguide is vertically coupled to a photonic crystal cavity, b) Cross sectional view at the cavity region

in this case. In conventional coupled systems, e.g. directional couplers, to ensure k -vector matching between the two optical modes, similar materials are used to guide both the optical modes. But in case of photonic crystal cavities, the k -space distribution is expanded by their ultra-small mode volume. This helps to achieve nonzero k -space overlap with the optical mode of a waveguide even with dissimilar material. And due to this rich k -space distribution of the cavity mode, a small change in the effective index of the waveguide can cause a large change in the mode overlap and hence a large change in the transmittance of the whole system. Therefore, the coupling efficiency between the waveguide mode and the cavity mode can be controlled either by changing the physical properties of the waveguide, such as the dimensions or material, the lattice structure of the photonic crystal cavity or the thickness of the barrier layer. All of these parameters can be controlled with very high precision. Importantly, the coupling efficiency is not strongly controlled by features whose dimensions are critical in terms of lithography, such as the hole size, which is a significant advantage over other approaches.

The influence of effective index of the waveguide mode on the coupling efficiency and thereby the transmission property of the vertically coupled system, can be understood by analyzing the mode profiles of a photonic crystal cavity and a bus waveguide. Here we consider an L3 cavity in a silicon slab suspended in air. Figure 3.15 shows the calculated real space and Fourier space distribution of the dominant electric field (E_y) of the waveguide and the cavity. The white circle shows the boundary of the leaky region due to the air cladding. We notice that the intensity distribution of the waveguide mode expands along the k_y axis, which is due to the real space confinement in y -direction. Along k_x , however, the intensity distribution follows a sinc function and decays quickly. Note that the sinc type distribution is an artifact of the finite calculation domain that we have chosen. Any change in effective index of the waveguide, either by changing the dimension or the material, will move the high intensity regions in k -space along k_x . The k -space distribution

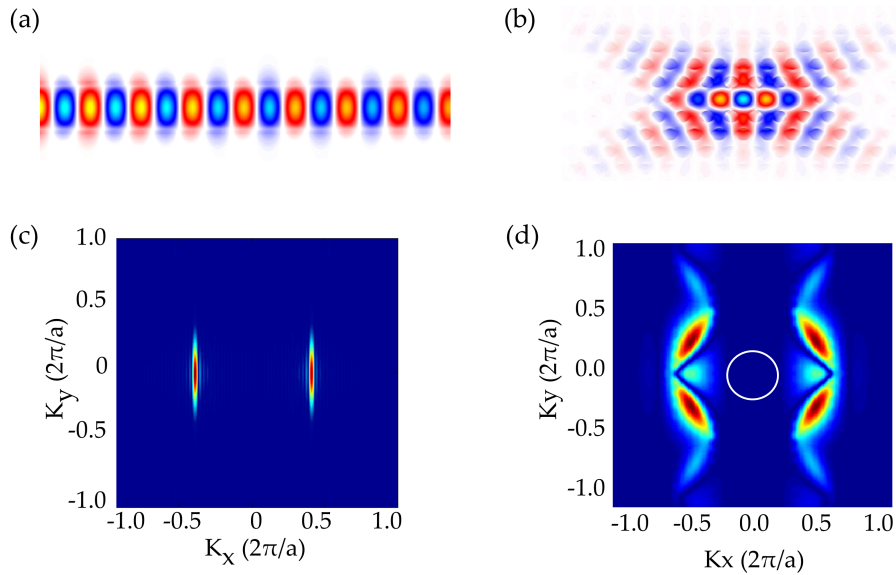


Figure 3.15 – Dominant electric field (E_y) profile of (a) the waveguide, (b) the photonic crystal cavity. K-space distribution of the dominant field (c) the waveguide, (d) the photonic crystal cavity.

of the cavity mode is more distributed and complex, which means that any small change in the effective index of the waveguide can cause a large change in the mode overlap and hence a large change in the transmittance of the entire system.

The photonic crystal cavity itself may be engineered so that the cavity mode exhibits a k-vector space suitable for matching to that of a specific waveguide. Figure 3.16 shows an example of this. By distorting the normal triangular photonic crystal lattice, the k-vector space can be made to develop higher intensities in the desired regions, resulting in improved coupling. A triangular lattice with an inter-hole spacing (spacing between the next neighboring holes) equal to the lattice period a is used as a starting point. The lattice is then distorted by stretching/squeezing it in y-direction (Fig. 3.16a) to fine-tune its k-space distribution. As a result, the vertical inter-hole spacing y changes from its original values $\sqrt{3}/2a$ to a higher or lower value depending on the value of the stretching/squeezing factor f . Figure 3.16b and 3.16c shows the real space and the k-space distribution of the cavity mode for different values of the stretching parameter f , respectively. We notice that the k-space intensity of the cavity mode at the waveguide high intensity regions (represented by the yellow ellipses) changes with f .

This Vertical coupling technique also allows coupling to different types of photonic crystal cavities for improved flexibility in the choice of parameters such as free spectral range and quality factor. It is also important to note that the coupling efficiency of a specific photonic crystal cavity can be tuned/adjusted without influencing the cavity design strongly.

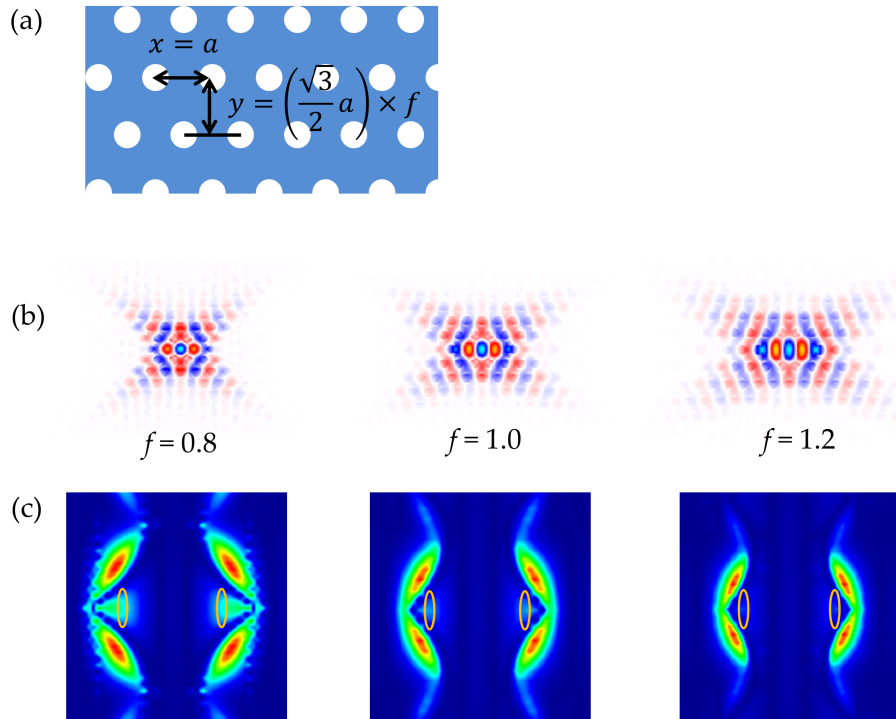


Figure 3.16 – (a) A standard triangular photonic crystal lattice with inter-hole spacing along the x-direction x and inter-hole spacing in y-direction y . (b) Real space field profile of a L3 cavity when the stretching/squeezing factor f is varied. (c) K-space distribution for different values of f . The yellow ellipses denotes the position of the high intensity regions of the waveguide mode.

3.5.2 Device fabrication

For experimental demonstration we consider partially SOG-cladded photonic crystal cavities. The advantage of using SOG-cladding is threefold, firstly, it helps to achieve an almost symmetric cavity mode ensuring a high Q-factor, secondly it offers mechanical stability and CMOS compatibility and finally the SOG-layer acts as the buffer layer between the waveguide and the cavity. Here we use two different high quality factor photonic crystal cavity designs: (a) linewidth modulated cavity and (b) dispersion adapted cavity (with 7 sections). Even with oxide-cladding, these designs offer significantly high quality factor. Table 3.1 summarizes the cavity parameters used for this demonstration. For the waveguide material, we consider ZEP 520A (a positive electron-beam resist) and silicon nitride (Si_3N_4). The ZEP 520A is used mainly to demonstrate low insertion loss of the system and high coupling efficiency between two very dissimilar material. Silicon nitride is used to demonstrate the effect of coupling efficiency on the overall response of the filter. In order to achieve efficient coupling of light into the waveguides in an end-fire setup, the width of the waveguides at the facets are kept at $3\ \mu\text{m}$ and tapered down to smaller width on top of the cavities.

The complete fabrication process is outlined in Fig. 3.17. It starts with a SOITEC Silicon-on-insulator wafer with 220 nm Silicon layer on a $2\ \mu\text{m}$

3. PHOTONIC CRYSTAL CAVITY BASED OPTICAL FILTER

Cavity type	Period	Radius	Line defect type	H0	H1	H2	H3	H4	H5	H6
DA	390	100	W1	40	36	29	22	13	-2	-25

Cavity type	Period	Radius	Line defect type	D _A	D _B	D _C
Line-width modulated cavity	390	100	W1	15	10	5

Table 3.1 – Design parameters for the photonic crystal cavities (all the numbers in nm)

thick buried oxide layer. A suitably sized piece of the SOI is first cleaned in acetone and IPA and then spin-coated with 350 nm thick electron beam resist ZEP 520A (Fig. 3.17a). Using electron beam (e-beam) lithography, the desired pattern is transferred into the resist. The resist is then developed in an e-beam resist developer, Xylene. Since ZEP 520A is a positive resist, the exposed area will be developed (Fig. 3.17b). After removing the exposed area, the pattern is transferred to the sample using reactive ion etching (RIE) (Fig. 3.17c). The sample is then cleaned with Piranha (3:1 H₂SO₄:H₂O₂) to remove any leftover resist and then spin-coated with a flowable oxide (FOx) containing hydrogen silsesquioxane (commercially available as FOx-14 from Dow Corning) which fills the PhC holes uniformly (Fig. 3.17d). The sample is first baked at 100°C to drive off all the solvents and then hard baked at 400°C for 4 hours. After this curing process, the resulting thickness of the FOx cladding is between 350 nm to 400 nm. The FOx layer is then further reduced using RIE. A thickness of 200 nm was used to achieve efficient coupling while keeping the overall quality factor of the filter high. The fabrication processes are slightly different for ZEP based waveguides and silicon nitride based waveguides. For ZEP waveguides, the sample is spin-coated with two layers of ZEP to produce a total thickness of 2 μm. The waveguide design is then transferred to the ZEP layer using e-beam lithography and is developed in Xylene. For silicon nitride waveguides, a layer of silicon nitride is first deposited on the surface using plasma-enhanced chemical vapour deposition (PECVD). This is done using a Plasma-Therm 790 Series system at the University of Sheffield, depositing the layer over a period of 45 minutes (Fig. 3.17e). Following deposition, the deposited layer is examined to verify its thickness and refractive index with an ellipsometer, where they are found to be 505 nm and 1.88 respectively. Waveguides were then patterned onto silicon nitride layer using e-beam lithography and RIE (Fig. 3.17f). Figure 3.18a shows the SEM image of the DA cavity and Fig. 3.18b shows a cross-sectional SEM image of the fabricated device with silicon

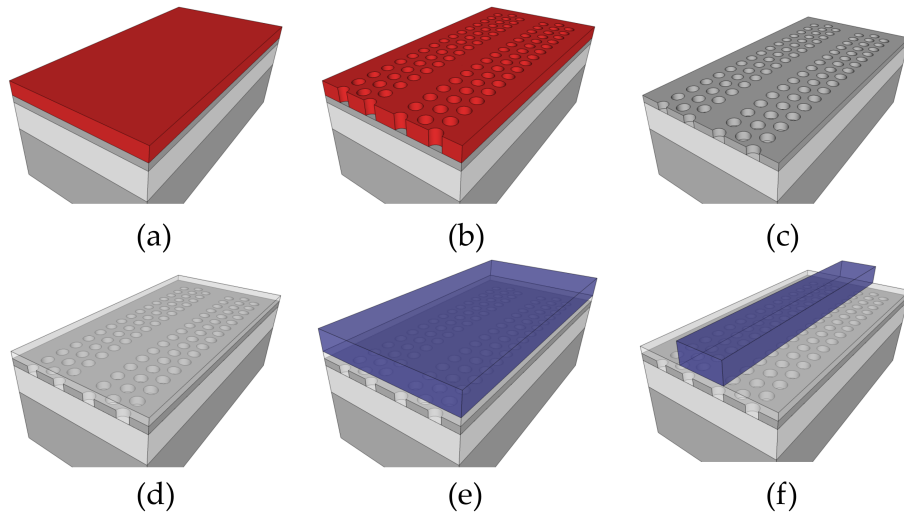


Figure 3.17 – Fabrication process: (a) A sample of SOI is cleaved from the wafer and covered in e-beam resist. (b) The resist is exposed with the photonic crystal pattern. (c) The pattern is transferred into the top silicon layer using a RIE etch and the remaining resist is removed. (d) The sample is covered in FOx and the FOx thickness is reduced to 200nm. (e) The sample is either spin coated with ZEP, or Si_3N_4 is deposited onto the sample. (f) ZEP/ Si_3N_4 waveguides are formed.

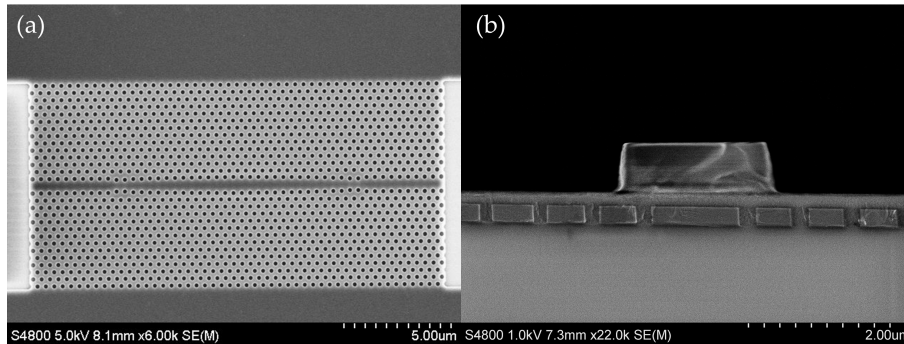


Figure 3.18 – SEM image of (a) Dispersion adapted cavity. Although most of the field intensity of the cavity mode is confined inside the cavity region, extra 10 lattice periods are added on each side of the cavity to avoid any small leakage of light into the bulk silicon or air mode. (b) Cross-section of the device in the cavity region.

nitride waveguide at the cavity region. After the final cleaning to remove any residual resist, the sample is cleaved to form optical facets.

3.5.3 Measurement setup

A schematic of the measurement setup is shown in Fig. 3.19. An end-fire technique is used to couple light in and out of the device. Light from a broadband (1520 nm to 1620 nm) amplified spontaneous emission (ASE) source is passed through a circulator and collimated using an objective lens

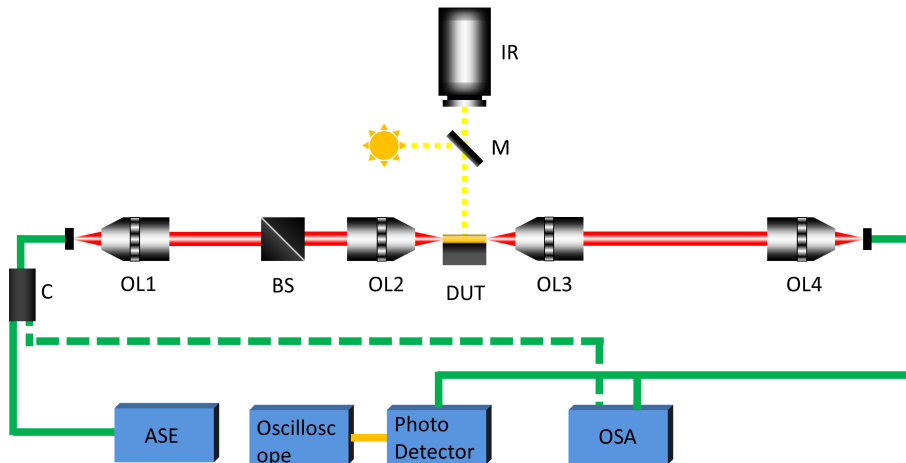


Figure 3.19 – Experimental setup for measuring transmission and reflection spectra. OL: Objective lens, BS: polarization beam splitter, DUT: device under test, C: circulator, M: mirror, IR: infrared camera.

(OL1). A polarization beam splitter is used to select only the TE polarized light and an objective lens (OL2) focuses the light onto one facet of the top waveguide. Another set of objective lenses (OL3 and OL4) collects the light from the other end of the waveguide. The collected light is then split into two parts, one part of which goes to an optical spectrum analyzer (OSA) and another part goes to a photo-detector which is connected to an oscilloscope. An infrared camera is used to achieve coarse alignment between the objective lenses and the waveguides on the sample. The fine alignment is carried out by maximizing the output voltage from the photo-detector. Once the alignment is done, the transmission measurement is carried out by taking the spectral scan using the OSA with a scanning resolution of 10 pm. The measured data is then stored using Labview. For measuring the reflection spectrum, one output from the circulator (as shown by the dashed line in Fig. 3.19) is connected to the OSA.

3.5.4 Transmission characterization

For most of the experimental demonstrations, a DA cavity is used because of its fabrication simplicity and higher disorder tolerance, resulting in a higher production yield in comparison to other high-Q cavity designs. Figure 3.20a shows the transmission spectrum of an optical filter consisting of a DA cavity and a ZEP waveguide with dimensions of $2\ \mu\text{m} \times 3\ \mu\text{m}$. As mentioned earlier, the DA cavity is a multimodal cavity; therefore we see a number of dips in the transmission spectrum corresponding to each cavity mode. For clarity, we only show the first two modes. The FSR of the overall filter is equal to the spectral separation between the modes, which is $\sim 7\ \text{nm}$. We also observe some background ripple ($\sim 0.3\ \text{dB}$) in the transmission spectrum, which originates from the reflections at both ends of the waveguide. In case of a ZEP waveguide, due to its lower index contrast to air, the amplitude of the ripple is lower.

In order to verify that the dips in transmission occur due to coupling between the waveguide mode and the cavity modes and not from the coupling to photonic crystal waveguide modes, infrared images of the scattered field are captured, as shown in the inset of Fig. 3.20a. The images clearly resemble the calculated intensity profiles of the cavity modes. In reality, there will be coupling between the dielectric waveguide mode and the photonic crystal waveguide mode, because the dispersion relations of the two modes intercept one another. In the wavelength range of the cavity mode, however, there is no guided mode supported by the photonic crystal waveguide, so no coupling takes place between the two waveguide modes.

Figure 3.20b shows the transmission and reflection spectra of the same device for the first order cavity mode. At resonance, only 20 % of the incident light is transmitted through the system and almost 80 % is reflected back. This type of response is expected from any high-Q cavity on pure crystalline silicon, where the loss due to scattering and absorption is minimal. In this case, the extinction ratio, which is calculated as the ratio between the on and off transmitted power, is 7 dB. At such high extinction ratio, the overall quality factor is maintained at 50,000. Using Eq. 3.11 and Eq. 3.12, we can estimate the quality factor associated with coupling and intrinsic quality factor as $Q_c \approx 60,000$, and $Q_o \approx 110,000$ respectively.

The primary reason behind using the ZEP waveguide is to demonstrate the low coupling loss of the filter while achieving reasonably high extinction ratio. In order to measure the loss arising from the interface, light from a tunable laser source is fed into the top waveguide using a lensed fiber. The TE polarization is maintained using a fiber polarization controller. At the output, light is collected using another lensed fiber and measured using a photo-detector. The measured overall loss (fiber-to-fiber loss) is found to be less than 3 dB. For silicon nitride waveguide the overall loss is ~6 dB. Here it is important to note that using techniques such as that employed in [54, 116], sub-dB insertion losses are possible with this approach.

To demonstrate operation with higher FSR, a line width modulated cavity is used. This kind of design generally produces a cavity with a higher quality factor in comparison to DA cavity. Because of its high quality factor, the high intensity regions in the k-space distribution of line width modulated cavity lies farther away from the light line (leaky region) of the FOx cladding. As a result, k-space overlap between the cavity mode and the waveguide mode is not significant for ZEP ($n=1.52$) based waveguides and hence the extinction ratio is poor for such filters. On the other hand, with silicon nitride based waveguides, we can achieve considerable amount of mode overlap due to large refractive index of silicon nitride ($n=1.88$). Figure 3.20c shows the transmission spectrum of an optical filter consisting of a line width modulated cavity and a silicon nitride waveguide. Because of the single mode nature of the cavity, the transmission spectrum only has a single dip at the resonance wavelength of the cavity. This demonstrates an FSR of at least 50 nm. This wavelength range can be further increased considering that this type of cavity shows single mode operation over a wavelength range more than 100 nm [73, 74]. The amplitude of the background ripple in the trans-

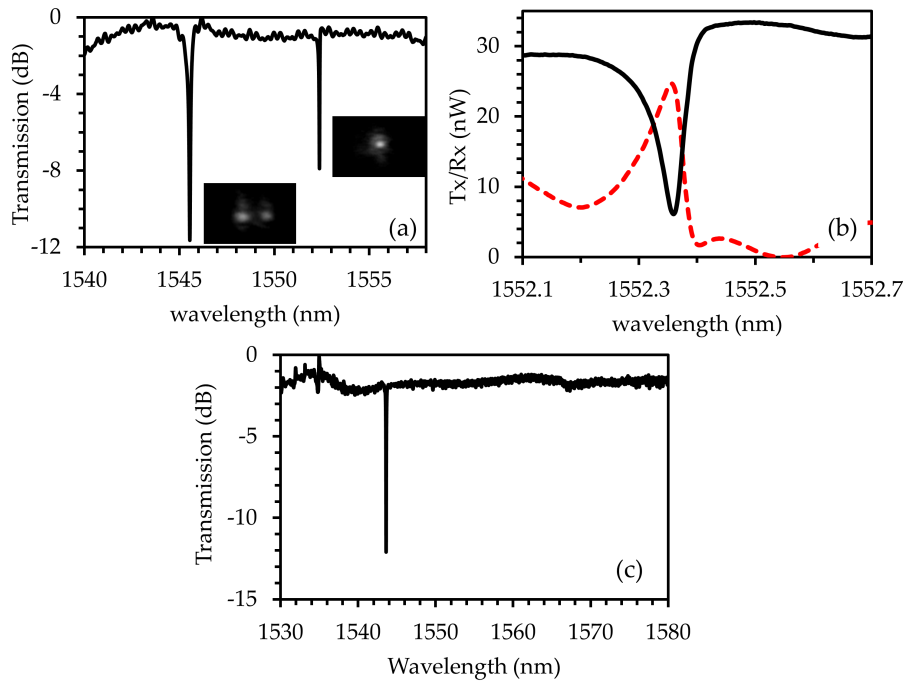


Figure 3.20 – (a) Normalized transmission spectrum of the optical filter comprising a DA cavity and a ZEP waveguide. The two dips in the transmission spectrum correspond to the first two modes of the cavity. The inset shows the infrared images of the intensity distribution of the two modes. (b) Transmission and reflection spectra of the same system around the first cavity mode. (c) Normalized transmission spectrum of the optical filter comprising a linewidth modulated cavity and a Si_3N_4 waveguide.

mission spectrum is ~ 1.5 dB. This is due to the increase in reflection from the facets because of the increase in index contrast. The extinction ratio of the filter is 10 dB with an overall quality factor of 38,000. This gives an intrinsic quality factor of $\sim 120,000$.

3.5.5 Effect of k-space overlap on extinction ratio

To demonstrate the effect of k-space overlap on the coupling efficiency and thereby the overall extinction ratio of the filter, first the width of the dielectric waveguides is varied. This change in physical dimension varies the effective index of the waveguide and thereby moves the k-space components of the waveguide mode along k_x ; as a result, the overlap intensity with the cavity mode also changes. In this experiment, silicon nitride is used as the waveguide material. Because of its relatively large refractive index, a wide range in the k-space can be covered to include some features of the cavity mode. The width of the silicon nitride waveguides is varied from $0.8 \mu\text{m}$ to $1.5 \mu\text{m}$. In most of this range, the waveguides support a single quasi-TE mode. However, the higher order mode that occurs for widths more than $1.2 \mu\text{m}$, accounts for very little energy compared with the fundamental mode and does not have a k-space overlap with the cavity modes. For these rea-

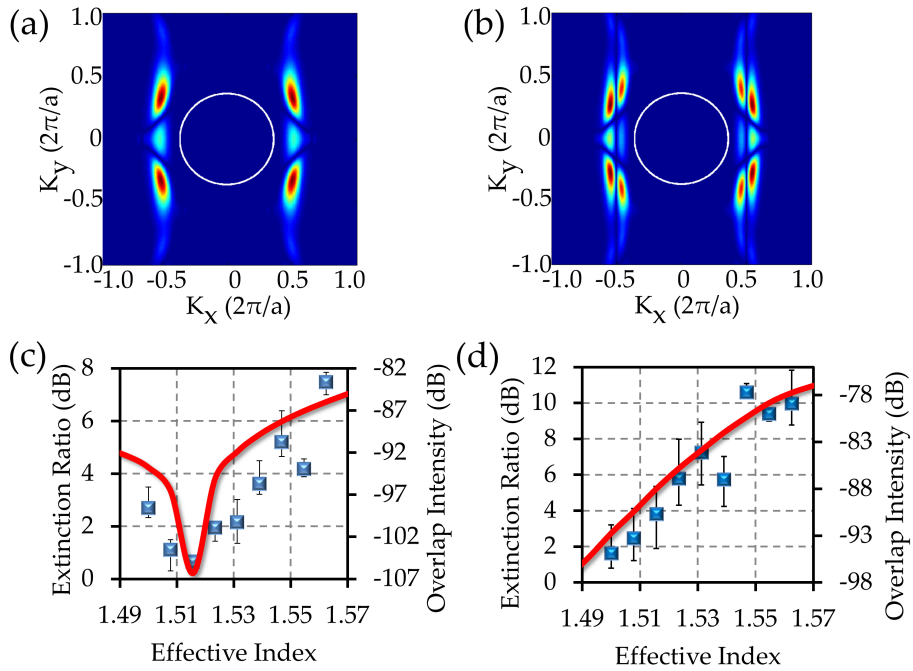


Figure 3.21 – K-space distribution of the dominant electric field (E_y) of (a) mode1, (b) mode2. Extinction ratio (blue squares) and k-space overlap intensity (red line) for different waveguide dimensions for (c) mode1, (d) mode2.

sons, only the fundamental mode is taken into account here. The cavity design chosen here is the same DA cavity as that used in the previous section. Only the first two resonance modes are considered here, and both of them have a reasonably high intrinsic quality factor.

Figure 3.21a and 3.21b shows the k-space distribution of the first two modes of the cavity, where the white circles denote the boundary of the leaky region (light line of FOx cladding). In Fig. 3.21c and 3.21d, the red curves are the calculated k-space overlap intensities as the effective index of the waveguide is modified and the blue squares show the corresponding measured extinction ratios. Comparing the theoretical overlap intensities with experimental extinction ratios, we note that both shapes match quite well. One might argue that the change in extinction ratio is caused by the change in the physical mode overlap and not the k-space overlap. This can be understood intuitively. For a monotonous increase in physical mode overlap, we should also expect a monotonous increase in the extinction ratio. But in case of the first order mode, when the k-space intensity drops at around an effective index of 1.51, the extinction ratio also drops. This suggests that the change in extinction ratio is mainly determined by the mode overlap in k-space rather than in real space.

As we discussed in Section 3.4.1, to achieve high extinction ratio (Eq. 3.11 and Eq. 3.12) in an optical filter, we should be able to increase the coupling efficiency without changing the intrinsic quality factor of the cavity, so that Q_c/Q_o approaches zero. We also claimed that in the vertical

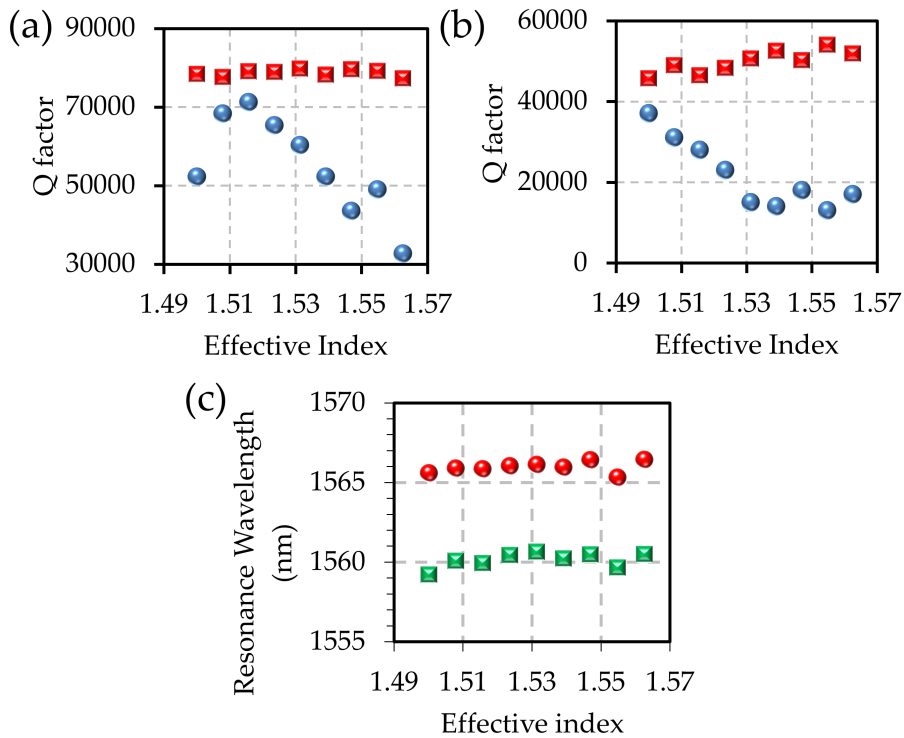
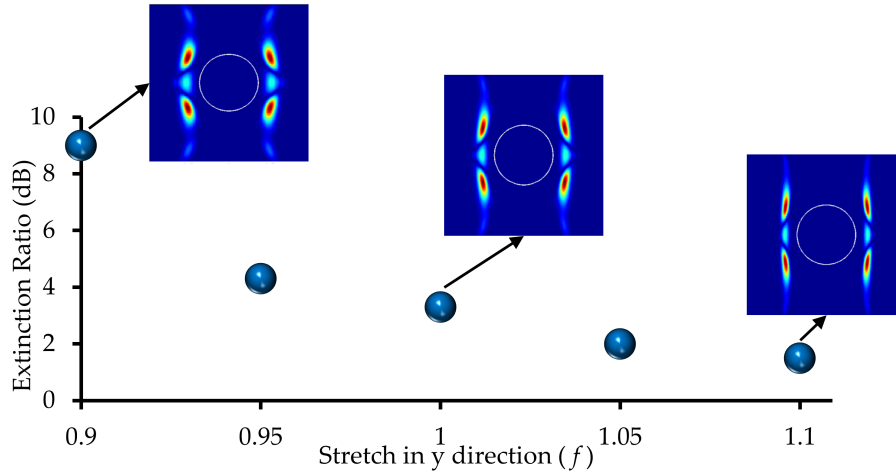


Figure 3.22 – Overall quality factor (Blue circles) and intrinsic quality factor (Red squares) for different waveguide dimensions for (a) model1, (b) mode2. (c) Resonance wavelength of the optical filter for different waveguide effective index.

coupling approach, we can independently optimize the coupling efficiency without changing the property of the cavity significantly. To validate this claim, in Fig. 3.22a and 3.22b, the overall quality factor of the filter and the calculated intrinsic quality factor of the cavity are plotted for different effective indices of the waveguide. As we expect, the total quality factor changes as the k-space mode overlap and the extinction ratio change. Interestingly, however, the intrinsic quality factor remains almost unchanged for both cavity modes. Also, in Fig. 3.22c, we can see that the resonance wavelength of the overall system (which is determined primarily by the cavity) remains within a wavelength range of 1.5 nm. These results clearly suggest that vertical coupling approach offers more flexibility in increasing the extinction ratio by improving the coupling efficiency.

Finally we study the dependence of the k-space occupied by the cavity mode on the overall extinction ratio. Here, the dimension of the waveguide is kept constant at $500 \text{ nm} \times 1.5 \mu\text{m}$ for all devices, but the basic hexagonal lattice of a DA cavity is stretched along the y-direction, so that the periodicity along y is $a_y = \left(\sqrt{3}/2a_x\right) \times f$, where a is the periodicity along x axis. By stretching the lattice we can vary the coupling coefficient as discussed in Section 3.5.1. Such distortion in the lattice also causes a shift in the resonance wavelength of the cavity, which we compensated by fine-tuning the cavity

Stretch in y direction (f)	0.90	0.95	1.00	1.05	1.10
a_x	400	395	390	385	375
a_y	312	325	338	350	357

Table 3.2 – Design parameters for Y-stretched cavities**Figure 3.23** – Measured extinction ratio of the optical filter comprising of a DA cavity and Si_3N_4 waveguide as a function of stretch factor f . Inset shows the k-space distribution for different values of f .

design. Table 3.2 summarizes the parameters used for this experiment.

Figure 3.23 shows the measured extinction ratios against the stretch factor f . As the value of f decreases from 1, the extinction ratio increases and when f increases the extinction ratio decreases. This can be explained by considering the k-space distribution of the cavity for different values of f . When f is smaller than 1, the high intensity region of the k-space is more expanded, and it will have a larger overlap with the waveguide mode. When f is larger than 1, however, the high intensity region is more compressed and the overlap intensity is small.

3.5.6 Multiplexing

One of the major advantages of the vertical coupling geometry is the possibility to multiplex several wavelengths channels in the same waveguide without requiring any additional multiplexer. This, as it has been mentioned earlier, is a drawback of in-line coupling. To demonstrate the multiplexing operation of the vertical coupling configuration, here we use five DA cavities (as shown in Fig. 3.24a) coupled to a single silicon nitride waveguide. The cavities share the same photonic crystal lattice and are separated by 20 lattice periods to avoid unwanted coupling between the cavities themselves. The different channel wavelengths can be achieved in many different ways, either by altering the parameters of the photonic crystal lattice or by fine tuning

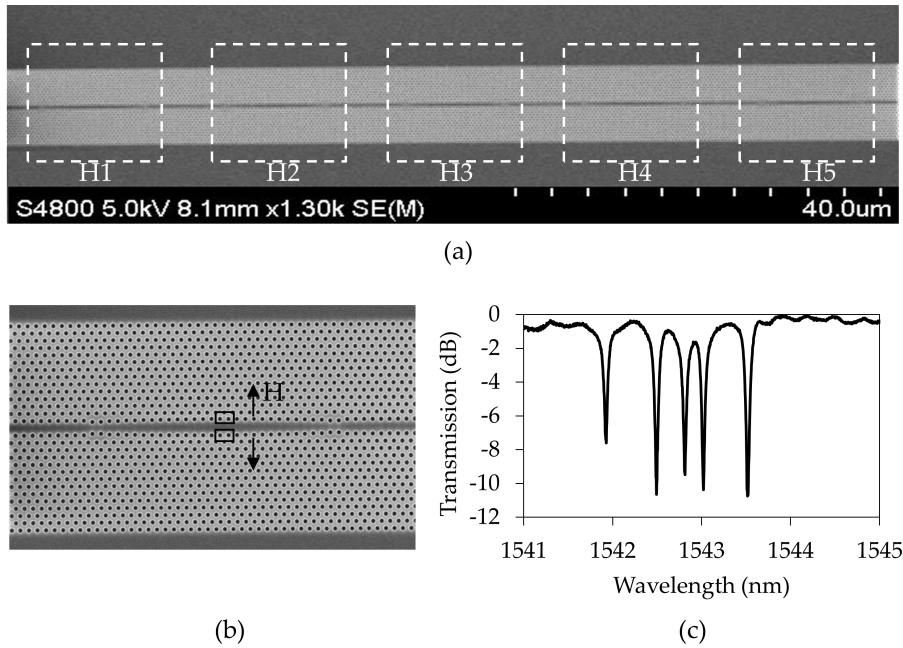


Figure 3.24 – (a) Five DA cavities in a single photonic crystal lattice. (b) The resonance wavelengths of each cavity are varied by tuning the position of the four innermost holes. (c) Normalized transmission spectrum at the Si_3N_4 waveguide output. Five dips in transmission correspond to the modes of the five cavities.

just the cavity parameters. Here we achieve the required resonance wavelengths of each cavity by tuning the positions of the four inner most holes, as shown in Fig. 3.24b.

Figure 3.24c shows the transmission spectrum at the output of the silicon nitride waveguide. A 2nm shift in the positions of the four holes is sufficient to move the resonance wavelength by ~ 0.5 nm. Due to fabrication variation, the five channels are not quite equally spaced [117]; we note that these channel spacing values can be further improved by trimming techniques such as laser assisted local oxidation [118], or by using highly efficient active tuning with integrated heaters [119]. We also notice that the extinction ratios for all five channels are not equal. The variation is caused by the slightly different k-space matching between the waveguide mode and the cavity modes. Careful control of the cavity and waveguide design can avoid such discrepancies.

3.6 Discussion

Photonic crystal cavities possess some unique characteristics; however, until now, they have not been exploited extensively as an alternative solution in photonic circuits. The reason lies in their implementation in real devices. Many clever designs have been proposed to increase the quality factor while maintaining wavelength scale mode volume of isolated photonic crystal cavities, but coupling light in and out of the cavity has remained as a ma-

major stumbling block. In traditional optical filter designs based on photonic crystal cavities, the inclusion of the waveguide in the same photonic crystal lattice affects the properties of the cavity and consequently deteriorates the performance of the overall system. The key advantage of the proposed vertically coupled system is that it physically separates the waveguide from the photonic crystal cavity and as a result they become less interdependent and the key parameters can be independently optimized. Separating the waveguide from the photonic crystal lattice also avoids the need for using the same material for both components.

At the beginning of this chapter I have highlighted some of the key features of waveguide-resonator systems, which are essential for their use in integrated photonic circuits, especially for on-chip optical networks. Based on the experimental results presented here, I believe that, the proposed vertically coupled system fulfills all the requirements and hence has the potential to become an ideal building block for such networks. This chapter mainly focused on the passive optical behavior of this vertically coupled system. In chapter 4 and chapter 5, I will demonstrate their use as active optical components, such as electro-optic modulators and photo-detectors.

Chapter 4

Cascaded Modulator Architecture

4.1 Introduction

Electro-optic modulation is one of the the most essential functionalities of an optical interconnect and in silicon photonics, a significant amount of research has been undertaken to develop efficient modulators. For an on-chip optical interlink, high integration density, simple design architecture, low energy consumption and low optical loss are the prerequisites, whereas for off-chip communication, such as chip-to-chip or rack-to-rack communication, a high data rate with a large extinction ratio is essential. There are primarily two modulation techniques employed in pure crystalline silicon: two-beam interference based modulation, typically Mach-Zehnder type modulators [56, 60] and resonance based modulation, typically ring resonators [67, 120]. In interference based techniques, optical modulation is achieved by changing the refractive index of the material and thereby changing the phase of the propagating wave, which is then converted into a change in optical intensity via an interferometer. Interference based modulation usually offers broadband modulation, high speed operation and better thermal stability. However, devices have relatively large footprint and as a result they are inappropriate for on-chip integration. Due to their large size, the energy consumption is also very high (in pJ/bit). Resonance based modulators operate on changes in the refractive index of the material, which modify the resonance wavelength of the device, which in turn modulates the output optical intensity of the device. Due to their small footprint and large quality factor, the operating energy is significantly smaller than for interference based modulators. Besides, their small size also promises chip-scale integration. The main disadvantage of resonance-based modulators, however, is their narrow bandwidth, which may limit the modulation speed and make them sensitive to changes in environmental conditions, most notably the operating temperature.

In any optical interlink, whether for on-chip or off-chip communication, in order to reach the required data transfer rate, wavelength division multiplexing (WDM) is essential for increasing the aggregate bandwidth. Two major approaches may be identified in the literature based on ring resonators

[81] and broadband modulators with arrayed waveguide gratings [35, 121]. WDM systems that employ resonance based devices generally achieve multi-channel operation by cascading multiple resonators. The small free spectral range (FSR) of ring resonators restricts the channel scalability of such WDM systems, however. WDM systems that employ broadband modulators use arrayed waveguide gratings (AWG) to multiplex multiple channels. Despite the broadband nature of the modulator, the overall operating wavelength window is then restricted by the 3 dB bandwidth of the AWG. In addition, both these approaches incorporate all silicon based components, and due to the large number of optical interfaces, the overall optical loss of the device is large and increases with increasing number of channels. Moreover, having all the optical components on the same platform makes it difficult to optimize the integration of both electronics and photonics, which is a primary requirement for on-chip interconnects.

In this chapter, I present a cascaded modulator architecture based on the vertically coupled system, which is the transmission section of the proposed architecture. The attraction of photonic crystal based cavities for electro-optic modulation is their ability to achieve both a high quality factor and a small mode volume at the same time. Due to their ultra-low mode volume, photonic crystal cavities can be modulated with a power consumption of one to two orders of magnitude lower than conventional ring resonators [72, 114, 122]. Along with this low power operation, photonic crystal cavities can also eliminate the restriction on channel scalability, since they can achieve a large free spectral range (>100 nm) [73, 74]. There have been some demonstrations of electro-optic modulation using photonic crystal cavities prior to this work. For example, Tanabe et al. demonstrated a modulator with ultra-low capacitance (5.6×10^{-18} F) based on resonance coupled photonic crystal cavity [72]. Shambat et al. used a tapered optical fiber to couple light in and out of a modulator based on photonic crystal cavity in GaAs[114]. They also demonstrated low power operation (0.2 fJ/bit), however, the use of a fiber for in-coupling directly makes it difficult to achieve a large extinction ratio and practical application. By using a monolithically integrated vertically coupled low index contrast waveguide, we can overcome the limitations associated with existing modulation and multiplexing techniques. Also, having a waveguide integrated on top of the cavity modulators promises better design optimization for the optoelectronic integration in case of on-chip interconnects and incurs low optical loss.

4.2 Wavelength tuning in photonic crystal cavities

As described in Chapter 3, the operating wavelength of the vertically coupled system is decided by the resonance wavelength of the cavity. If the wavelength of the incident light matches with the resonance wavelength (λ_o) of the cavity, light couples from the waveguide mode to the cavity mode. Some of the coupled light is lost due to scattering/absorption inside the cavity and the rest couples back into forward and backward propagating modes of

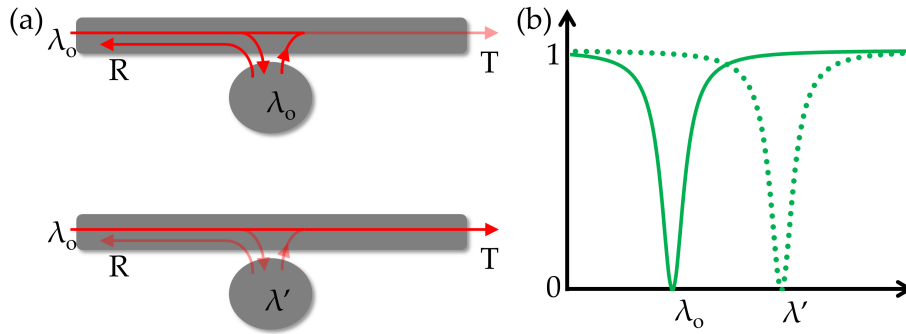


Figure 4.1 – (a) A schematic representation of Off-state (no transmission) and On-state (complete transmission) in a resonance based modulator. (b) Transmission spectra of the filter when the refractive index is unperturbed (solid) and perturbed (dotted).

the waveguide. The reflected light arising due to coupling to the backward propagating mode needs to be managed, which may otherwise cause instability in the light source. When the cavity resonance is shifted to a different wavelength (λ'), which no longer matches with the incident wavelength, no coupling happens and the light is fully transmitted. Therefore, by tuning the resonance wavelength of the cavity, a strong modulation in the output optical intensity can be achieved. This process is described schematically in Fig. 4.1a. The resonance can be tuned optically, electrically or thermally. In all cases, a perturbation in the refractive index of the cavity material is introduced, which either causes a redshift (in case of increase in refractive index) or a blueshift (in case of decrease in refractive index) in the cavity resonance. Figure 4.1b, shows an idealized transmission spectrum of the waveguide resonator system with and without an applied perturbation. For a perturbation of sufficiently small magnitude, the amount of redshift or blueshift is proportional to the change in refractive index:

$$\frac{\Delta\lambda}{\lambda_o} = \frac{\Delta n}{n} \quad (4.1)$$

where n is the average refractive index experienced by the optical mode and λ_o is the resonance wavelength of the cavity. $\Delta\lambda$ is the change in resonance wavelength due to a refractive index change of Δn .

The most effective way of achieving modulation in refractive index in bulk medium is by applying an electric field, because this implies little or no current flow (thus low power operation) and fast response time. The effect of an applied electric field to a material can cause either a change in the real part of the refractive index, which is called electro-refraction, or a change in the imaginary part of the refractive index, which is called electro-absorption. The best known ways of implementing modulation via electric field are the Pockels effect, the Kerr effect and the Franz-Keldysh effect. The Pockels effect, also known as the linear electro-optic effect, causes a change in the refractive index in a material that is proportional to the applied electric field. The Pockels effect is usually very strong in birefringent materials, such as

lithium niobate (LiNbO₃). In silicon, however, due to its centro-symmetric crystal structure, the Pockels effect is absent. The Kerr effect, on the other hand, is a third order nonlinear electro-optic effect, where the change in the real part of the refractive index is proportional to the square of the applied electric field. In silicon, the Kerr effect is present but very weak. For example, the applied electric field required to produce a refractive index change of 10^{-4} in silicon is 10^6 V/cm, which is above the breakdown field of lightly doped silicon [123]. Unlike the Pockels effect and Kerr effect, Franz-Keldysh effect causes electro-refraction by changing the imaginary part of the refractive index. This effect arises from the distortion of the energy bands in semiconductors upon the application of electric field. Similar to the Kerr effect, the Franz-Keldysh effect in silicon is also very weak [19].

Another way of achieving refractive index modulation in semiconductors is the free carrier plasma dispersion effect. This effect arises from the change in absorption caused by the change in free carrier concentration. The change in absorption alters the imaginary part of the refractive index of the material and, as a result, it affects the real part of the refractive index, according to the Kramers-Kronig relationship. Using experimental optical absorption spectra of silicon over a large range of acceptor and donor concentration (10^{17} to $10^{20}/\text{cm}^3$) and conducting a numerical Kramer-Kronig analysis, Soref and Bennet showed that the free carrier plasma dispersion effect produces a refractive index change two orders of magnitude higher than the Kerr effect and the Frenz-Keldysh effect in silicon and proposed that this effect can be promising to realize silicon based electro-optic modulators [123]. They also gave an empirical expression relating the change in refractive index and absorption coefficient to the change in carrier concentration at both $1.3 \mu\text{m}$ and $1.55 \mu\text{m}$ wavelengths, which are now universally used for evaluating optical modulation in silicon.

At $\lambda=1.3 \mu\text{m}$, these expressions are:

$$\Delta n = \Delta n_e + \Delta n_h = -6.2 \times 10^{-22} \Delta N_e - 6.2 \times 10^{-18} (\Delta N_h)^{0.8} \quad (4.2)$$

$$\Delta \alpha = \Delta \alpha_e + \Delta \alpha_h = 6.0 \times 10^{-18} \Delta N_e + 4.0 \times 10^{-18} \Delta N_h \quad (4.3)$$

And at $\lambda=1.55 \mu\text{m}$, these expressions are:

$$\Delta n = \Delta n_e + \Delta n_h = -8.8 \times 10^{-22} \Delta N_e - 8.5 \times 10^{-18} (\Delta N_h)^{0.8} \quad (4.4)$$

$$\Delta \alpha = \Delta \alpha_e + \Delta \alpha_h = 8.5 \times 10^{-18} \Delta N_e + 6.0 \times 10^{-18} \Delta N_h \quad (4.5)$$

Where, ΔN_e and ΔN_h are the change in free electron and hole concentrations. Δn_e and Δn_h are the change in refractive index resulting from the change in free electron and hole concentrations respectively. And $\Delta \alpha_e$ and $\Delta \alpha_h$ are the change in absorption coefficient resulting from the change in free electron and hole concentrations respectively. According to the above equations, at wavelength around $1.55 \mu\text{m}$, a change in carrier concentration of

$\Delta N = 6.7 \times 10^{15} \text{ cm}^{-3}$ causes a refractive index change of $\Delta n = -4.48 \times 10^{-5}$. As we will see later, this amount of change in refractive index is enough to produce sufficient modulation in the output intensity of our device.

Conventionally, the free carrier plasma effect is employed in silicon by adding pn or pin junctions into the device. For an applied voltage, either excess carriers are depleted (in reverse bias condition) from the junction or injected into the junction (in forward bias condition), which causes an increase or decrease in the refractive index of the silicon in the junction. Thus silicon based optical modulators are classified into two groups: depletion type modulators and injection type modulators. The modulation speed of depletion-type modulators is mainly decided by the RC time constant of the pn junction and can be very high [60, 62, 124, 125], whereas the speed of an injection type modulator is limited (few GHz) by the free carrier lifetime in the intrinsic region of the pin diode [72, 81].

Optical modulation in silicon can also be achieved by the thermo-optic effect, where the refractive index of the material changes with temperature. The thermo-optic coefficient of silicon is $dn/dt = 1.86 \times 10^{-4}/\text{K}$ [126]. That signifies that a change in temperature of 6°C can result in a refractive index change of 10^{-3} . Thermo-optic modulation is inherently a slow process and hence cannot give a modulation speed more than 1 MHz. Due to its slow response, the thermo-optic effect is not typically used for high speed modulation in silicon, but instead for thermal tuning.

4.3 Design and fabrication

4.3.1 Design consideration

A five channel WDM system is designed by cascading five modulators based on photonic crystal cavities vertically coupled to a single silicon nitride waveguide. The schematic of one of the modulators is shown in Fig. 4.2a, where the photonic crystal cavity is embedded into a pin junction and a silicon nitride waveguide is placed vertically on the top of the cavity and separated by a thin oxide layer. The cavity design considered here is a dispersion adapted cavity [96]. Although the dispersion adapted cavity does not offer a high FSR, I am using it here because of its large fabrication tolerance and better mode overlap with the polymer and silicon nitride bus waveguides. The five cavity designs considered here are identical, except for the positions of the four holes at the center of the cavity which are tuned to achieve five different resonance wavelengths. The dimension of the silicon nitride waveguide is $1.5 \mu\text{m}$ wide and 500 nm high. This width is chosen to increase the coupling efficiency between the waveguide mode and the cavity via a large k-space overlap, while the waveguide still operates in a single mode. To maintain a good physical overlap between the two modes, the oxide layer thickness is set to 200 nm. The gap between the p^+ and n^+ type regions is chosen to be $2 \mu\text{m}$ and the width of both the regions is $5 \mu\text{m}$ and the center of the cavity coincides with the center of the intrinsic region. Here, we are mainly interested in the first two modes of the DA cavity, be-

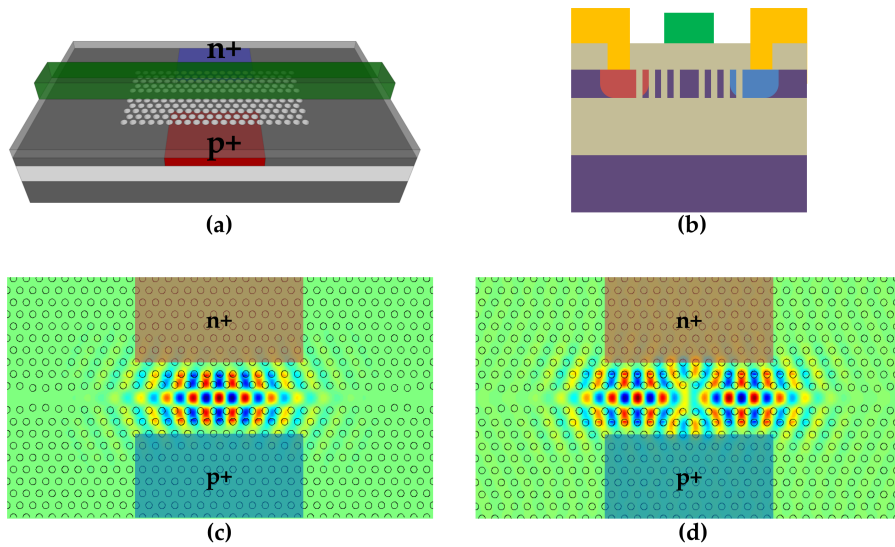


Figure 4.2 – (a) Schematic of the device. The photonic crystal cavity and the Si₃N₄ waveguide are vertically coupled through an oxide layer. (b) Cross section of the device, consisting of a pin diode embedded into a photonic crystal cavity. (c), (d) Relative position of the intrinsic region of the pin diode with respect to the field distribution (E_y) of the first and second order modes respectively.

cause of their relatively high quality factor and small mode volume. The $2\ \mu\text{m}$ wide intrinsic region is chosen to reduce the diode resistance and at the same time to avoid any overlap between the high intensity regions of the two modes with the high doping regions, which may otherwise result in large free carrier absorption and reduce the quality factor of the cavities. And the $5\ \mu\text{m}$ width is chosen to maximize the overlap between the optical mode and the intrinsic region of the diode while keeping the diode capacitance low (as shown in Fig. 4.2c and 4.2d).

4.3.2 Mask Design

The fabrication process involves eight lithography steps, two of which are e-beam lithography and six are photolithography steps. The steps are summarized in Table 4.1.

A photo-mask is designed containing all the layers for the photolithography steps. The first layer consists of alignment marks and electrical isolation trenches. The alignment marks are required to maintain alignment between the different steps during the fabrication process. To avoid unwanted leakage current between the p⁺ and n⁺ regions and to confine the electron flow to the photonic crystal, isolation trenches are used around the n⁺ doped regions, as shown by the gray region in Fig. 4.3a. The second and third layers contain n⁺ and p⁺ doping windows. The doping regions are designed to keep all the vias on the same side of the silicon nitride waveguide to avoid any contact layer on top of the waveguide. As a result, the p⁺ doping window is wrapped around the cavity, as shown in Fig. 4.3a. This also facilitates testing of the device with high speed ground-signal-ground RF probes. The fifth layer con-

Layer No.	Layer description	Layer Resolution	Lithography technique
1	Alignment marks and isolation trenches	Low	Photo Lithography
2	n-type doping window	Low	Photo Lithography
3	p-type doping window	Low	Photo Lithography
4	Photonic crystal cavity	High	E-beam Lithography
5	Window for opening alignment marks	Low	Photo Lithography
6	Silicon nitride waveguide	High	Photo Lithography
7	Via	Low	Photo Lithography
8	Lift-off window for metal contact	Low	Photo Lithography

Table 4.1 – Description of the mask layers used for fabrication

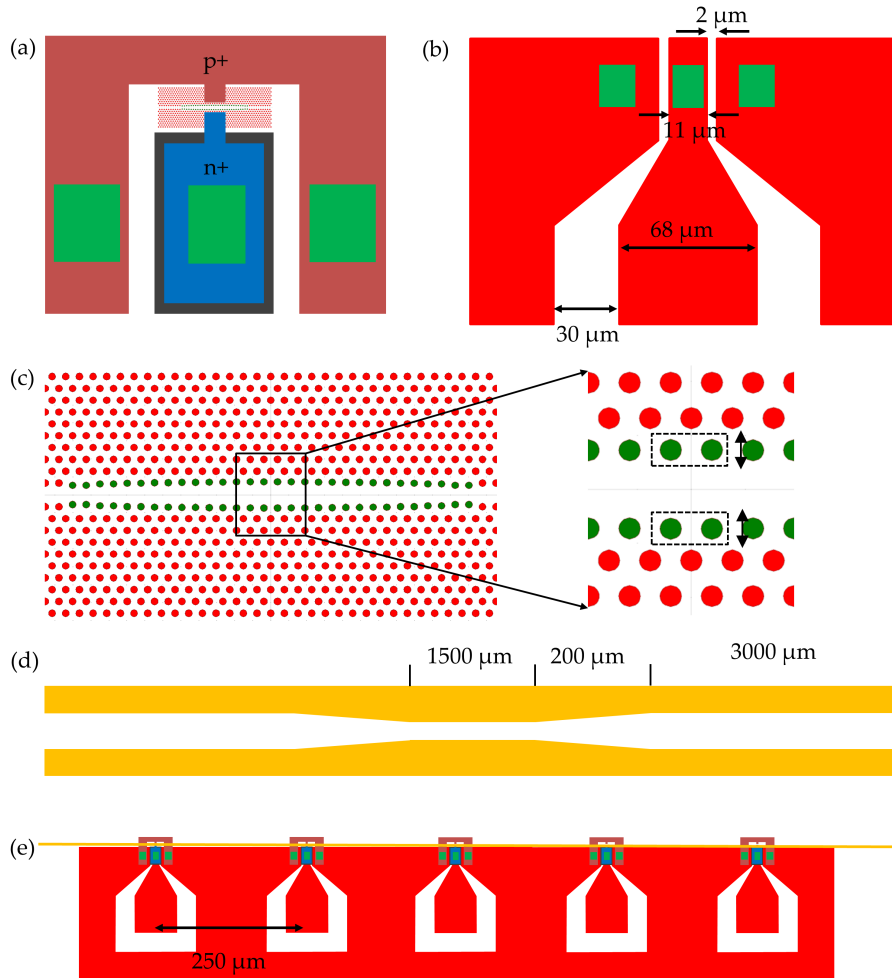


Figure 4.3 – (a) Relative position of the photonic crystal cavity and the p^+ and n^+ doping regions. The green region shows the position of the vias. (b) The position of the metal electrodes with respect to the vias. (c) Dispersion adapted cavity. The shifted holes are represented by green circles. All five cavity designs are identical, except for the positions of the four innermost holes of each cavity, which were tuned to achieve the required resonance wavelength. (d) Dimension of the Si_3N_4 waveguide. (e) A complete view of the device containing all layers.

tains windows for etching the silicon nitride and oxide layers on top of the alignment marks. Although both layers are transparent under visible light, they are opaque for an electron beam. Therefore, no silicon nitride or oxide should be present on top of the alignment marks. Vias are drawn on layer seven. They are required to open windows in the oxide layer in order to enable contacts to the doped regions. These oxide windows are positioned in such a way that any small misalignment during fabrication will not allow the metal to be in contact with undoped areas on silicon as this would interfere with the electrical behavior of the diode. Finally layer eight contains the metal electrodes. The electrode ground area covers the vias on p^+ regions and the central electrode covers the vias on n^+ regions. The electrodes are drawn for lift-off process so that only metal inside the window is left on the chip. The electrodes are designed to match the $100\ \mu m$ pitch of a $50\ \Omega$ RF probe used to test the device. Also the width and separation of the central electrode is designed to match the $50\ \Omega$ impedance of a coplanar waveguide to avoid any reflections of the microwave signal. The relative position of the windows for vias and metal electrodes are shown in Fig. 4.3b, where red and green regions represent the electrodes and the vias, respectively.

4.3.3 Fabrication

The device is fabricated on a silicon-on-insulator platform with $220\ \text{nm}$ silicon layer on a $2\ \mu m$ buried oxide layer (Fig. 4.4a). The isolation trenches and alignment marks are first transferred onto silicon layer using photolithography and dry etching. To create n^+ doping regions, the sample is spin coated with a positive photoresist S1818. After baking at 100°C to drive-off the solvent, the thickness of the resist layer is $\sim 2\ \mu m$. This thickness is sufficient to block any doping in the unwanted region on silicon. Areas corresponding to five n^+ doping windows are then exposed on the photoresist using photolithography and developed using MF319 UV photoresist developer (Fig. 4.4b). The sample is then doped with phosphorous using ion implantation to give a doping density of $1 \times 10^{19}\ \text{cm}^{-3}$. Similarly, the p^+ regions are doped with boron to give a doping density of $5 \times 10^{19}\ \text{cm}^{-3}$ (Fig. 4.4c). The high doping density for the p-region was chosen to compensate for the extra resistance arising from the extra length of p-type region. Even though the doping creates free-carrier losses, it has been reported that quality factors of 40,000 can be achieved even with carrier densities of $1 \times 10^{18}\ \text{cm}^{-3}$ at the center of the cavity [45], hence a doping density of $\sim 10^{19}\ \text{cm}^{-3}$ at a $1\ \mu m$ distance from the cavity center is not detrimental to the operation of the devices. Following the doping process, the sample is cleaned with Piranha (3:1 H_2SO_4 , H_2O_2) and then acetone and IPA to remove the photoresist. The sample is then annealed for 1 minute at 1000°C using a rapid thermal annealer (RTA) to activate the dopants.

After the annealing process, the sample is spin coated with 350nm thick e-beam photoresist ZEP 520A. Using electron beam lithography, the photonic crystal cavities are defined in the ZEP-520A layer (Fig. 4.4d) and the pattern is transferred into the silicon layer by reactive ion etching (RIE) (Fig. 4.4e). The entire device is then covered with spin-on-glass (FOx 14, Dow Corning)

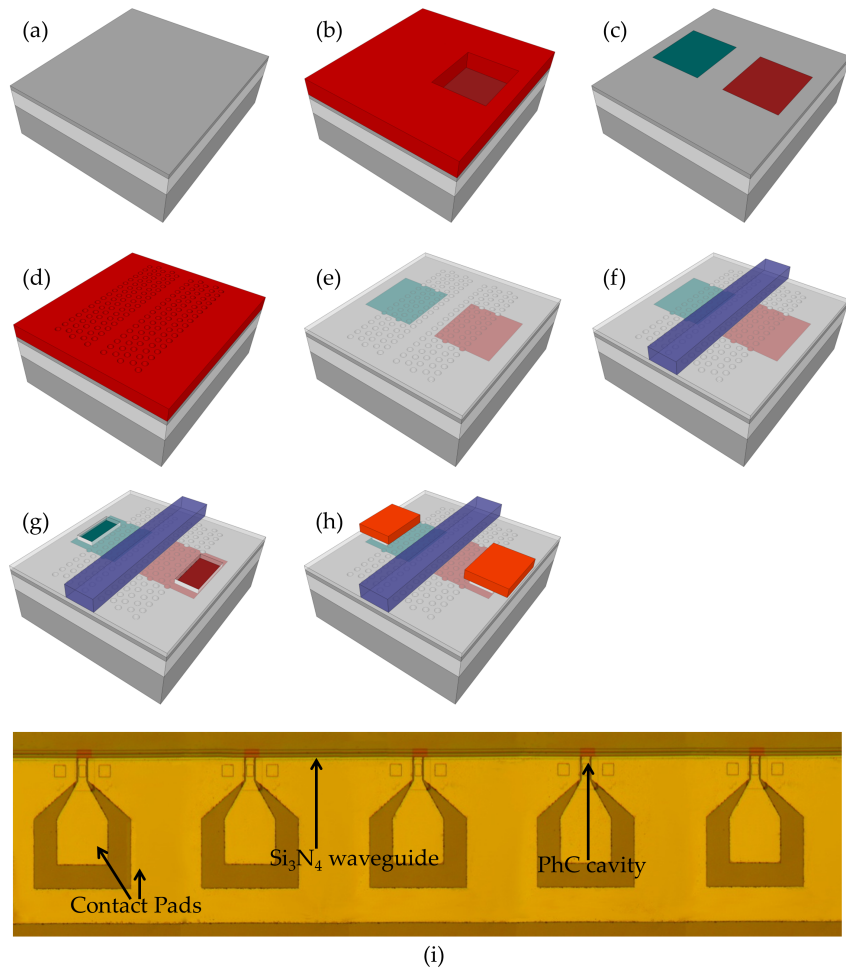


Figure 4.4 – Fabrication process: (a) A sample of SOI is cleaved from the wafer. (b) The sample is selectively ion-implanted through doping windows in the photoresist. (c) The sample is annealed to activate both types of implanted ions. (d) Using e-beam lithography and dry etching, photonic crystal patterns are transferred to the silicon layer. (e) The sample is covered in FOx and the FOx thickness is reduced to 200nm. (f) Si_3N_4 waveguides are fabricated using e-beam lithography. (g) Electrical vias are etched through the FOx layer. (h) Electrical contacts are formed using lift-off. (i) Top view of the cascaded PhC cavity based modulator set, where five cavities are coupled to a single silicon nitride waveguide.

(Fig. 4.4e). Although this process reduces the index contrast, it improves the CMOS compatibility of the final device, increases heat transport and allows us to control the coupling coefficient to the dielectric bus waveguide. The oxide layer thickness is then reduced to 200 nm by RIE. A 500 nm thick layer of silicon nitride is deposited using Plasma Enhanced Chemical Vapour Deposition (PECVD) and the waveguide is defined on top of all cavities by e-beam lithography and RIE (Fig. 4.4f). After defining the waveguides, vias are etched into the 200 nm thick oxide layer using photolithography and RIE (Fig. 4.4g). Finally the metal contacts are formed by depositing ~ 300 nm of aluminium using thermal evaporator and using lift-off process (Fig. 4.4h). The sample is annealed at 450°C to form an ohmic contact between the aluminium and the doped silicon. Finally, the sample is cleaved to form optical facets for measurement using the end-fire technique.

4.4 Characterization setup

The fabricated device was characterized at University of Southampton, especially for its high-speed modulation properties. Here, I provide a brief summary of the optical and electrical measurement setups.

4.4.1 Optical setup

A schematic of the optical characterization setup is shown in Fig. 4.5. An end-fire technique is used to couple light in and out of the device. The equipment used for the passive optical measurement are a computer operated tunable laser and detector, polarisation maintaining fibers, collimators, a quarter wave plate, a cube beam splitter, nano positioners, infrared cameras. The setup was designed in such a way that for further active device measurements, complementary components can easily be appended to the setup. The components for active measurements include a DC to 50 GHz microwave coplanar probe, DC power supplies, a bias tee (bias T), a DC to 50 GHz microwave signal amplifier, a signal generator going up to 70 GHz, a 40 Gb/s pseudo random bit generator with a demultiplexer, a low power high gain EDFA (erbium doped fiber amplifier amplifier), a tuneable optical filter and a high speed digital oscilloscope with optical and electrical inputs.

For the passive optical measurement, light from the tunable laser is fed to an objective lens (OL1) using a polarization maintaining fiber (PMF). The collimated output is mainly TM polarized. Using a quarter-wave plate ($\lambda/4$ -plate), the polarization of the beam is rotated to TE and any residual TM polarized light is filtered out with a polarization beam splitter (BS). The incoming free space TE polarized light is then focused onto the cleaved facet of one of the waveguides using a objective lens (OL2) and the transmitted light is collected from the other facet of the waveguide with objective lens 3. When the mirror 2 (M2) is flat, the collected light goes straight to the objective lens 4 (OL4) and is detected by the inbuilt photo-detector in the tunable laser.

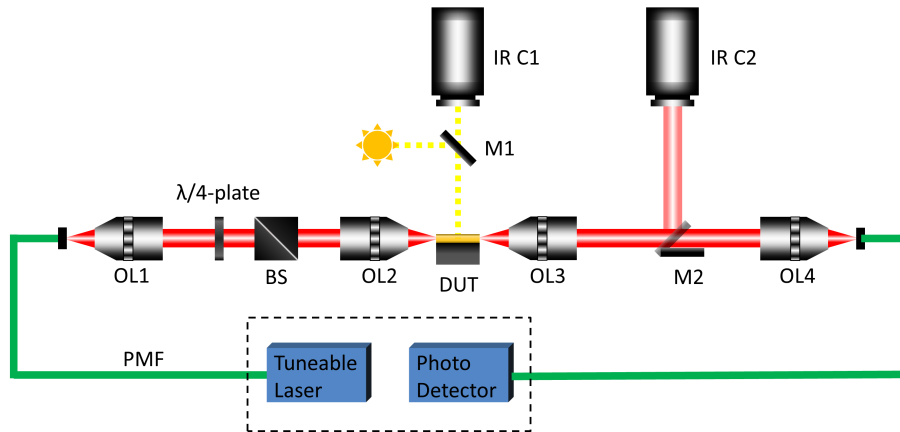


Figure 4.5 – Experimental setup for optical measurements. OL: Objective lens, BS: polarization beam splitter, DUT: device under test, M: mirror, IR C: infrared camera, PMF: Polarization maintaining fiber.

The two infrared cameras are mainly used to facilitate alignment of the collimating lenses with the waveguides on the device. Both cameras have a broad sensitivity range, ranging from the visible to the infrared. This allows us to see both the chip and the infrared light propagating through the device. The output infrared camera (IR C2) is used to align the output objective lens to the waveguide on the chip (by rotating mirror 2) and to monitor the output beam shape of the waveguide.

The tunable laser has a wavelength range from 1520 nm to 1640 nm, with a scanning resolution of 1pm. There are two scanning techniques available, stepped scan and sweep scan. The stepped scan is more accurate but consumes a significant amount of time (up to 12 hours for a full scan); during this time, the mechanical alignment of the setup will drift, resulting in an uncontrolled power variation. In contrast, the sweep scan only takes few minutes with a wavelength resolution of 4 pm. The resolution is sufficient for the measurement and also the fast scanning time avoids any power variation due to mechanical misalignment. Hence, I used the sweep scan for the passive optical characterization.

4.4.2 Electrical setup

For the DC characterization of the device, the additional components I have added to the existing optical setup are a Pico ammeter/Voltage, a bias T and a coplanar microwave probe for DC to 50 GHz operation (shown in Fig. 4.6). The IV measurements are performed with a Pico ammeter/Voltage source connected to the chip via a ground- signal-ground probe.

The schematic of the setup for high speed measurement is shown in Fig. 4.7. The aim is to modulate the optical intensity with pseudo-random electrical bit sequence (PRBS). The corresponding cycle of 1's and 0's is generated by a clock at the specified frequency. The clock drives the PRBS generator to produce two bits for each clock cycle in a non-return-to-zero (NRZ)

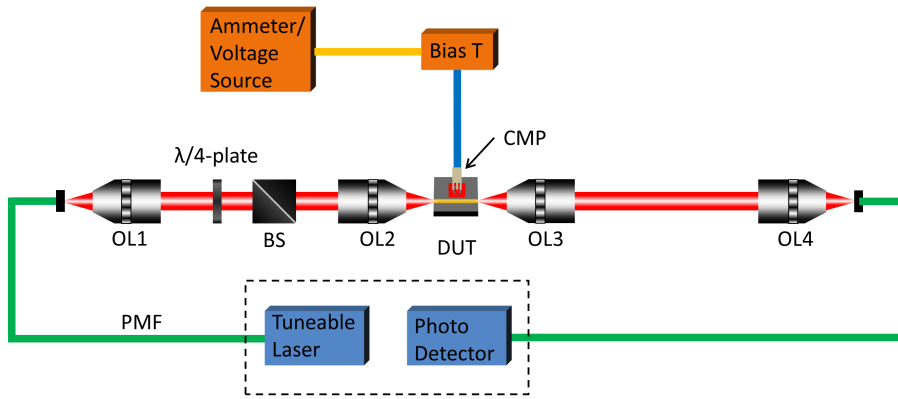


Figure 4.6 – Experimental setup for DC measurements. OL: Objective lens, BS: polarization beam splitter, DUT: device under test, M: mirror, PMF: Polarization maintaining fiber.

coding scheme. The PRBS differential outputs are connected to a clock and data demultiplexer that enable division of the bit rate by a factor of 2, 4 and 8. The demultiplexer output is then amplified by the microwave amplifier (the amplification gain being set by the supplied DC voltage) and a DC bias is applied to the signal through the bias T before it is sent to the chip. The modulated optical signal is amplified with an EDFA and any residual amplified noise is removed using a tuneable band pass filter centered at the wavelength set on the tuneable laser. The oscilloscope measures the extinction ratio and the data rate of the eye diagram as well as the rise and fall time of the pulses.

4.5 Optical characterization

Figure 4.8a shows the normalized transmission spectrum of the device, with each of the five transmission dips corresponding to one of the five cavities. As I mentioned earlier, the dispersion adapted cavity has multiple modes and any of them can be used for demonstrating electro-optic modulation. The first two modes have a reasonably high quality factor and the positions of the doping windows are considered in a way to cover most of the optical mode of the first two orders. Ideally, the first order mode should have been chosen for demonstrating low energy modulation, because of its high quality factor and relatively smaller mode volume. During the measurement, however, I found that the first order mode had a relatively low extinction ratio (<5 dB), while the second order mode had a relatively high extinction ratio (>10 dB), hence I focused on the second order mode. For the second order mode, the total quality factor of the cavities ranges from 10,000 to 15,000 with an extinction ratio ranging from 10 to 15 dB. This variation is caused by the slightly different k-space matching between the waveguide mode and the cavity modes. For the as-fabricated device, the five channels are not equally spaced (Fig. 4.8b); these channel spacing values can be further improved by trimming techniques such as laser assisted local oxidation [118], or by using

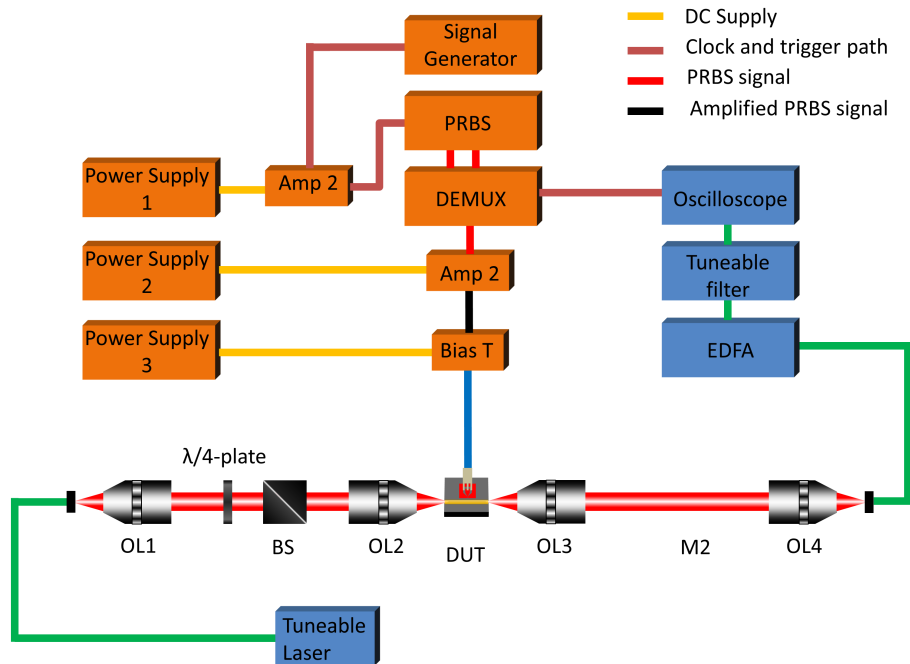


Figure 4.7 – Experimental setup for the high speed data rate measurements. OL: Objective lens, BS: polarization beam splitter, DUT: device under test, M: mirror, Amp: Amplifier.

highly efficient active tuning with integrated heaters [119].

4.6 Electro-optic modulation

4.6.1 DC characterization

The diode characteristics of all five modulators are measured by increasing the bias voltage across the pin junction and measuring the corresponding current flow. All the five IV curves are shown in Fig. 4.9a. Since the modulators are designed to work in the injection mode or, in other words, in forward bias mode, only the section of the IV curve is shown where the applied voltage is positive across the pin junction. Although the IV curves demonstrate a typical diode characteristic, the forward resistance is relatively high. Also, the cut-in voltage is quite high ($\sim 4\text{ V}$) in comparison to the cut-in voltage for typical pn diodes in silicon ($\sim 0.7\text{ V}$), which is a result of the high series resistance. This high series resistance is a result of the presence of holes of the photonic crystals in silicon and also because of high contact resistance arising from the metal contacts. We previously found that the contribution from the holes of the photonic crystal to the series resistance of the diode is in the range of few $\text{K}\Omega$ [45] and most of the resistance actually occurs at the metal-silicon contacts.

Figure 4.9b shows the shift in transmission of one of the cavities for different bias voltages. For injection type modulators, we would expect to see

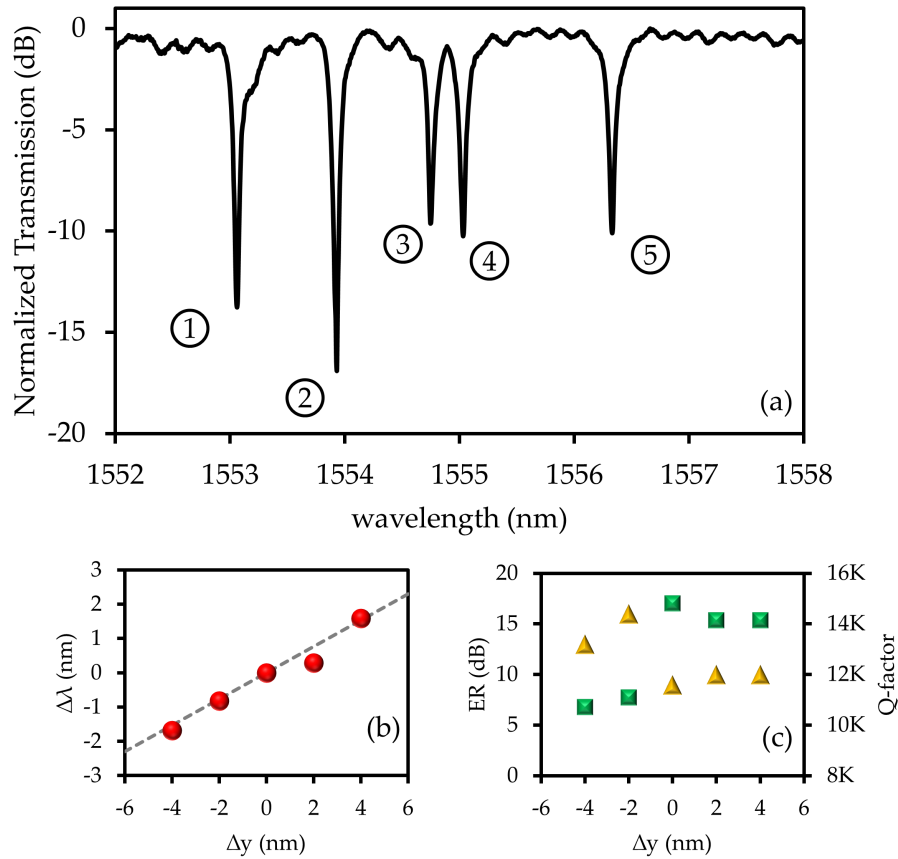


Figure 4.8 – (a) Normalized transmission spectrum of the Si_3N_4 waveguide vertically coupled to five PhC cavities, where each dip corresponds to a different cavity (b) Resonance wavelength shift due to the tuning of four central holes of the cavities with respect to the reference cavity. (c) Change in extinction ratio (yellow triangles) and quality factor (green squares) due to the tuning of the four central holes of the cavities.

a blue shift in the resonance wavelength of the cavity, due to the decrease in refractive index resulting from the injection of excess carriers inside the intrinsic region of the diode. Instead, we observe a negligible shift in resonance wavelength until the applied voltage reaches 6 V; only voltages above this value lead to redshift of the resonance wavelength. This abnormal behavior is due to the thermo-optic effect. As the applied bias increases from 0 V, the excess carrier concentration inside the intrinsic region increases, which causes a blue shift in the resonance wavelength of the cavity; at the same time, due to high series resistance of the diode, the temperature of the cavity also increases, which causes a redshift in the resonance wavelength. Both of these shifts tend to cancel each other, hence we do not see a net shift in the resonance wavelength until the forward bias reaches 5 V. Above 5 V, a further voltage increase causes a larger thermo-optic shift than the electro-optic shift does, so a net red-shift occurs. Due to this interplay between electro-optic and thermo-optic effects, the DC measurement is not a conclusive proof for electro-optic modulation, so we have to rely on high speed measurements.

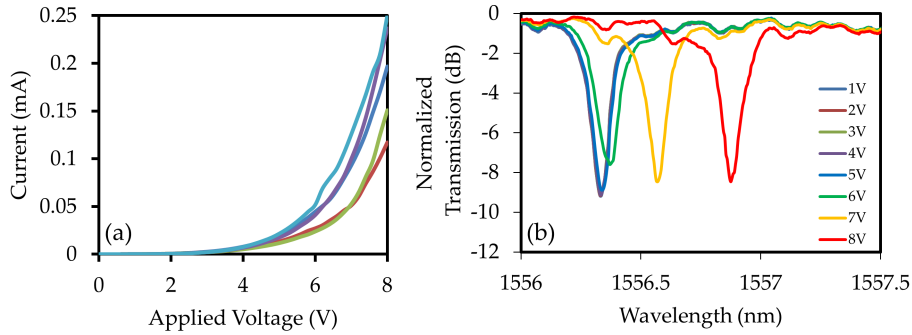


Figure 4.9 – (a) IV characteristics of all the five cavity modulators. Since we are operating in injection mode, only region above 0V is shown. (b) Normalized transmission spectra around the resonance wavelength of the fifth cavity for different bias voltages.

4.6.2 High speed measurement

To demonstrate high speed operation of the modulators, the setup shown in Fig. 4.7 is used. A 127 bit long pseudo random bit sequence is used to drive the photonic crystal cavities electrically and the electrical signal was applied to the devices via the high speed RF probe. An additional DC bias was added via the bias T. Due to the high contact resistance, the voltage drop at the metal-silicon interface is large. As a result, no modulation is observed up to a bias voltage of 4 V. Figure 4.10a and 4.10b show the eye diagrams of the modulated optical output at 0.5 Gbit/s and at 1 Gbit/s respectively, for the second modulator. As we can see, the eye is wide open at 0.5 Gbit/s, while at 1 Gbit/s, it is almost closed. A further increase in the speed of the driving signal results in a completely closed eye. This is expected from the current device, as I am using carrier injection, so the speed is limited by the free carrier lifetime in the intrinsic region of the pin diode. This is not a fundamental limitation of this resonant approach, however, rather it depends on the electrical design that I have chosen. For example, for a quality factor of 15,000, the photon lifetime is ≈ 12 ps in the cavity, which corresponds to a modulation speed of 10s of GHz. Hence the device speed is mainly limited by the electrical design rather than optical design.

One important point to note here is the driving voltage. A 0.7 V peak to peak voltage of the driving signal is required to get a 3.5 dB extinction ratio at 1 Gbit/s modulation speed. Due to the small mode volume of the photonic crystal cavity, such a small driving voltage is sufficient to turn the device on and off. A small driving voltage suggests that the AC power consumption of the device is also low. If we neglect the presence of any capacitive effects, The AC component of the power consumption can be calculated as $P_{ac} = V_{rms}^2/R$; where V_{rms} is the root mean square value of the driving signal. Assuming a sinusoidal signal, $V_{rms} = 0.3535 \times V_{pp}$, V_{pp} is 0.7 V and R is 100 K Ω for the device at the 4 V DC bias. Thus the AC power consumption is 0.6125 μ W and at 1 Gbit/s modulation and the AC energy consumption is ~ 0.6 fJ/bit. The total power consumption, due to

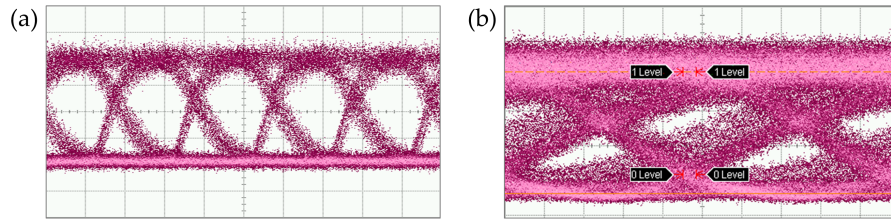


Figure 4.10 – Eye diagrams of the modulated optical output of the second modulator at (a) 0.5Gbit/s and (b) 1.0Gbit/s respectively. Horizontal scale: 1ns/div for 0.5Gbit/s and 200ps/div for 1 Gbit/s.

the additional 4V DC bias, is $38 \mu\text{W}$. Such a high DC power consumption results from the high resistance of the current device and can be reduced significantly by improving the metal-silicon contact.

A more fundamental indication of the device performance is the switching energy. Switching energy is defined as the energy required for a transition from the OFF state to ON state. To calculate the switching energy, I follow a similar method used in [68]. For an input voltage swing of 700mV, the extinction ratio is 3.5 dB at 1 Gbit/s, which corresponds to a resonance wavelength shift of 20 pm and a refractive index change in the silicon device layer of $\Delta n = 4.48 \times 10^{-5}$. This refractive index change corresponds to a carrier density change of $\Delta N = 6.7 \times 10^{15} \text{ cm}^{-3}$ in the intrinsic region of the modulator. Given the physical volume of the intrinsic region of $2.2 \mu\text{m}^3$, the switching energy for our device is therefore approximately 1.6 fJ, which is amongst the lowest ever reported.

Finally, to observe multiplexing, the driving signal is applied successively to each modulator and the modulated optical output is recorded at the resonance wavelength of each individual modulator. Figure 4.11 shows the eye diagrams of the five channels, each operating at 0.5 Gbit/s. To improve the extinction ratio further, the peak-to-peak voltage of the driving signal was set to 1.7V. This resulted in an extinction ratio of more than 7 dB for each channel. Increasing the driving voltage also increases the AC power consumption to $3.6 \mu\text{W}$, which is still one order of magnitude smaller than for conventional ring resonator based devices. The PRBS sequence used is 127 bit long. A longer sequence would have generated a much broader range of 1 and 0 variations, thus providing a better eye diagram, but this was not available.

4.6.3 Multi-wavelength operation using comb laser

Finally, to demonstrate the full potential of this approach, a multi-wavelength laser source is used to feed all five modulators. Here, I use a multi-wavelength comb laser source [127] with a spacing of 50 GHz (0.44 nm) between each channel, shown in the inset of Fig. 4.12. The resonance wavelength of each of the five cavities are actively tuned by adjusting the DC bias, which has the effect of thermo-optically tuning the resonances to match five consecutive lines of the comb laser as shown in Fig. 4.12a. Fig. 4.12b shows the output

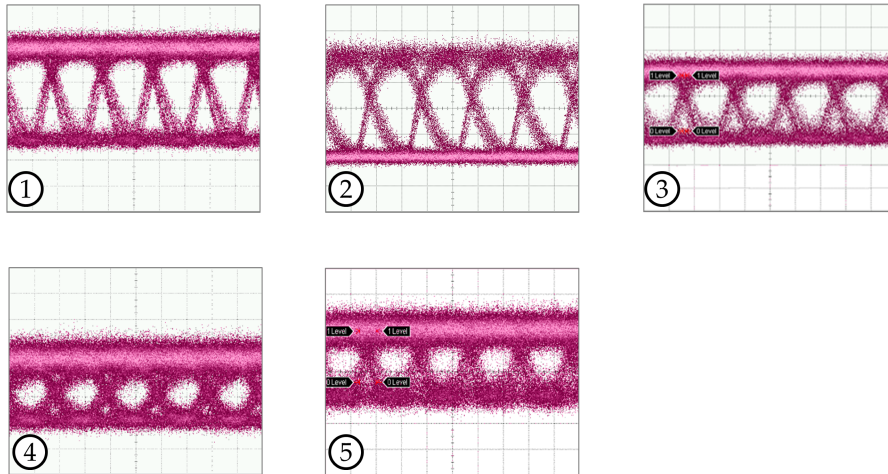


Figure 4.11 – Eye diagrams at 0.5Gbit/s for all the five cavity modulators. Open eyes were observed for each channel. Horizontal scale: 1ns/div

spectrum of the waveguide when none of the cavity wavelengths are aligned with the lines of the laser (each spike was normalized to unity for clarity) and Fig. 4.12c shows the same spectrum when the cavities are aligned to the lines of the comb laser. These results clearly demonstrate the scalability and multi-wavelength operation of our architecture.

4.7 Discussion

This section summarizes the main results and presents the conclusions that can be drawn. In Chapter 3, I have shown how efficient coupling between a vertically placed low index bus waveguide and a high index silicon photonic crystal cavity can be achieved by carefully matching the k-spaces of the two modes. Here, the same vertically coupled system is used to demonstrate a compact cascaded modulator architecture for WDM applications. The k-space matching technique allows effortless transfer of light from low refractive index passive components into high index active layers. The attraction of deposited layers, such the silicon nitride used here, for on-chip networks has already been highlighted [31], as the low loss and relatively tight bending radii make such waveguides ideal for the realisation of complex passive on-chip networks. Our technique solves the problematic interfacing between the active (silicon) and passive (silicon nitride) components allowing the full potential of on-chip networks to be realized. Additionally, the potentially sub-dB insertion losses of these waveguides [54] are ideal for the off-chip connections. Finally, by removing the bus waveguide from the active device layer and placing it above the silicon device layer, the area available for electronic circuitry is maximised, while keeping the active photonics in crystalline silicon- a further advantage for front-end CMOS integration. Ultimately, the key advantages of our approach derive from the high finesse of the photonic crystal cavity. Only a high finesse cavity can combine small size, therefore

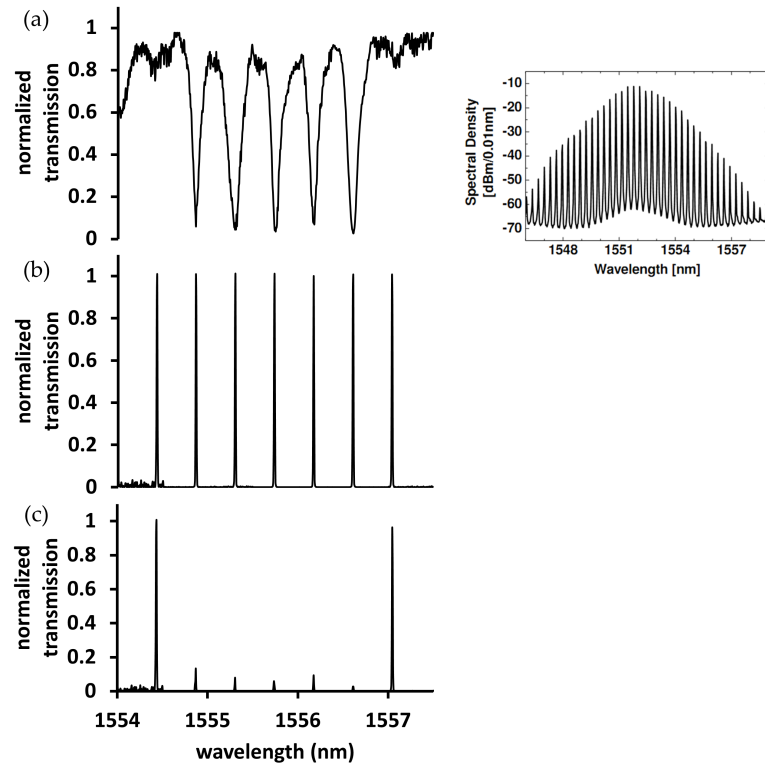


Figure 4.12 – (a) Normalized transmission spectrum of the bus waveguide with a tunable laser when each cavity is actively tuned to match the comb laser spectrum, (b) normalized transmission spectrum of the bus waveguide with the comb laser when cavity resonances are not aligned with the comb laser spectrum, (c) normalized transmission spectrum of the bus waveguide with the comb laser when cavity resonances are aligned with the comb laser, inset shows the comb laser spectrum

low capacitance, with narrow bandwidth and large free spectral range, which singles out the photonic crystal approach as uniquely advantageous.

I have demonstrated how an array of such cavities can be operated with a single source, i.e. a comb laser, to achieve on-chip WDM operation, one of the first demonstrations of this kind. The switching energy (Off-On state) is only 1.6 fJ, one of the lowest yet reported for a silicon electro-optic modulator. The device speed is relatively low; this is due to the injection mode operation employed here. The demonstrated speed, however, is not a fundamental limit, as depletion-type modulation, for example, can easily achieve the carrier density change of $5 \times 10^{15} \text{ cm}^{-3}$ required for a 3 dB extinction ratio and much higher modulation speeds; modulation speeds up to 50 Gbit/s have already been demonstrated [60] and have also been shown to be compatible with PhC designs [66]. Due to the small device area, fF capacitances can also be realized. For operation in carrier depletion mode, the power consumption is determined only by the switching energy and from the earlier numbers, values of 0.4 fJ/bit could be expected (as the 0-1 transitions have a 0.25 probability of occurring).

Due to their large Free Spectral Range (FSR), it is straightforward to fabricate large arrays of single mode photonic crystal cavities for multichannel operation. The width of the photonic bandgap (+100 nm) is the ultimate limit making this technique very scalable. This scalability, combined with the low switching energy, the small footprint and the low insertion loss makes our architecture very suitable for dense WDM operation and has the potential for Tbit/s data transmission. Even with the low modulation speeds reported here, such a FSR could support the 1000 channels required for a Tbit/s data transmission with dramatically lower area and power consumption than other approaches. Increasing the modulation speed to a reasonable 10 Gbit/s reduces the channel number to very practical numbers.

Chapter 5

Cascaded Detector Architecture

5.1 Introduction

The crystalline silicon-on-insulator platform enables modulation and low loss waveguiding in the telecommunication windows centered at $1.3\ \mu\text{m}$ and $1.55\ \mu\text{m}$ wavelengths. These functionalities can be implemented in bulk crystalline silicon due to its 1.12 eV band gap which does not produce any significant linear absorption beyond $1.1\ \mu\text{m}$ wavelength. Because of this transparency, a lot of progress has been made in silicon-based modulators and low loss passive components. The downside of this low absorption is that it is difficult to build another essential element of an optical interconnect, namely the detector.

Detection is therefore typically realized with hybrid materials such as III-V material-on-silicon or germanium-on-silicon. III-V compound semiconductors can be integrated on top of silicon waveguides using a wafer bonding process [128, 129]. This is not ideal due to the incompatibility of III-V material with silicon CMOS processing. The preferred alternative is to integrate germanium as the absorbing material using selective epitaxial growth of germanium on silicon. Several research groups have already demonstrated efficient germanium based photodetectors with high responsivity, low dark current and high detection speed [76, 77, 78]. Unlike III-V materials, germanium is CMOS compatible and is being used in CMOS foundries to create strained silicon and silicon-germanium (SiGe) transistors. However, the epitaxial growth of germanium on silicon requires complex processing steps to manage the 4% lattice mismatch between the two crystals. Due to the associated fabrication complexities and CMOS compatibility issues, both of these approaches can affect the production yield, cost and flexibility. Besides, due to their broadband absorption spectrum, incorporating such detectors in wavelength division multiplexing (WDM) systems require the addition of demultiplexers such as arrayed waveguide gratings (AWG) or ring resonators to separate the different wavelength channels [77, 130]. These demultiplexers contribute to the overall optical loss and introduce additional complexity to the system design.

In order to avoid the complexities associated with heterogeneous integration, an all-silicon approach is very desirable. Although crystalline silicon is not an obvious choice for photo-detection, it is possible to introduce defects to enhance the sub-bandgap absorption. Such defects can be introduced by adding impurities (e.g. Erbium ions) or lattice point defects (interstitials or vacancies) into the crystal structure, which tend to form deep levels that allow absorption far into the bandgap. Optical detection using such deep levels has been reported by several research groups and the resulting performance was found to be comparable to the germanium or III-V material based photo-detectors [32, 80, 92]. In addition, defect-based detectors have a number of advantages over conventional photo-detectors. Firstly, they are completely CMOS compatible. Secondly, fabrication of defect detectors does not require any complicated wafer bonding or epitaxial growth and only requires a single ion-implantation step. The disadvantage, however, is that the defects need to be introduced late in the process, i.e. at the back-end, as they tend to anneal out at temperatures above 300°C [131].

In this chapter, utilizing this defect detection technique I realize photodiodes with 0.108 A/W responsivity and a 9.4 nA dark current at a wavelength around 1.55 μm . Here I use the vertically coupled structure, introduced in Chapter 3, to demonstrate optical detection, and thereby completing the optical interconnect. Due to the strong optical confinement in the photonic crystal cavity, the light-matter interaction is enhanced, thus resulting in a smaller device size. This in turn results in a smaller dark current, which is mainly decided by the device size. Moreover, due to the small mode volume of photonic crystal cavities, the device capacitance can be very small (in atto-Farads [72]) suggesting an inherently faster device and can potentially avoid the need for an electrical amplifier (receiverless mode [132]) in real device implementation. Finally, the vertical coupling geometry offers easy cascading of multiple detectors without needing any complex demultiplexer circuits.

5.2 Sub-bandgap detection in silicon

In indirect bandgap semiconductors, such as silicon or germanium, electron-hole pair generation via photon absorption happens in two stages, as shown in Fig. 5.1a. Upon the incidence of a photon (with energy more than the bandgap energy of the semiconductor), an electron at the valence band maxima makes a transition to the conduction band at the same position with the same momentum, leaving behind a hole in the valence band. In the conduction band the electron then makes another rapid transition to a lower energy level. This second transition is facilitated by a transfer of momentum to the crystal in the form of a phonon. This generated electron-hole pair is free in their respective bands and they become mobile and can drift under an applied electric field, thus generating photo-current. Any photon with energy less than the band gap energy will simply pass through the medium without being absorbed.

Due to its relatively large bandgap, silicon has a very low absorption

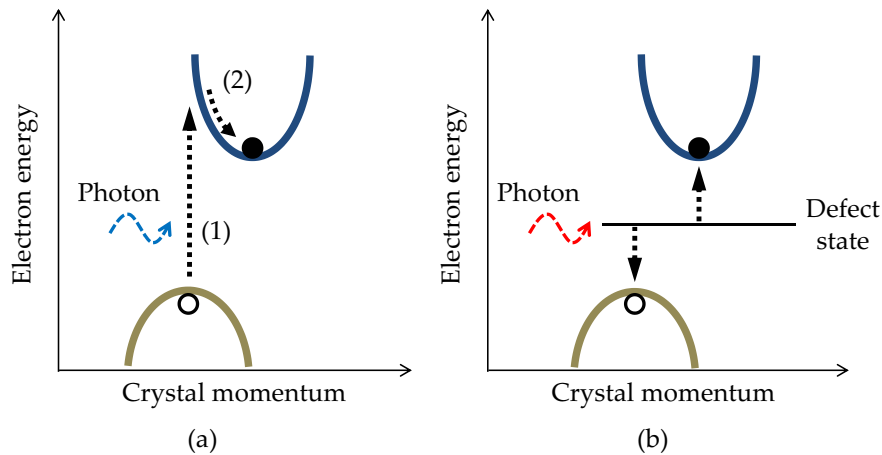


Figure 5.1 – (a) Generation of an electron-hole pair when a photon with energy equal to or more than the bandgap energy is absorbed. (b) Process of electron-hole pair generation using a defect state within the bandgap when a sub bandgap energy photon is absorbed. Open and filled circles represent hole and electron respectively.

coefficient beyond $1.1 \mu\text{m}$. Therefore, silicon is most commonly used for detection in the visible range of the electromagnetic spectrum. But for infrared communication wavelengths, crystalline silicon is incompatible for optical detection. In order to increase the sensitivity at wavelengths beyond $1.1 \mu\text{m}$, localized defect states must be introduced by disrupting the intrinsic periodic structure of bulk crystalline silicon. The process of generation of electron-hole pairs via a defect level is illustrated in Fig. 5.1b. These carriers can then be swept out by an applied electric field and collected as photocurrent before they can relax back to the ground state. Thus, via sub-bandgap defect states optical absorption of low energy photons is possible.

A number of different techniques have been proposed to introduce such deep levels into silicon. The simplest way is to create surface states via dry etching, although this has not proven to be very successful; the resulting responsivity, for example, was relatively low, i.e. 0.036 A/W in thin waveguides [133] and 0.00025 A/W in ring resonators [134]. Alternatively, trap levels can be introduced by doping with erbium ions, as demonstrated by Kik et al. [135]. It is well known that Er^{3+} ions can be electrically excited and emission at around $1.5 \mu\text{m}$ can be achieved. In this detection scheme, a reverse process was used where the Er^{3+} doped Si p-n junction generates photo current when illuminated with light at $1.5 \mu\text{m}$. The measured quantum efficiency of a 4 cm long device was only 10^{-3} . This poor detection efficiency can be attributed to the low solubility of Er^{3+} ions in silicon and lack of active Er^{3+} ions [136]. Another technique demonstrated by Preston et al. is to use the sub-bandgap absorption in polycrystalline silicon [32]. Infrared absorption in polysilicon is mainly due to the sub-bandgap states arising from dangling bonds. Preston et al. demonstrated a responsivity of 0.15 A/W with 1 Gbit/s detection speed using this technique, which is quite

impressive. The most effective method, however, is to irradiate the material with high-energy ions. This process creates mobile defects such as interstitials and vacancies, which are readily incorporated into the crystal structure. Using this technique, Geis et al. realized a photo-diode with responsivity of 0.8 A/W at -20 V with a silicon rib waveguide, highlighting the viability of the approach [137]. The main drawback, however, is that the absorption coefficient is relatively weak; hence long waveguides with a large footprint are required. In order to reduce the footprint, Doyle et al. reported a ring resonator based detector [92]. Because of multiple round trips inside the ring, the incident optical power effectively gets multiplied, thus improving responsivity without increasing the device length or the defect density. Using an 80 μm long race track type ring resonator, they demonstrated a responsivity of 0.14 A/W at a reverse voltage of -10 V with a leakage current less than 0.2 nA for the wavelength range 1510 nm-1600 nm.

In this chapter, I study the detection efficiency of defect-detectors based on high energy ion irradiation and using photonic crystal cavities to enhance the light-matter interaction. One of the advantages of high-energy ion implantation over using polycrystalline silicon is that the defect density can be optimized by controlling the implantation parameters such as dose and energy. The absorption can also be localized by selective implantation, whereas in the polycrystalline case, the entire device experiences the same loss.

5.3 Device design and fabrication

5.3.1 Design consideration

A sketch of the detector is shown in Fig. 5.2a, which highlights how the photonic crystal cavity is embedded into a reverse biased pin diode. Similar to the modulator design in Chapter 4, the gap between the doped regions of the diode is chosen to be 2 μm and the width of both the regions is 5 μm . The center of the intrinsic region coincides with the center of the photonic crystal cavity. The defects discussed above are then introduced into the intrinsic region of the diode using ion implantation. The photonic crystal cavity is coupled to a vertically placed silicon nitride waveguide and separated by a 200 nm thick oxide layer. The silicon nitride waveguide is 1.5 μm wide and 500 nm high.

Light couples from the waveguide mode to the cavity mode on resonance. Some of this light is lost due to scattering or radiation or absorption in the cavity while the rest couples back into the waveguide. The coupling efficiency between the waveguide mode and the cavity mode is optimized by maximizing the overlap between the k-space distributions of the two modes. Details of the coupling mechanism have already been discussed in Chapter 3. The sub-bandgap deep levels convert the absorbed light into photo-generated carriers which are then extracted as photocurrent via the applied reverse bias.

In Chapter 3, while studying the coupled waveguide-resonator system, our main focus was on the transmittance and reflectance of the device and the aim was to reduce the transmittance and increase the reflectance in order

to achieve a good extinction ratio. This was done by lowering the optical loss in the cavity and increasing the coupling efficiency between the waveguide mode and the cavity mode. Here, in order to use the same vertically coupled structure for photo-detection, the optical loss in the device needs to be optimized along with the transmittance and reflectance. Since absorption, a component of the optical loss, contributes to the extracted photocurrent, by maximizing the total absorption we can also maximize the photocurrent and overall photodetection efficiency of the system. In order to determine the optimum condition for photodetection, I rewrite the expressions for transmittance (T), reflectance (R) at resonance wavelength of the coupled system.

$$T = \frac{\Gamma_o^2}{(\Gamma_o^2 + \Gamma_c^2)} \quad (5.1)$$

$$R = \frac{\Gamma_c^2}{(\Gamma_o^2 + \Gamma_c^2)} \quad (5.2)$$

Since the optical loss in the waveguide is negligible, the sum of transmittance, reflectance and optical loss in the cavity is unity. Γ_c represents the decay rate of the cavity mode into the waveguide and Γ_o represents the decay rate of the cavity mode due to scattering and radiation (Γ_s) and absorption (Γ_a). We can therefore express the cavity decay rate as:

$$\Gamma_o = \Gamma_s + \Gamma_a \quad (5.3)$$

In Fig. 5.2b, transmittance, reflectance and optical loss are plotted as functions of Γ_o/Γ_c . We can see that as Γ_o/Γ_c increases from zero the transmittance of the system also increases and reflectance decreases monotonously, whereas the optical loss initially increases rapidly, then reaches a maximum when $\Gamma_o/\Gamma_c = 1$ and then decreases slowly as Γ_o/Γ_c increases further. From this analysis we can identify the optimum conditions for photodetection as :

1. $\Gamma_a \approx \Gamma_o$; i.e. the optical loss is mainly dominated by the absorption.
2. $\Gamma_o = \Gamma_c$; for this condition, transmittance and reflectance both are 0.25, i.e. -6dB and optical loss is 0.5, i.e. -3 dB. This is the so-called critical coupling for standing wave resonator (note the different form to that familiar from ring resonators [138]).

These two conditions suggest that as long as scattering is much lower than absorption, an internal quantum efficiency of 0.50 may be achieved regardless of the strength of the absorbers.

The cavity considered here is the same dispersion adapted (DA) cavity [96] that was used for demonstrating modulation in the vertically coupled architecture. The DA cavity is a high quality factor cavity and hence both Γ_s and Γ_a are very small when bulk crystalline silicon is used. The vertical coupling technique allows us to increase the coupling of light into the cavity mode from the waveguide mode with minimum effect on Γ_o ; in other words, the intrinsic Q-factor of the cavity remains almost unaltered, as explained in chapter 3. By introducing lattice defects into the cavity region, it is possible

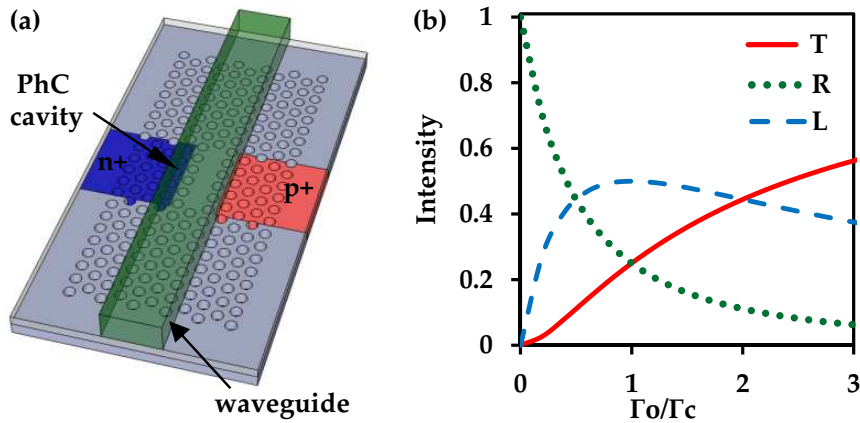


Figure 5.2 – (a) Schematic of the device, where the defect implanted photonic crystal cavity and the bus waveguide are vertically coupled through a buffer layer. An arbitrary photonic crystal cavity is shown in the schematic for illustration purposes. The design of [96] is used in our experiment. (b) Theoretical plot of transmittance (T), reflectance (R) and optical loss (L) against Γ_o/Γ_c at resonance wavelength, using coupled mode theory.

to increase the value of Γ_a without affecting Γ_c and Γ_s , so the optical loss will be dominated by defect-mediated absorption. Furthermore, by optimizing the concentration of defects, it is possible to achieve $\Gamma_c = \Gamma_o$, which is the optimum situation for achieving maximum absorption and converting the maximum amount of incident light into photocurrent in the detector.

5.3.2 Mask design and fabrication

The fabrication process involves nine lithography steps, six of which are photolithography steps and three are e-beam lithography steps. Due to the similarity between the modulator and photodetector designs, the same photomask is used for all of the photolithography steps; the only difference being the additional ion implantation step for introducing defects. A summary of the complete fabrication process is given below.

The device is fabricated on a SOI platform with 220 nm of silicon and $2\mu\text{m}$ of buried oxide (Fig. 5.3a). n^+ and p^+ doped regions, separated by $2\mu\text{m}$, were created using ion implantation of Phosphorous and Boron ($\sim 10^{19}\text{ cm}^{-3}$), respectively (Fig. 5.3b and 5.3c). Using e-beam lithography, the photonic crystal cavity designs are defined in the ZEP-520A layer and the pattern is transferred into the silicon layer by reactive ion etching (RIE) (Fig. 5.3d). The entire device is then covered with spin-on-glass (FOX-14, Dow Corning) (Fig. 5.3e). The oxide layer thickness is reduced to 200nm by RIE and a 500nm thick layer of silicon nitride is deposited using plasma-enhanced chemical vapor deposition (PECVD) to allow defining the waveguide on top of cavity (Fig. 5.3f). After defining the waveguide, electrical contacts are created by etching via holes through the nitride and oxide layers (Fig. 5.3g) and depositing aluminium contacts by thermal evaporation (Fig. 5.3h). Af-

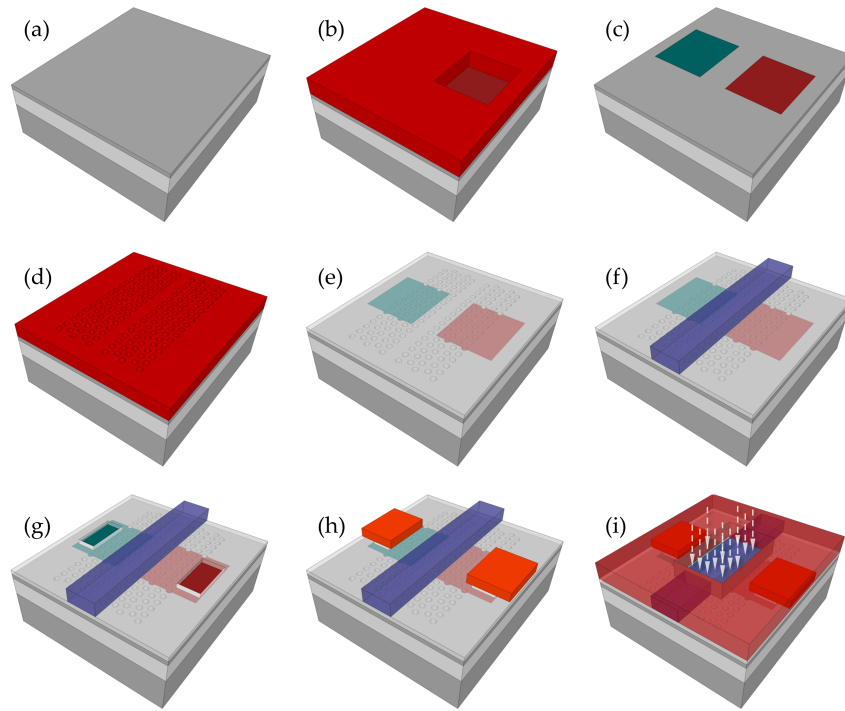


Figure 5.3 – Fabrication process: (a) A sample of SOI is cleaved from the wafer. (b) The sample is selectively ion-implanted through doping windows in photoresist. (c) The sample is annealed to activate both types of implanted ions. (d) Using e-beam lithography and dry etching, photonic crystal patterns are transferred to the silicon layer. (e) The sample is covered in FOX and the FOX thickness is reduced to 200nm. (f) Si_3N_4 waveguides are fabricated using e-beam lithography. (g) Electrical vias are etched through the FOX layer. (h) Electrical contacts are formed using lift-off. (i) Selective silicon implantation is done for creating the defect states.

ter contact metallization, the sample is spin-coated with a $2\mu\text{m}$ thick layer of ZEP-520A and defect implantation windows are opened above the photonic crystal cavities by e-beam lithography. The sample is then implanted with silicon at 6 MeV to a dose of $3 \times 10^{11} \text{ cm}^{-2}$ to introduce volume defects in the silicon layer (Fig. 5.3i). At this energy the silicon is situated below the buried oxide, so does not take part in the device operation beyond the introduction of defects during implantation. Finally the sample is cleaved to form optical facets for measurements.

5.4 Characterization setup

The optical and electrical characterization of the device was carried out at the University of Southampton. The measurement setup is similar to that of Chapter 4 (Fig. 5.4). For the optical characterization, an end-fire technique is used. Light from a tuneable laser source is first amplified using an erbium doped fiber amplifier and then passed through a polarization beam splitter and $\lambda/2$ plate allowing only TE polarized light to couple into the silicon

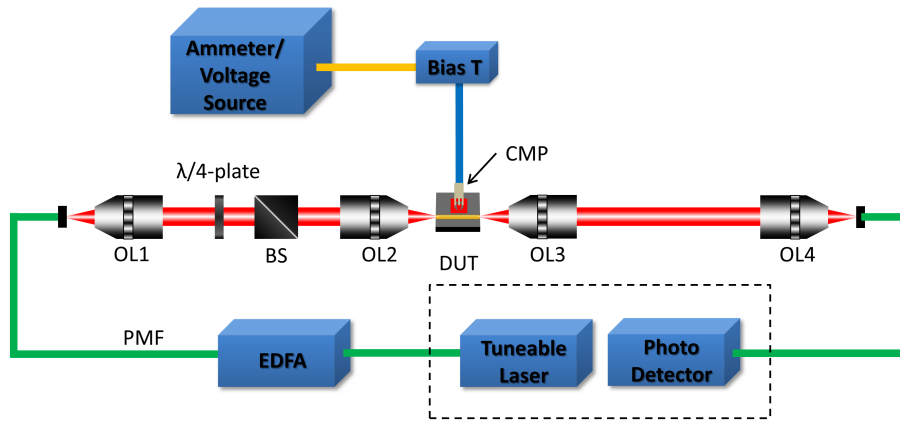


Figure 5.4 – Experimental setup for DC measurements. OL: Objective lens, BS: polarization beam splitter, DUT: device under test, CMP: coplanar metal probe, PMF: Polarization maintaining fiber.

nitride waveguide using an objective lens. The output light is then collected from the other end of the waveguide via a collimating lens coupler and passed to a detector. The IV measurements were performed using a pico ammeter/Voltage source connected to the chip via ground signal ground probe connection. This allowed for the photocurrent to be measured for each wavelength as a function of the reverse voltage. The wavelength/photocurrent scans were automated using Labview.

5.5 Measurements

To observe the relationship between transmittance and photocurrent at the resonance wavelength, five different detector designs are realized by varying the k-space overlap between the waveguide and the cavity modes, thus varying Γ_c in Eq. 5.1 and 5.2. I characterize the defect absorption by monitoring the transmittance (Eq. 5.1); the transmittance was well below -6 dB for the unimplanted devices, as Γ_c dominates over Γ_o . After implantation, the absorption increases and so do the cavity decay rate $\Gamma_o = \Gamma_s + \Gamma_a$ and the transmittance, until Γ_o and Γ_c balance. Fig. 5.5 plots the corresponding functional relationship as well as the generated photocurrent for the five different devices with different Γ_c values. Before defect implantation, the quality factors of the cavities were around 35,000, roughly corresponding to an equivalent propagation loss of 17 dB/cm. This loss arises mainly from scattering and free carrier absorption from the heavily doped regions of the pin diode. After defect implantation, the quality factor decreases to around 15,000, corresponding to an equivalent propagation loss of 40 dB/cm. This extra 23 dB/cm loss arises from the increase in defect density inside the cavity region. Thus, a large fraction of Γ_o is now contributed by Γ_a . It is clear from Fig. 5.5 that the maximum absorption occurs when $\Gamma_c = \Gamma_o$, in which case the transmittance equals -6 dB (0.25). In this optimum situation the maximum amount of light is absorbed and converted into photocurrent.

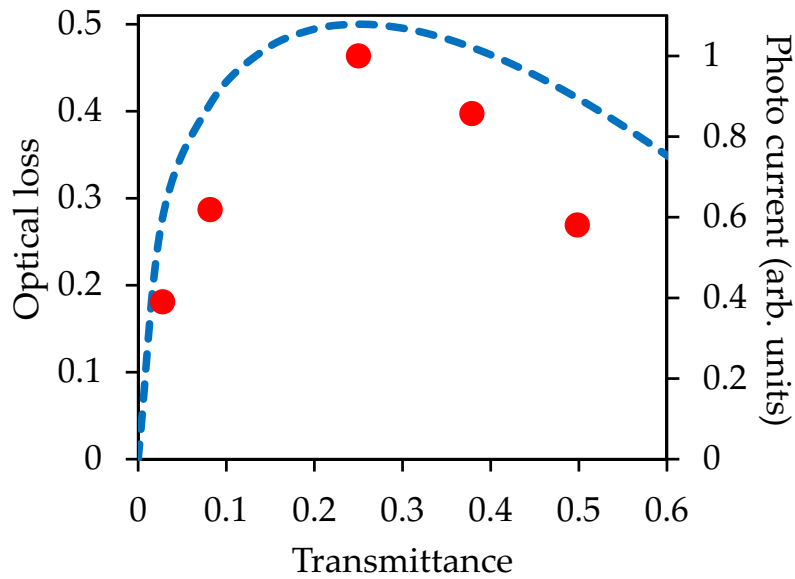


Figure 5.5 – The blue dashed curve shows the theoretical relationship between transmittance and optical loss of the system on resonance. The red dots show the measured photocurrents for five different detectors with different transmittances. The level of the red dots has been normalised to its maximum value, i.e. the graph highlights qualitative rather than a quantitative agreement.

Figure 5.6 shows the spectrum of the optical power in the waveguide immediately after the photonic crystal cavity (this is calculated from the measured transmission spectrum using the known losses) and the generated photocurrent for a near-optimal device. On resonance, the transmittance is 0.30 and by comparing this with the theoretical values in Fig. 5.2b, we can estimate the optical loss in the cavity to be 0.49 (-3.1 dB). The responsivity is defined as the ratio between the generated photocurrent and the total optical loss, which is -3.1 dB of the off-resonance optical power ($45 \mu\text{W}$). For 0 V reverse bias, the detector has a responsivity of 7 mA/W on resonance with a dark current of 0.5 nA. For a reverse bias of -10 V, the responsivity increases to 110 mA/W, and the dark current increases to 9.4 nA. The extinction ratio between the on-resonance photocurrent and off-resonance photocurrent is maintained at around 14 dB irrespective of the reverse bias.

5.5.1 Effect of power and bias voltage

Figure 5.7a shows the measured photocurrent versus wavelength near the resonance wavelength, as a function of the off-resonance optical power in the waveguide. The reverse bias is set to 0 V. As the optical power increases, a redshift in the wavelength is observed corresponding to the maximum photocurrent (shown in Fig. 5.7c) and also an asymmetry in the photocurrent response. This redshift can be attributed to the thermo-optic effect caused by carrier recombination inside the intrinsic region of the diode. When the off-resonance optical power increases from $20 \mu\text{W}$ to $85 \mu\text{W}$, the shift

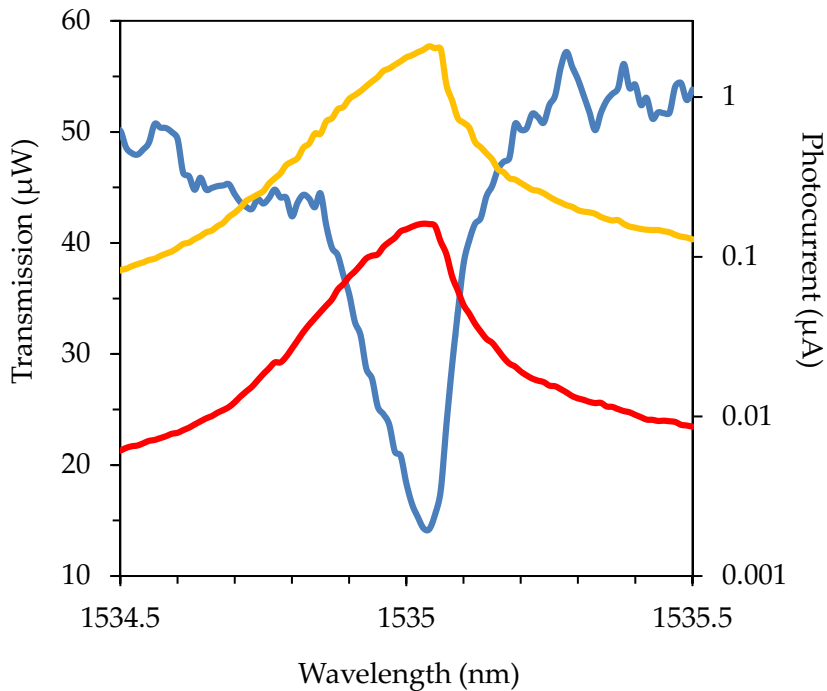


Figure 5.6 – Estimated optical spectra in the Si_3N_4 waveguide immediately after the cavity (blue) and measured photocurrent at photocurrent at 0V (red) and -10V (yellow) for the device with transmittance of 0.30.

in resonance wavelength is 0.18 nm, which corresponds to a change in the cavity temperature of $\sim 2\text{K}$ given the thermo-optic coefficient of silicon of $1.86 \times 10^{-4}/\text{K}$ [126]. In addition to thermo-optic detuning, the effect of two photon absorption (TPA) is also apparent from Fig. 5.7b, where the peak photocurrent is plotted against the absorbed optical power. Here, two regions can be identified. For low power operation, the photocurrent increases linearly with absorbed optical power and follows a line corresponding to the 7 mA/W responsivity. As the absorbed power increases beyond $20 \mu\text{W}$, a second component with a quadratic dependence becomes apparent which can be attributed to TPA [139, 140].

I have also investigated the effect of reverse bias on photocurrent and resonance wavelength. The optical power in the waveguide in this case was $55 \mu\text{W}$ with total optical loss of $25.3 \mu\text{W}$. Figure 5.7d shows the measured photocurrent as the reverse bias is increased from 0 V to -10 V. For 0 V to -2 V, the photocurrent shows a sharp increase due to the fast sweep-out of photo-generated carriers from the intrinsic region of the diode and then a further (less dramatic) increase from -2 V to -10 V. As shown in Fig. 5.7e, the responsivity also increases with reverse bias from 9.5 mA/W to 108 mA/W, with a corresponding increase in dark current from 0.5 nA to 9 nA. The effect of reverse bias on resonance wavelength is particularly interesting. In Fig. 5.7f, we can observe an initial blueshift in the resonance wavelength when the reverse bias is increased from 0 V to -2 V followed by a steady redshift for

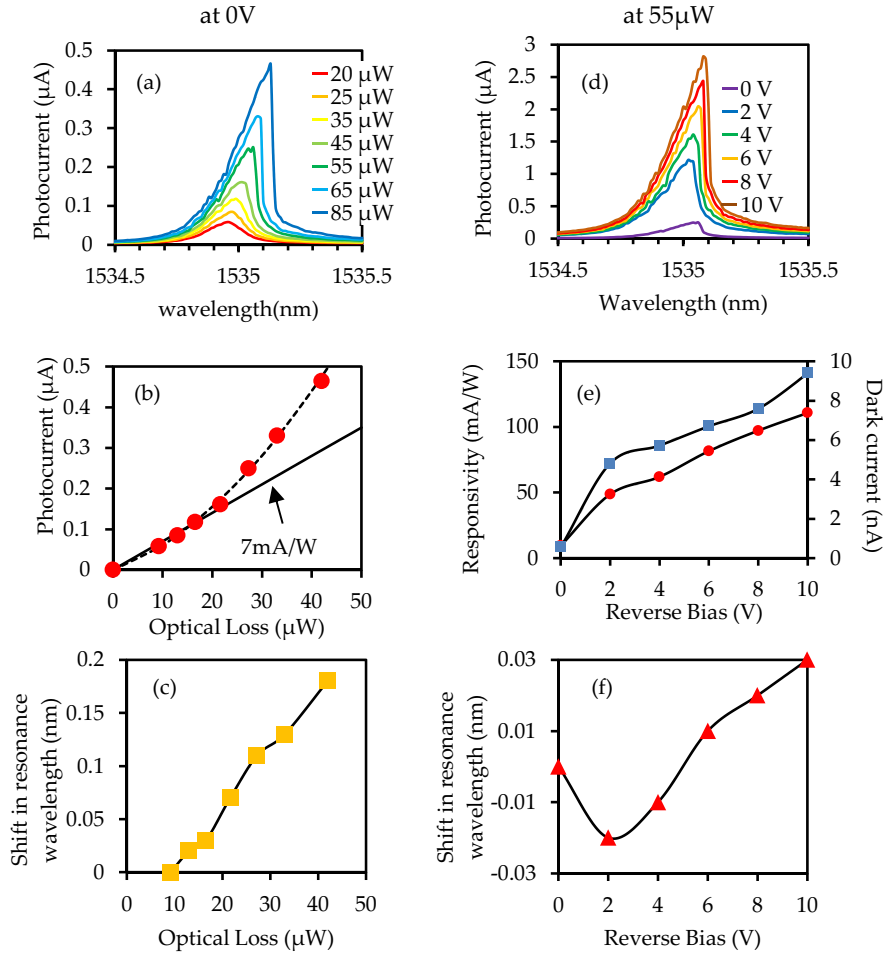


Figure 5.7 – (a) Measured photocurrent spectra for different input optical power at 0 V reverse bias. (b) Measured photocurrent peaks as the absorbed optical power increases. The solid line corresponds to a 7 mA/W responsivity and the dashed line shows the trend in photocurrent as the input power increases. (c) Shift in resonance wavelength as the absorbed optical power increases. (d) Measured photocurrent spectra for different applied reverse bias, when the input optical power is $55 \mu\text{W}$. (e) Measured responsivity (red circle) at resonance and dark current (blue square) as the reverse bias increases. (f) Shift in resonance wavelength as the applied reverse bias increases.

higher reverse voltage. For 0 V reverse bias, due to the lack of an external electric field, most of the photo-generated carriers recombine inside the intrinsic region and contribute to the rise in temperature of the “cold” cavity which causes a redshift of the resonance wavelength. As the reverse bias increases from 0 V to -2 V, more of the photo-generated carriers are swept away from the intrinsic region before they can recombine and the cavity temperature drops causing a relative blue shift in resonance wavelength. Further increases in reverse bias increase the photocurrent but cause Ohmic heating

due to the movement of photo-generated carriers, redshifting the resonance wavelength once more. Using the same calculation used in the previous section, we can estimate that a change in reverse bias of -8V increases the cavity temperature by 0.6 K.

5.5.2 Demultiplexing

In Chapter 4, I have demonstrated that the vertically coupled waveguide-cavity architecture enables the multiplexing of multiple channels without the need for additional wavelength selective components. Here I use the same principle to achieve wavelength demultiplexing. Due to the wavelength selective nature of our detector, only one specific wavelength channel will be detected. As a result, multiple detectors can be cascaded in series and coupled to the same waveguide. To demonstrate this functionality, I have cascaded two detectors to address two different wavelength channels, as shown in Fig. 5.8a. To achieve different resonance wavelengths for the detectors, the cavities were fine-tuned lithographically, similar to the process described in Chapter 4. Figure 5.8b shows the normalized optical transmission spectrum (in blue) of the system, with each dip in transmission corresponding to a cavity. Red and yellow (dashed) curves show the detected photocurrent response from the first and the second detectors, respectively.

5.6 Discussion

In summary, I have demonstrated wavelength selective photo-detection in deep level mediated silicon photodiodes. Due to the high optical confinement achievable in photonic crystal cavities, the device size was only $20 \mu m$. I have demonstrated a responsivity of $0.108 A/W$ at -10 V bias with 9.4 nA dark current. Additionally, vertically coupling to low refractive index waveguides provides very low insertion losses and access to powerful passive optical components. By cascading multiple cavities coupled to the same waveguide, a simple and elegant photo-detection scheme is realized that is the ideal counterpart to the modulator architecture discussed in Chapter 4.

The photodetector design presented here shares many similarities with previous work on defect-mediated detection in ring resonators [32, 92, 141]. While the Q-factor is similar in both cases, the finesse of the photonic crystal cavity is significantly higher. This provides a larger Free Spectral Range (i.e. the number of supported channels) for the same Q-factor and allows a smaller device reducing the capacitance, by over an order of magnitude, and thereby the power consumption of subsequent electronic amplifiers. Similar to the modulator design, by avoiding the use of spot size converters, grating couplers, AWGs or Echelle gratings, a significant reduction in the optical power budget is also possible, which is very promising for on-chip optical interconnects. This brings the effective responsivity (photo current/power from the optical fiber) of our photodiode much closer to that the III-V/germanium demultiplexed photodetection systems. Alternative to operating as a photodetector, the system could also be considered for monitoring light propa-

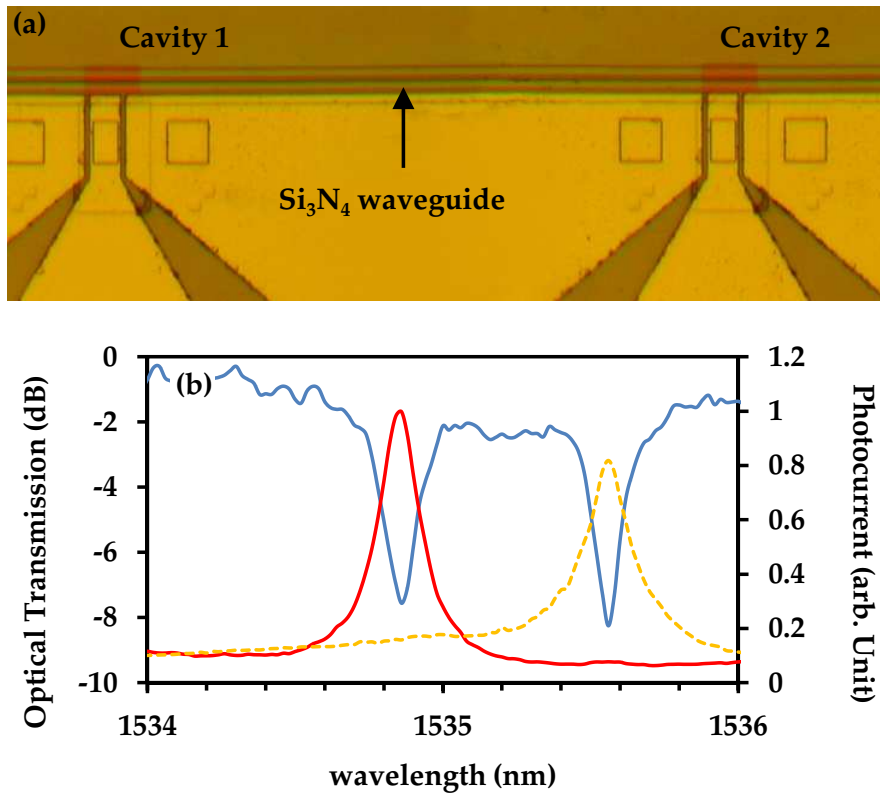


Figure 5.8 – (a) Top view of the cascaded photonic crystal cavity based detector set, where two cavities are coupled to a single silicon nitride waveguide. (b) Normalized transmission spectrum (blue) of the system and measured photocurrent from detector 1 (red) and detector 2 (yellow dashed).

gating in a dielectric waveguide, avoiding the need for tap-off and spot size converting structures.

In this demonstration, a large fraction of the coupled light is lost mainly due to free carrier absorption in the diode that does not contribute to the photocurrent. Based on the measured quality factors and the responsivity, around 57% of the total optical loss that arises from the defects contributes to the photocurrent, suggesting a room for further improvement. Several design optimizations can be implemented to improve the detection efficiency. The free carrier absorption could be reduced by reducing the electrical doping levels near the cavity region which will allow us to increase the defect concentration further. This can be achieved by increasing the gap between the doped regions. This, however, would affect the speed of the device. Another alternative is to use four level doping, i.e. p+pinn+, so that the optical mode sees less of the highly doped regions. Moreover, improvements in the junction layout and the use of sidewall passivation will also improve the extraction of photocarriers.

Chapter 6

Conclusions

6.1 Thesis summary

In this thesis, I have introduced and demonstrated a new architecture for optical interconnects that provides a common platform and offers extreme simplicity and efficiency. The architecture may be used in a wide range of applications, ranging from fiber-to-the-home to chip-to-chip links, possibly even enabling global on-chip interconnects. At the heart of the design is a highly efficient optical filter that is based on a low index bus waveguide vertically coupled to a photonic crystal cavity. Photonic crystal cavities provide the ultimate confinement of light both in time and space and consequently offer substantial savings in operating power, cost and footprint.

Getting light in and out of photonic crystal cavities is considerable challenge that has, so far, confined them to “hero” experiments conducted in a well-controlled laboratory environment. Our vertical coupling approach addresses this problem and offers a solution that has the potential to make photonic crystal cavities useful even in the field. This unique coupling scheme allows us to precisely control the light coupling efficiency between a dielectric bus waveguide and the cavity, i.e. to couple two optical modes that are located in two very dissimilar materials and hence increase the extinction ratio of the filter. In Chapter 3, I have demonstrated that an extinction ratio of more than 10 dB can be achieved with this technique. Placing the bus waveguide on top of the cavity makes it easy to independently optimize both the optical components, the waveguide and the cavity. I have demonstrated that by varying the width, thereby the effective index, of the bus waveguide, the coupling efficiency and hence the extinction ratio can be controlled. Equally, the coupling efficiency can also be controlled by optimizing the cavity structure. Moreover, the flexibility on the choice of the waveguide material permits us to reduce the insertion loss as well as the transmission loss. A fiber-to-fiber loss of less than 3 dB was demonstrated using a polymer waveguide. Ultimately, this may be reduced to ~ 1 dB [142]. Finally, this vertical coupling scheme allows us to cascade multiple photonic crystal cavities coupled to the same waveguide, thus suggesting its potential as a WDM component.

In Chapter 4, I have implemented this vertically coupled system to real-

ize a five channel WDM transmitter. Multiwavelength operation was demonstrated by operating all five channels (with 50 GHz channel spacing) simultaneously using a single comb laser, one of the first demonstrations of this kind. Due to the limitation imposed by the electrical design (carrier injection), the highest modulation speed measured was 1 Gbit/s. This, however, is not a fundamental limitation and can be improved by employing depletion-type modulation. Modulation speeds up to 60 Gbit/s have already been demonstrated with this technique in rib waveguide [62] and 40 Gbit/s speed has been demonstrated in photonic crystal waveguide [66]. In our devices, due to the ultra-small mode volume of the photonic crystal cavities, the required operating energy was very low; I have estimated a switching energy of only 1.6 fJ, which represents one of the lowest ever energies reported for silicon electro-optic modulators. In addition to the low switching energy, the large free spectral range (FSR) of single mode photonic crystal cavities can make this approach very scalable. Thus the combination of high scalability, low switching energy, small footprint and low insertion loss makes our architecture very suitable for dense WDM operation and has the potential for Tbit/s data transmission.

To highlight the advantages of our architecture, in Table 6.1 I make a comparison with other WDM designs reported in the literature. Based on the type of modulators used, we can categorize the WDM designs into two groups: resonant and non-resonant (broadband) approaches. There are a large number of options for non-resonant modulators and most of them are based on interference based technique (MZI) that require prohibitively large operating energies (in pJ/bit). For the purpose of comparison, we limit ourselves to the most energy efficient, namely the waveguide integrated germanium electro-absorption modulator (at 0.75 fJ/bit) [144]. Such a relatively broadband modulator may be combined with a range of demultiplexing/multiplexing elements in a WDM system. For an arrayed waveguide grating (AWG), used for multiplexing/demultiplexing, the channel number is given by the number of waveguides and the channel spacing is given by the interference order. In contrast, in resonator approaches, the number of channels scales with the finesse of the resonator ($FSR/\Delta\lambda_{FWHM}$) and the channel spacing is decided by the resonator quality factor. These considerations place limitations on the area and channel number of the various approaches and are clearly illustrated in the table. By virtue of its high FSR, the photonic crystal cavity can provide the greatest number of channels making it one of the most promising routes to high bandwidth optical links.

Finally in Chapter 5, I have demonstrated optical detection using the vertically coupled system. By creating crystal defects in a silicon pin junction, weak sub bandgap absorption was created. By using a high quality factor photonic crystal cavity, a responsivity of 0.108 A/W was experimentally realized with less than 10 nA of dark current. In a similar geometry as was used for the cascaded modulator design, we have also demonstrated a two channel WDM receiver by cascading two cavity detectors coupled to the same silicon nitride waveguide.

Type	Channel Spacing	FSR (nm)	Area/channel (μm^2)*	Maximum channels	Excess loss (dB)**	Switching energy (fJ)
Rings	0.6[81]	18[81], 19[143]	400	30	9[67], 11[85]	55[68]
Si ₃ N ₄ AWG[35]	0.8	12.8	300 000	16	14	
Si AWG[87]	0.8	74	12 000	46	10	3[144]
Echelle[145]	3	90	16 600	30	16	
Microdisks[146]	-	-	25	-	10	12
This approach	0.44	100+[94]	100	220+	6 (2.8)	1.6

Table 6.1 – A comparison of different low power WDM modulator techniques.

For the channel numbers and spacings, in order to show the full potential of the various systems, the best case numbers are taken from the respective papers. Microdisk modulators are a powerful option, intermediate between the ring resonators and photonic crystal cavities in terms of mode volume and FSR. However, to our knowledge, cascadeability has not yet been demonstrated.

*This is the area of each resonant component (with an allowance for trenches etc) or the total device area divided by the number of channels.

**Defined here as the sum of the coupling loss and the loss in the demux/mux elements. Losses in the modulator are generally in the 3-5dB range [85], but strongly depend on the extinction ratio and energy/bit values used thus making a comparison based on this number difficult. NB For the non-resonant approaches, this loss is calculated assuming both a demultiplexing and multiplexing element. Losses in interfacing between the demux/mux and the modulators are also ignored in this case.

The state of the art in germanium photodetectors is already very high with 1 A/W responsivities regularly reported. This, however, is reported in terms of the power received by the photodetectors rather than that coupled from the fiber. Therefore, when coupling losses (5.5 dB [85]) and wavelength selection (e.g. 3 dB for AWG [87]) are included, the true responsivity is clearly lower. By virtue of the efficient coupling to fiber (ultimately <1 dB) and wavelength selective nature (0 dB additional loss), the initial demonstration of our detector operation is therefore much closer to that of a germanium detector than the bare performance numbers suggest. An optimization of the defect implantation and coupling conditions will lead to further improvements in responsivity.

6.2 Future directions

Initial demonstrations of different components of the proposed optical interconnect architecture have already shown significant improvement over competing architectures in terms of power consumption, scalability and integration density. Nonetheless, a number of areas still remain for further investigation and improvement. In this section, I discuss some of the research plans that will be undertaken in the future.

6.2.1 Optimization of the filter response

In this work, the highest extinction ratio was realized for silicon nitride waveguides, whereas low insertion loss was demonstrated for polymer (ZEP) waveguides. By optimizing the photonic crystal cavity structure as well as the k-space matching conditions, high extinction ratio and low insertion loss can be achieved simultaneously. A key milestone would be to realize extinction ratio of ~ 20 dB with insertion loss below 1 dB. In order to achieve such performance, two different approaches will be implemented. In one approach, I will consider polymer waveguide based vertically coupled system. Polymer waveguides have the advantage of achieving low insertion loss even without any spot size converters, thus offering great design and fabrication simplicity. The low index contrast of polymer waveguides, however, limits the coupling efficiency and as a result, the extinction ratio of the overall system is low. As we saw in Chapter 3, since the high intensity point on the k-space distribution of the polymer waveguide sits very close to the light line (leaky region) of the silica cladding, the overlap intensity with an unmodified cavity k-space is small. The overlap intensity can be improved by modifying the cavity k-space in such a way that more intensity appears near the light line of silica cladding. One way to modify the k-space distribution of the cavity is by stretching the background photonic crystal lattice as demonstrated in Section 3.5.5. In another approach, I will explore the possibility of using cantilever coupling technique [54] to reduce the insertion loss in silicon nitride waveguides. From an integration point of view, silicon nitride is a better candidate for waveguide material than polymer. Silicon nitride also

offers better extinction ratio, but insertion had been an issue in the current demonstration.

For most of the experimental demonstrations presented in this thesis, I have used a dispersion adapted (DA) cavity design, because of its large fabrication tolerance and better mode overlap with the polymer and silicon nitride bus waveguides. This type of cavity, however, is not ideal for demonstrating scalability and a large channel count, because it only has a small FSR. In the future, other types of single mode cavity designs, such as the linewidth modulated cavity, the heterostructure cavity, and the hexapole cavity [147], all of which offer higher FSR, will be considered in detail. Both linewidth modulated cavity and heterostructure cavity designs can achieve high quality factor even with oxide cladding. We have already demonstrated quality factor of 120,000 with oxide cladded linewidth modulated cavity. High quality factor heterostructure cavity with oxide cladding has also been demonstrated elsewhere [110]. The hexapole cavity is particularly interesting from design point of view, due to the six-fold symmetry of its k-space distribution. Such symmetry would allow more possibilities for coupling configuration in comparison to photonic crystal waveguide based cavity designs. However, the viability of this cavity design with oxide cladding still needs to be explored.

6.2.2 Optimization of the modulator design

For fabrication simplicity and a quick turnaround, I used injection type modulation. As a result, the modulation speed was limited to only 1Gbit/s. To overcome this limitation, the next step will be to consider depletion-type modulation. From our current results we have estimated that a change in carrier density of $5 \times 10^{15} \text{ cm}^{-3}$ is sufficient to achieve 3 dB extinction ratio. This carrier density change can easily be achieved by reverse biasing a pn diode. Hence, in future modulator designs, the pin diode will be replaced by a pn diode. Here I will consider two different diode configurations, as shown in Fig. 6.1. The first design is a simple pn diode, where the depletion region is designed to coincide with the cavity axis. The drawback of this design is that it is less tolerant to misalignment and the optical mode overlap with the depleted junction is smaller. For the second design I will consider an interleaved junction. As the interleaved pn junctions are oriented crossing the cavity region, the overlap of the depletion regions and the optical mode of the cavity is insensitive to the location of the pn junctions, which enables much higher misalignment tolerance for the fabrication process. A modulator design layout containing these modifications has already been sent to IME, Singapore, for fabrication, within the framework of UK Silicon Photonics.

6.2.3 Thermal stability

Sensitivity to thermal fluctuations is the primary drawback of resonant approaches, so active compensation is required, which is typically done thermally [119]. However, the extreme confinement of light in photonic crystal cavities provides another option, namely to exploit nonlinearity; the strong light intensity in the cavity enhances two photon absorption. Together with

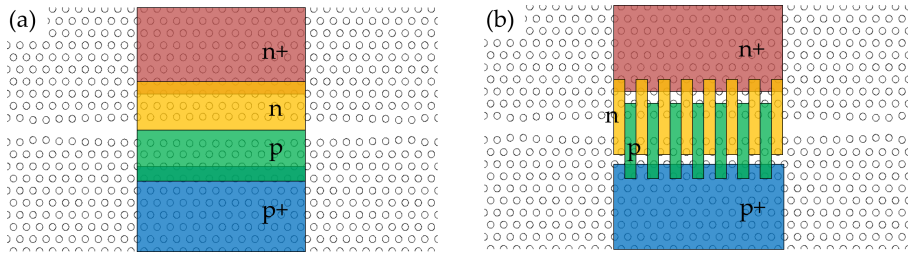


Figure 6.1 – Electrical design for the depletion type modulator (a) simple pn junction, (b) interleaved pn junction

the resulting free carriers, two photon absorption causes absorption; the resulting heating effect shifts the original resonance (known as self-tuning) until it reaches a steady state. At this point, there is a degree of temperature stability, because detuning reduces the self-heating effect, so the cavity tracks the emission line. The process of thermal stability using self-tuning is described in Fig. 6.2. Initial experiments suggest that the cavity can be stabilized within a range of approximately 5°C for a coupled laser power of $50\text{-}100\ \mu\text{W}$. This method is also compatible with electro-optic tuning, as the refractive index change for electro-optic modulation occurs on a much smaller time scale (in GHz) than the thermo-optic effect, thus it does not break the steady state condition. The use of 8b/10b or Manchester encoding would be helpful for the implementation of this method to avoid any long stream of “0” bits to prevent the cavity from cooling down.

6.2.4 Optimization of the detector design

For detectors, the defect creation approach will be further optimized and a four level doping strategy, i.e. p+pinn+, will be implemented to reduce free carrier absorption and to increase defect absorption and hence realize higher responsivity. Additionally, alternative approaches such as polycrystalline silicon will be studied. There is significant absorption at the grain boundaries and the temperature stability is superior for polysilicon in comparison to defect implanted, where the defect tends to disappear at temperature above 300°C . With a propagation loss of $6\ \text{dB/cm}$ (corresponding to a quality factor of 100,000) [32], high wavelength selectivity and photodetection can be achieved simultaneously in a photonic crystal cavity. Our coupling approach also avoids the downside of using polycrystalline silicon, namely increased absorption in passive waveguides, because all the passive functions are performed in the dielectric bus waveguide.

Detector designs containing four level doping have been included in the mask layout sent to IME. Along with individual modulator and detector devices, complete on-chip optical link (five channels) has also been included in the mask.

Due to the small footprint, the capacitance of photonic crystal cavity based photodiode is in the atto-Farad regime [139]. This small capacitance opens the door to super-efficient receivers. As highlighted in [132], for a given charge created by the incident light, the smaller the capacitance, the

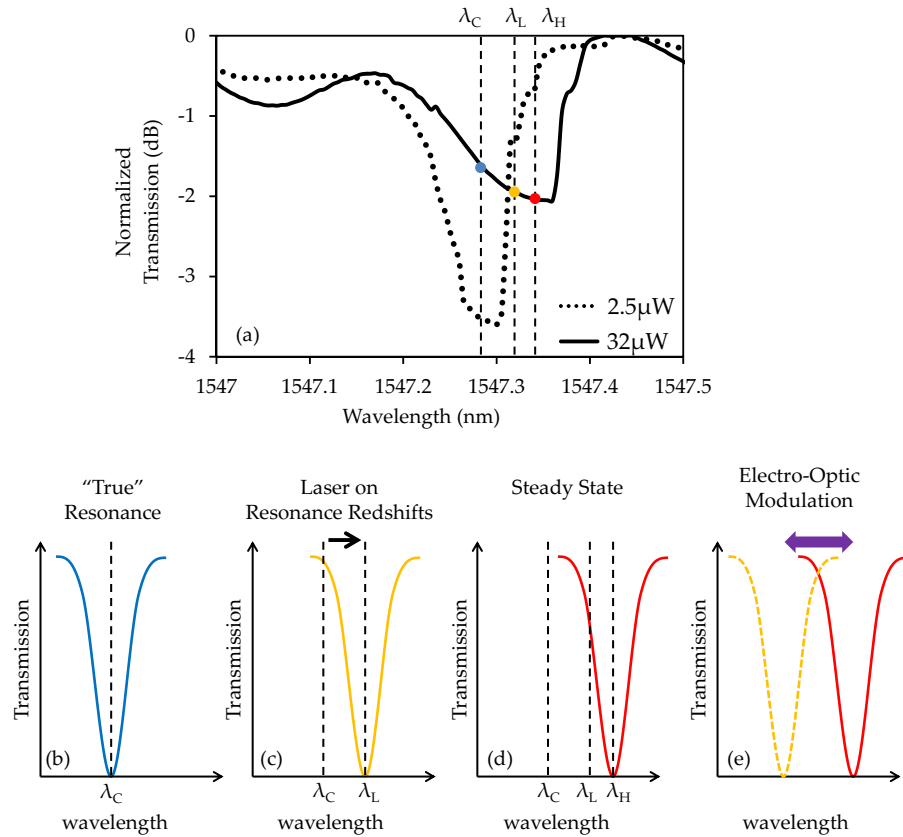


Figure 6.2 – (a) Transmission spectra of a vertically coupled system for different input optical power taken under wavelength upsweeping condition using a tunable laser. Dotted line shows the transmission spectrum for a “cold” cavity, i.e. the input power is small. Solid curve shows the transmission spectra for a “hot” cavity. Relatively large and asymmetric transmission dip in case of a hot cavity is an artifact of self-tuning effect. Process of temperature stability using self-tuning effect: (b) When the laser is set to a wavelength slightly longer than λ_C , see (c), a small amount of light is coupled into the cavity, resulting in a small amount of TPA and FCA. This redshifts the resonance (λ_H , the “hot” resonance) increasing the coupling of light into the cavity, resulting in further redshifting of the resonance. This continues until the resonance matches the laser wavelength (λ_L), see (d) and TPA and FCA are at a maximum. The resonance continues to redshift but now the amount of TPA and FCA starts to decrease as less and less light is coupled to the cavity. The system will quickly reach a steady state, with the heat produced by TPA and FCA matching the heat dissipated from the cavity. Should the resonance be red shifted further (due to change in temperature of the cavity environment), the heating effects will reduce and the cavity will experience a net cooling returning to the steady state. The electro-optic modulation, see (e), which happens at a nanosecond time scale, will not affect this steady state.

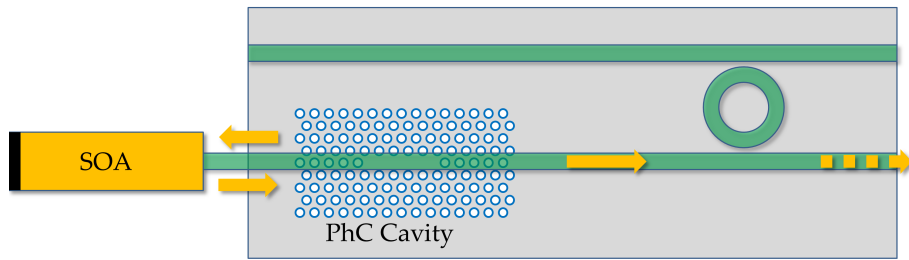


Figure 6.3 – Schematic diagram showing the laser built around a reflective SOA and a narrow line-width Photonic Crystal reflector. A passive ring resonator is added on the output waveguide to enable direct modulation.

larger the output voltage. This favorable scaling potentially allows us to drive a transistor directly, the so-called “receiverless” mode, thus reducing or even avoiding the use of electronic amplifying circuits and their power consumption. In the future, I plan to study this receiverless configuration and to build examples of circuits, using a silicon or poly-silicon resistor that will be placed in series with the photodiode in order to generate an output voltage. The capacitance of the total circuit determines the speed and a study will be made on the tradeoffs between speed and output voltage.

6.2.5 Tunable Lasers and directly modulated laser

Another opportunity offered by our architecture is to build a wavelength tunable laser. Such a device can be realized by combining a semiconductor optical amplifier (SOA) and our vertically coupled system, as shown in Fig. 6.3. In this configuration, the optical gain will be provided by a reflective SOA and the photonic crystal cavity will naturally give narrow linewidth reflection, ideal for a laser mirror. This concept is similar to that of [148], but the simplicity and efficiency of our system should enable much superior performance. With optimization, the large core polymer waveguide will provide on-resonance reflection back into the amplifier of greater than 50%. This locks the lasing wavelength to a component of the silicon chip, thereby eliminating the need for matching the two. By optimizing the SOA for modest gain at low currents and the waveguide dimensions for coupling, very efficient operation can be attained. Calculations suggest that sub-10 mW threshold power consumption and 0.1 W/A slope efficiencies can be achieved.

This platform can then be used to realize an entirely new type of directly modulated laser. Normally, the laser gain chip is switched on and off to signify “1” and “0” states. Instead, we will tune photonic crystal reflector at high speed. As the resonance moves, so will the filter reflection and the laser wavelength. By placing a second, fixed filter (e.g. a passive ring resonator) in the output path of the laser light the beam will either be passed the communication link (a ‘1’) or the beam will be passed to a beam dump (a ‘0’). We can thus achieve an encoding mechanism that consumes very little energy even at high data rates and produces very little chirp.

Ultimately, all these techniques will be combined to demonstrate a com-

plete optical interlink aiming to achieve on-chip power consumption of 50 fJ/bit and 1 pJ/bit for the complete link.

Bibliography

- [1] M. McLuhan, *The Gutenberg Galaxy The Making of Typographic Man*. University of Toronto Press, 1962.
- [2] M. G. Institute, “Internet matters the nets sweeping impact on growth job and prosperity,” May 2011. [Online]. Available: <http://www.mckinsey.com/>
- [3] M. marketing group, “Internet world stats,” February 2013. [Online]. Available: <http://www.internetworldstats.com/stats.htm>
- [4] “Twentieth session of the united nations human rights council,” 2012.
- [5] BBC, “Carbon cost of google revealed,” January 2009. [Online]. Available: <http://news.bbc.co.uk/2/hi/7823387.stm>
- [6] M. Asghari and A. V. Krishnamoorthy, “Energy efficient communication,” *Nature Photonics*, vol. 5, pp. 268–270, 2011.
- [7] G. E. Moore, “Cramming more components onto integrated circuits,” *Electronics*, vol. 38, pp. 114–117, 1965.
- [8] ITRS, “International roadmap for semiconductors.” [Online]. Available: <http://www.itrs.net/>
- [9] P. Moon, V. Chikarmane, K. Fischer, R. Grover, T. A. Ibrahim, D. Ingerly, K. J. Lee, C. Litteken, T. Mule, and S. Williams, “Process and electrical results for the on die interconnect stack for intels 45nm process generation,” *Intel Technology Journal*, vol. 12, pp. 87–92, 2008.
- [10] ITRS, “International roadmap for semiconductors,” 2005. [Online]. Available: <http://www.itrs.net/>
- [11] N. Magen, A. Kolodny, U. Weiser, and N. Shamir, “Interconnect power dissipation in a microprocessor,” *Proceedings of the 2004 international workshop on System level interconnect prediction*, pp. 7–13, 2004.
- [12] J. W. Goodman, F. J. Leonberger, S. Y. Kung, and R. A. Athale, “Optical interconnections for VLSI systems,” *Proceedings of the IEEE*, vol. 72, pp. 850–866, 1984.
- [13] R. Ho, K. W. Mai, and M. A. Horowitz, “The future of wires,” *Proceedings of the IEEE*, vol. 89, pp. 490–504, 2001.

- [14] D. A. B. Miller and H. M. Ozaktas, "Limit to the bit rate capacity of electrical interconnects from the aspect ratio of the system architecture," *Journal of Parallel Distributed Computing*, vol. 41, pp. 42–52, 1997.
- [15] D. A. B. Miller, "Rationale and challenges for optical interconnects to electronic chips," *Proceedings of the IEEE*, vol. 88, pp. 728–749, 2000.
- [16] —, "Device requirements for optical interconnects to silicon chips," *Proceedings of the IEEE*, vol. 97, pp. 1166–1185, 2009.
- [17] V. Alwayn, *Fiber Optic Technologies*. Cisco Press, 2004.
- [18] R. G. Beausoleil, P. J. Kuekes, G. S. Snider, S.-Y. Wang, and R. S. Williams, "Nanoelectronic and nanophotonic interconnect," *Proceedings of IEEE*, vol. 96, pp. 230–247, 2007.
- [19] R. A. Soref and B. R. Bennett, "Kramers Kronig analysis of electro optical switching in silicon," *Proceedings of SPIE*, vol. 704, pp. 32–37, 1986.
- [20] R. A. Soref and J. P. Lorenzo, "Single crystal silicon a new material for 1.3 and 1.6 um integrated optical components," *Electronics Letters*, vol. 21, pp. 953–954, 1985.
- [21] M. Bruel, "Silicon on insulator material technology," *Electronics Letters*, vol. 31, pp. 1201–1202, 1995.
- [22] C. Gunn, "CMOS photonics SOI learns a new trick," *Proceedings of IEEE*, pp. 7–13, 2005.
- [23] C. Gunn, A. Narasimha, B. Analui, Y. Liang, and T. J. Sleboda, "A 40Gb silicon photonics transceiver," *Proceedings of SPIE*, pp. 64 770N–8, 2007.
- [24] A. Shacham, K. Bergman, and L. P. Carloni, "On the design of a photonic network on chip," *Proceedings of the First International Symposium on Networks on Chip*, pp. 53–64, 2007.
- [25] D. Vantrease, R. Schreiber, M. Monchiero, M. McLaren, N. P. Jouppi, M. Fiorentino, A. Davis, N. Binkert, R. G. Beausoleil, and J. H. Ahn, "Corona system implications of emerging nanophotonic technology," *ACM SIGARCH Computer Architecture News*, vol. 36, pp. 153–164, 2008.
- [26] Y. Pan, P. Kumar, J. Kim, G. Memik, Y. Zhang, and A. Choudhary, "Firefly illuminating future network on chip with nanophotonics," *ACM SIGARCH Computer Architecture News*, vol. 37, pp. 429–440, 2009.
- [27] M. J. Cianchetti, J. C. Kerekes, and D. H. Albonesi, "Phastlane a rapid transit optical routing network," *ACM SIGARCH Computer Architecture News*, vol. 37, pp. 441–450, 2009.

-
- [28] M. Petracca, B. G. Lee, K. Bergman, and L. P. Carloni, "Design exploration of optical interconnection networks for chip multiprocessors," *16th IEEE Symposium on High Performance Interconnects*, pp. 31–40, 2008.
- [29] T. K. Liang and H. K. Tsang, "Role of free carriers from two photon absorption in raman amplification in silicon on insulator waveguides," *Applied Physics Letters*, vol. 84, pp. 2745–2747, 2004.
- [30] A. Biberman, K. Preston, G. Hendry, N. Sherwood-Droz, J. Chan, J. S. Levy, M. Lipson, and K. Bergman, "Photonic network on chip architectures using multilayer deposited silicon materials for high performance chip multiprocessors," *Journal of Emerging Technology in Computing Systems*, vol. 7, pp. 7:1–7:25, 2011.
- [31] N. Sherwood-Droz and M. Lipson, "Scalable 3D dense integration of photonics on bulk silicon," *Optics Express*, vol. 19, pp. 17 758–17 765, 2011.
- [32] K. Preston, Y. H. D. Lee, M. Zhang, and M. Lipson, "Waveguide integrated telecom wavelength photodiode in deposited silicon," *Optics Letters*, vol. 36, pp. 52–54, 2011.
- [33] K. Preston, S. Manipatruni, A. Gondarenko, C. B. Poitras, and M. Lipson, "Deposited silicon high speed integrated electro optic modulator," *Optics Express*, vol. 17, pp. 5118–5124, 2009.
- [34] S. Zhu, G. Q. Lo, and D. L. Kwong, "Low loss amorphous silicon wire waveguide for integrated photonics effect of fabrication process and the thermal stability," *Optics Express*, vol. 18, pp. 25 283–25 291, 2010.
- [35] L. Chen, C. R. Doerr, P. Dong, and Y.-K. Chen, "Monolithic silicon chip with 10 modulator channels at 25 Gbps and 100 GHz spacing," *Optics Express*, vol. 19, pp. B946–B951, 2011.
- [36] J. N. Milgram, J. Wojcik, P. Mascher, and A. P. Knights, "Optically pumped Si nanocrystal emitter integrated with low loss silicon nitride waveguides," *Optics Express*, vol. 15, pp. 14 679–14 688, 2007.
- [37] K. Ikeda, R. E. Saperstein, N. Alic, and Y. Fainman, "Thermal and Kerr nonlinear properties of plasma deposited silicon nitride silicon dioxide waveguides," *Optics Express*, vol. 16, pp. 12 987–12 994, 2008.
- [38] J. Michel, J. Liu, and L. C. Kimerling, "High performance Ge on Si photodetectors," *Nature Photonics*, vol. 4, pp. 527–534, 2010.
- [39] G. Treyz, "Silicon mach zehnder waveguide interferometer operating at 1.3 μm ," *Electronics Letters*, vol. 27, pp. 118–120, 1991.
- [40] G. T. Reed, *Optical Interconnects the Silicon Approach*, L. Pavesi and G. Guillot, Eds. Springer, 2006.

- [41] M. Gnan, S. Thomas, D. S. Macintyre, R. M. D. L. Rue, and M. Soref, "Fabrication of low loss photonics wires in silicon on insulator using hydrogen silsesquioxane electron beam resist," *Electronics Letters*, vol. 44, pp. 115–116, 2008.
- [42] F. Y. Gardes, G. T. Reed, A. P. Knights, G. Mashanovich, P. E. Jessop, L. Rowe, S. McFaul, D. Bruce, and N. G. Tarr, "Sub micron optical waveguides for silicon photonics formed via the local oxidation of silicon (LOCOS)," *International Society for Optics and Photonics*, p. 68980R, 2008.
- [43] J. Cardenas, C. B. Poitras, J. T. Robinson, K. Preston, L. Chen, and M. Lipson, "Low loss etchless silicon photonic waveguides," *Optics Express*, vol. 17, pp. 4752–4757, 2009.
- [44] M. P. Nezhad, O. Bondarenko, M. Khajavikhan, A. Simic, and Y. Fainman, "Etch free low loss silicon waveguides using hydrogen silsesquioxane oxidation masks," *Optics Express*, vol. 19, pp. 18 827–18 832, 2011.
- [45] P. Cardile, G. Franzo, R. L. Savio, M. Galli, T. F. Krauss, F. Priolo, and L. O. Faolain, "Electrical conduction and optical properties of doped silicon on insulator photonic crystals," *Applied Physics Letters*, vol. 98, pp. 203 506–203 506–3, 2011.
- [46] M. J. Shaw, J. Guo, G. A. Vawter, S. Habermehl, and C. T. Sullivan, "Fabrication techniques for low loss silicon nitride waveguides," *International Society for Optics and Photonics*, pp. 109–118, 2005.
- [47] A. Gondarenko, J. S. Levy, and M. Lipson, "High confinement micron scale silicon nitride high Q ring resonator," *Optics Express*, vol. 17, pp. 11 366–11 370, 2009.
- [48] T. W. Ang, G. T. Reed, A. Vonsovici, A. G. R. Evans, P. R. Routley, and M. R. Josey, "Highly efficient unibond silicon on insulator blazed grating couplers," *Applied Physics Letters*, vol. 77, pp. 4214–4216, 2000.
- [49] D. Taillaert, W. Bogaerts, P. Bienstman, T. F. Krauss, P. V. Daele, I. Moerman, S. Verstuyft, K. D. Mesel, and R. Baets, "An out of plane grating coupler for efficient butt coupling between compact planar waveguides and single mode fibers," *IEEE Journal of Quantum Electronics*, vol. 38, pp. 949–955, 2002.
- [50] P. Cheben, S. Janz, D.-X. Xu, B. Lamontagne, A. Delage, and S. Tanev, "A broad band waveguide grating coupler with a subwavelength grating mirror," *IEEE Photonics Technology Letters*, vol. 18, pp. 13–15, 2006.
- [51] C. Gunn, "10Gb/s CMOS photonics technology," *Proceedings of SPIE*, vol. 6125, p. 612501, 2006.

-
- [52] G. Maire, L. Vivien, G. Sattler, A. Kazmierczak, B. Sanchez, K. B. Gylfason, and A. Griol, "High efficiency silicon nitride surface grating couplers," *Optics Express*, vol. 16, pp. 328–333, 2008.
- [53] T. Shoji, T. Tsuchizawa, T. Watanabe, K. Yamada, and H. Morita, "Low loss mode size converter from 0.3 μm square Si wire waveguides to singlemode fibres," *Optics Express*, vol. 18, pp. 21 519–21 533, 2010.
- [54] L. Chen, C. R. Doerr, Y.-K. Chen, and T.-Y. Liow, "Low loss and broadband cantilever couplers between standard cleaved fibers and high index contrast Si₃N₄ or Si waveguides," *IEEE Photonics Technology Letters*, vol. 22, pp. 1744–1746, 2010.
- [55] G. V. Treyz, P. G. May, and J. M. Halbout, "Silicon machzehnder waveguide interferometers based on the plasma dispersion effect," *Applied Physics Letters*, vol. 59, pp. 771–773, 1991.
- [56] A. Liu, R. Jones, L. Liao, D. Samara-Rubio, D. Rubin, O. Cohen, R. Nicolaescu, and M. Paniccia, "A high speed silicon optical modulator based on a metal oxide semiconductor capacitor," *Nature*, vol. 427, pp. 615–618, 2004.
- [57] F. Y. Gardes, G. T. Reed, and N. Emerson, "A sub micron depletion type photonic modulator in silicon on insulator," *Optics Express*, vol. 13, pp. 8845–8854, 2005.
- [58] L. Liao, A. Liu, D. Rubin, J. Basak, Y. Chetrit, H. Nguyen, R. Cohen, N. Izhaky, and M. Paniccia, "40 Gbit/s silicon optical modulator for highspeed applications," *IEEE Electronics Letters*, vol. 43, pp. 1196–1197, 2007.
- [59] D. J. Thomson, F. Y. Gardes, Y. Hu, G. Mashanovich, M. Fournier, P. Grosse, J. M. Fedeli, and G. T. Reed, "High contrast 40Gbit/s optical modulation in silicon," *Optics Express*, vol. 19, pp. 11 507–11 516, 2011.
- [60] D. J. Thomson, F. Y. Gardes, J.-M. Fedeli, S. Zlatanovic, Y. Hu, B. P. P. Kuo, E. Myslivets, N. Alic, S. Radic, G. Z. Mashanovich, and G. T. Reed, "50 Gb/s silicon optical modulator," *IEEE Photonics Technology Letters*, vol. 24, pp. 234–236, 2012.
- [61] P. Dong, L. Chen, and Y.-K. Chen, "High speed low voltage single drive push pull silicon Mach Zehnder modulators," *Optics Express*, vol. 20, pp. 6163–6169, 2012.
- [62] X. Xiao, X. L. H. Xu, Z. Li, T. Chu, Y. Yu, and J. Yu, "High-speed, low-loss silicon machzehnder modulators with doping optimization," *Optics Express*, vol. 21, pp. 4116–4125, 2013.
- [63] S. Schulz, L. OFaolain, D. M. Beggs, T. P. White, A. Melloni, and T. F. Krauss, "Dispersion engineered slow light in photonic crystals a comparison," *Journal of Optics*, vol. 12, p. 104004, 2010.

- [64] Y. Jiang, W. Jiang, L. Gu, X. Chen, and R. T. Chen, "80 micron interaction length silicon photonic crystal waveguide modulator," *Applied Physics Letters*, vol. 87, p. 221105, 2005.
- [65] H. C. Nguyen, Y. Sakai, M. Shinkawa, N. Ishikura, and T. Baba, "10 Gb/s operation of photonic crystal silicon optical modulators," *Optics Express*, vol. 19, pp. 13 000–13 007, 2011.
- [66] H. C. Nguyen, S. Hashimoto, M. Shinkawa, and T. Baba, "Compact and fast photonic crystal silicon optical modulators," *Optics Express*, vol. 20, pp. 22 465–22 474, 2012.
- [67] Q. Xu, B. Schmidt, S. Pradhan, and M. Lipson, "Micrometre scale silicon electro optic modulator," *Nature*, vol. 435, pp. 325–327, 2005.
- [68] L. Chen, K. Preston, S. Manipatruni, and M. Lipson, "Integrated GHz silicon photonic interconnect with micrometer scale modulators and detectors," *Optics Express*, vol. 17, pp. 5248–52 556, 2009.
- [69] F. Y. Gardes, A. Brimont, P. Sanchis, G. Rasigade, D. Marris-Morini, L. O'Faolain, and F. Dong, "High speed modulation of a compact silicon ring resonator based on a reverse biased pn diode," *Optics Express*, vol. 17, pp. 21 986–21 991, 2009.
- [70] P. Dong, S. Liao, H. Liang, W. Qian, X. Wang, R. Shafiqi, D. Feng, G. Li, X. Zheng, A. V. Krishnamoorthy, and M. Asghari, "High speed and compact silicon modulator based on a racetrack resonator with a 1 V drive voltage," *Optics Letters*, vol. 35, pp. 3246–3248, 2010.
- [71] P. Dong, S. Liao, D. Feng, H. Liang, D. Zheng, R. Shafiqi, and C.-C. Kung, "Low V_{pp} ultralow energy compact high speed silicon electro optic modulator," *Optics Express*, vol. 17, pp. 22 484–22 490, 2009.
- [72] T. Tanabe, K. Nishiguchi, E. Kuramochi, and M. Notomi, "Low power and fast electro optic silicon modulator with lateral pin embedded photonic crystal nanocavity," *Optics Express*, vol. 17, pp. 22 505–22 513, 2009.
- [73] E. Kuramochi, M. Notomi, S. Mitsugi, A. Shinya, T. Tanabe, and T. Watanabe, "Ultrahigh Q photonic crystal nanocavities realized by the local width modulation of a line defect," *Applied Physics Letters*, vol. 88, p. 041112, 2006.
- [74] B.-S. Song, T. Nagashima, T. Asano, and S. Noda, "Resonant wavelength control of nanocavities by nanometer scaled adjustment of two dimensional photonic crystal slab structures," *IEEE Photonics Technology Letters*, vol. 2008, pp. 532–534, 2008.
- [75] L. Vivien, M. Rouviere, J.-M. Fedeli, D. Marris-Morini, J. F. Damlencourt, J. Mangeney, P. Crozat, L. E. Melhaoui, E. Cassan, X. L. Roux, D. Pascal, and S. Laval, "High speed and high responsivity germanium

- photodetector integrated in a silicon on insulator microwaveguide,” *Optics Express*, vol. 15, pp. 9843–9848, 2007.
- [76] L. Vivien, J. Osmond, J.-M. Fedeli, D. Marris-Morini, P. Crozat, J.-F. Damlencourt, E. Cassan, Y. Lecunff, and S. Laval, “42 GHz pin germanium photodetector integrated in a silicon on insulator waveguide,” *Optics Express*, vol. 17, pp. 6252–6257, 2009.
- [77] L. Chen and M. Lipson, “Ultra low capacitance and high speed germanium photodetectors on silicon,” *Optics Express*, vol. 17, pp. 7901–7906, 2009.
- [78] T. Yin, R. Cohen, M. M. Morse, G. Sarid, Y. Chetrit, D. Rubin, and M. J. Paniccia, “31 GHz Ge nip waveguide photodetectors on silicon on insulator substrate,” *Optics Express*, vol. 21, pp. 13 965–13 971., 2007.
- [79] J. D. B. Bradley, P. E. Jessop, and A. P. Knights, “Silicon waveguide integrated optical power monitor with enhanced sensitivity at 1550 nm,” *Applied Physics Letters*, vol. 86, p. 241103, 2005.
- [80] M. W. Geis, S. J. Spector, M. E. Grein, J. U. Yoon, D. M. Lennon, and T. M. Lyszczarz, “Silicon waveguide infrared photodiodes with 35 GHz bandwidth and phototransistors with 50 AW-1 response,” *Optics Express*, vol. 17, pp. 5193–5204, 2009.
- [81] Q. Xu, B. Schmidt, J. Shakya, and M. Lipson, “Cascaded silicon microring modulators for WDM optical interconnection,” *Optics Express*, vol. 14, pp. 9431–9436, 2006.
- [82] D. Kucharski, S. Abdalla, B. Analui, C. Bradbury, P. D. Dobbelaere, D. Foltz, S. Gloeckner, D. Guckenberger, M. Harrison, S. Jackson, M. Mack, G. Masini, A. Mekis, A. Narasimha, M. Peterson, T. Pinguet, S. Sahni, W. Wang, B. Welch, and J. Witzens, “40Gb/s optical active cable using monolithic transceivers implemented in silicon photonics enabled 0.13 um SOI CMOS technology,” *Hot Chips*, vol. 21, 2009.
- [83] M. Asghari, *IEEE Photonics Society Annual meeting*, 2012.
- [84] S. Ren, Y. Rong, S. A. Claussen, R. K. Schaevitz, T. I. Kamins, J. S. Harris, and D. A. B. Miller, “Ge SiGe quantum well waveguide modulator monolithically integrated with SOI waveguides,” *IEEE Photonics Technology Letters*, vol. 24, pp. 461–463, 2012.
- [85] X. Zheng, Y. Luo, J. Lexau, F. Liu, G. Li, H. D. Thacker, I. Shubin, J. Yao, R. Ho, and J. E. C. A. V. Krishnamoorthy, “2 pJ/bit onchip 10Gb/s digital CMOS silicon photonic link,” *Photonics Technology Letters*, vol. 24, pp. 1260–1262, 2012.
- [86] T. Pinguet, B. Analui, G. Masini, V. Sadagopan, and S. Gloeckner, “40 Gbps monolithically integrated transceivers in CMOS photonics,” *Proceedings of SPIE*, pp. 689 805–689 805, 2008.

- [87] Q. Fang, T.-Y. Liow, J. F. Song, K. W. Ang, M. B. Yu, G. Q. Lo, and D.-L. Kwong, "WDM multichannel silicon photonic receiver with 320 Gbps data transmission capability," *Optics Express*, vol. 18, pp. 5106–5113, 2010.
- [88] R. G. Beausoleil, J. Ahn, N. Binkert, A. Davis, D. Fattal, M. Fiorentino, N. P. Jouppi, M. McLaren, C. M. Santori, R. S. Schreiber, S. M. Spillane, D. Vantrease, and Q. Xu, "A nanophotonic interconnect for high performance many core computation," *16th IEEE Symposium on High Performance Interconnects*, pp. 182–189, 2008.
- [89] A. Kovsh, A. Gubenko, I. Krestnikov, D. Livshits, S. Mikhlin, J. Weimert, L. West, G. Wojcik, D. Yin, C. Bornholdt, N. Grote, M. Maximov, and A. Zhukov, "Quantum dot comb laser as efficient light source for silicon photonics," *Proceedings of SPIE*, vol. 7230, p. 72300M, 2009.
- [90] D. F. Kyser and N. S. Viswanathan, "Monte Carlo simulation of spatially distributed beams in electron-beam lithography," *Journal of Vacuum Science and Technology*, vol. 12, pp. 1305–1308, 1975.
- [91] M. Qiu, "Vertically coupled photonic crystal optical filters," *Optics Letters*, vol. 30, p. 1476, 2005.
- [92] J. K. Doylend, P. E. Jessop, and A. P. Knights, "Silicon photonic resonator enhanced defect mediated photodiode for sub bandgap detection," *Optics Express*, vol. 18, pp. 14671–14678, 2010.
- [93] N. Sherwood-Droz, H. Wang, L. Chen, B. G. Lee, A. Biberman, K. Bergman, and M. Lipson, "Optical 4x4 hitless silicon router for optical networks on chip," *Optics Express*, vol. 16, pp. 15915–15922, 2008.
- [94] M. Notomi, "Manipulating light with strongly modulated photonic crystals," *Report on Progress in Physics*, vol. 73, p. 096501, 2010.
- [95] B.-S. Song, S. Noda, T. Asano, and Y. Akahane, "Ultra high Q photonic double heterostructure nanocavity," *Nature Material*, vol. 4, pp. 207–210, 2005.
- [96] K. Welna, S. L. Portalupi, M. Galli, L. O'Faolain, and T. F. Krauss, "Novel dispersion adapted photonic crystal cavity with improved disorder stability," *IEEE Journal of Quantum Electronics*, vol. 48, p. 1177, 2012.
- [97] L. Rayleigh, "On the remarkable phenomenon of crystalline reflexion described by Prof Stokes," *Philosophical Magazine*, vol. 26, pp. 256–265, 1888.
- [98] M. Born and E. Wolf, *Principles of Optics*, 4th ed. Pergamon Press, 1970.

-
- [99] E. Yablonovitch, “Inhibited spontaneous emission in solid state physics and electronics,” *Physical Review Letters*, vol. 58, pp. 2059–2062, 1987.
- [100] J. D. Joannopoulos, S. G. Johnson, J. N. Winn, and R. D. Meade, *Photonic Crystals Molding the Flow of Light*, 2nd ed. Princeton University Press, 2008.
- [101] C. Kittel, *Introduction to Solid State Physics*, 7th ed. Wiley, 1995.
- [102] Y. Akahane, T. Asano, B.-S. Song, and S. Noda, “High Q photonic nanocavity in a two dimensional photonic crystal,” *Nature*, vol. 425, pp. 944–947, 2003.
- [103] —, “Fine tuned high Q photonic crystal nanocavity,” *Optics Express*, vol. 13, pp. 1202–1214, 2005.
- [104] M. Borselli, T. J. Johnson, and O. Painter, “Measuring the role of surface chemistry in silicon microphotronics,” *Applied Physics Letters*, vol. 88, p. 131114, 2006.
- [105] M. Settle, M. Salib, A. Michaeli, and T. F. Krauss, “Low loss silicon on insulator photonic crystal waveguides made by 193nm optical lithography,” *Optics Express*, vol. 14, pp. 2440–2445, 2006.
- [106] Y. Tanaka, T. Asano, R. Hatsuta, and S. Noda, “Investigation of point defect cavity formed in two dimensional photonic crystal slab with one sided dielectric cladding,” *Applied Physics Letters*, vol. 88, p. 011112, 2006.
- [107] P. Velha, J. C. Rodier, P. Lalanne, J. P. Hugonin, D. Peyrade, E. Picard, T. Charvolin, and E. Hadji, “Ultra high reflectivity photonic bandgap mirrors in a ridge SOI waveguide,” *New Journal of Physics*, vol. 8, p. 204, 2006.
- [108] T. P. White, L. OFaolain, J. Li, L. C. Andreani, and T. F. Krauss, “Silica embedded silicon photonic crystal waveguides,” *Optics Express*, vol. 16, pp. 17076–17081, 2008.
- [109] S. W. Jeon, B.-S. S. J.-K. Han, and S. Noda, “Glass embedded two dimensional silicon photonic crystal devices with a broad bandwidth waveguide and a high quality nanocavity,” *Optics Express*, vol. 18, pp. 19361–19366, 2010.
- [110] B.-S. Song, S.-W. Jeon, and S. Noda, “Symmetrically glass clad photonic crystal nanocavities with ultrahigh quality factors,” *Optics Letters*, vol. 36, pp. 91–93, 2011.
- [111] C. Manolatou, M. J. Khan, S. Fan, P. R. Villeneuve, H. A. Haus, and J.D.Joannopoulos, “Coupling of modes analysis of resonant channel add drop filters,” *IEEE Journal of Quantum Electronics*, vol. 35, pp. 1322–1331, 1999.

- [112] P. E. Barclay, K. Srinivasan, and O. Painter, “Nonlinear response of silicon photonic crystal microresonators excited via an integrated waveguide and fiber taper,” *Optics Express*, vol. 13, pp. 801–820, 2005.
- [113] I.-K. Hwang, G.-H. Kim, and Y.-H. Lee, “Optimization of coupling between photonic crystal resonator and curved microfiber,” *IEEE Journal of Selected Topics in Quantum Electronics*, vol. 42, pp. 131–136, 2006.
- [114] G. Shambat, B. Ellis, M. A. Mayer, A. Majumdar, E. E. Haller, and J. Vuckovic, “Ultra low power fiber coupled gallium arsenide photonic crystal cavity electro optic modulator,” *Optics Express*, vol. 19, pp. 7530–7536, 2011.
- [115] M. Grande, L. O’Faolain, T. P. White, M. Spurny, A. Dorazio, and T. F. Krauss, “Optical filter with very large stopband approximate to 300 nm based on a photonic crystal vertical directional coupler,” *Optics Letters*, vol. 34, pp. 3292–3294, 2009.
- [116] F. Morichetti, A. Melloni, M. Martinelli, R. G. Heideman, A. Leinse, D. H. Geuzebroek, and A. Borreman, “Box shaped dielectric waveguides a new concept in integrated optics,” *IEEE Journal of Lightwave Technology*, vol. 25, pp. 2579–2589, 2007.
- [117] S. L. Portalupi, M. Galli, M. Belotti, L. Andreani, T. Krauss, and L. O’Faolain, “Deliberate versus intrinsic disorder in photonic crystal nanocavities investigated by resonant light scattering,” *Physical Review B*, vol. 84, p. 045423, 2011.
- [118] C. J. Chen, J. Zheng, T. Gu, J. F. McMillan, M. Yu, G.-Q. Lo, D.-L. Kwong, and C. W. Wong, “Selective tuning of high Q silicon photonic crystal nanocavities via laser assisted local oxidation,” *Optics Express*, vol. 19, pp. 12 480–12 489, 2011.
- [119] P. Dong, W. Qian, H. Liang, R. Shafiqi, N.-N. Feng, D. Feng, X. Zheng, A. V. Krishnamoorthy, and M. Asghari, “Low power and compact reconfigurable multiplexing devices based on silicon microring resonators,” *Optics Express*, vol. 18, pp. 9852–9858, 2010.
- [120] M. R. Watts, W. A. Zortman, D. C. Trotter, R. W. Young, and A. L. Lentine, “Vertical junction silicon microdisk modulators and switches,” *Optics Express*, vol. 19, pp. 21 989–22 003, 2011.
- [121] A. W. Fang, E. Lively, Y.-H. Kuo, D. Liang, and J. E. Bowers, “A distributed feedback silicon evanescent laser,” *Optics Express*, vol. 16, pp. 4413–4419, 2008.
- [122] K. Nozaki, T. Tanabe, A. Shinya, S. Matsuo, T. Sato, H. Taniyama, and M. Notomi, “Sub femtojoule all optical switching using a photonic crystal nanocavity,” *Nature Photonics*, vol. 4, pp. 477–483, 2010.
- [123] R. A. Soref and B. R. Bennett, “Electrooptical effects in silicon,” *IEEE Journal of Quantum Electronics*, vol. 23, pp. 123–129, 1987.

-
- [124] H. Xu, X. Xiao, X. Li, Y. Hu, Z. Li, T. Chu, Y. Yu, and J. Yu, "High speed silicon mach zehnder modulator based on interleaved pn junctions," *Optics Express*, vol. 14, pp. 15 093–15 099, 2012.
- [125] X. Xiao, H. Xu, X. Li, Y. Hu, K. Xiong, Z. Li, T. Chu, Y. Yu, and J. Yu, "25 Gbit/s silicon microring modulator based on misalignment tolerant interleaved pn junctions," *Optics Express*, vol. 20, pp. 2507–2515, 2012.
- [126] S. A. Clark, B. Culshaw, E. J. C. Dawnay, and I. E. Day, "Thermo optic phase modulators in SIMOX material," *Proceedings of SPIE*, vol. 3936, pp. 16–24, 2000.
- [127] B. Huettl, R. Kaiser, W. Rehbein, H. Stolpe, C. Kindel, S. Fidorra, A. Steffan, A. Umbachl, and H. Heidrich, "Low noise monolithic 40 GHz mode locked DBR lasers based on GaInAsP/InP," *International Conference on Indium Phosphide and Related Materials*, pp. 633–636, 2005.
- [128] H. Park, A. W. Fang, R. Jones, O. Cohen, O. Raday, M. N. Sysak, M. J. Paniccia, and J. E. Bowers, "A hybrid AlGaInAs silicon evanescent waveguide photodetector," *Optics Express*, vol. 15, pp. 6044–6052, 2007.
- [129] G. Roelkens, J. Brouckaert, D. Taillaert, P. Dumon, W. Bogaerts, D. V. Thourhout, R. Baets, R. Ntzel, and M. Smit, "Integration of InP/InGaAsP photodetectors onto silicon on insulator waveguide circuits," *Optics Express*, vol. 13, pp. 10 102–10 108, 2005.
- [130] L. Chen, C. R. Doerr, L. Buhl, Y. Baeyens, and R. A. Aroca, "Monolithically integrated 40 wavelength demultiplexer and photodetector array on silicon," *IEEE Photonics Technology Letters*, vol. 23, pp. 869–871, 2011.
- [131] J. K. Doylend, P. E. Jessop, and A. P. Knights, "Optical attenuation in ion implanted silicon waveguide racetrack resonators," *Optics Express*, vol. 19, pp. 14 913–14 918, 2011.
- [132] D. A. B. Miller, "Optics for low-energy communication inside digital processors: quantum detectors, sources, and modulators as efficient impedance converters," *Optics Letters*, vol. 14, pp. 146–148, 1989.
- [133] T. Baehr-Jones, M. Hochberg, and A. Scherer, "Photodetection in silicon beyond the band edge with surface states," *Optics Express*, vol. 16, pp. 1659–1668, 2008.
- [134] H. Chen, X. Luo, and A. Poon, "Cavity enhanced photocurrent generation by 1.55 μm wavelengths linear absorption in a p i n diode embedded silicon microring resonator," *Applied Physics Letters*, vol. 95, pp. 171 111–171 113, 2009.

- [135] P. G. Kik, A. Polman, S. Libertino, and S. Coffa, "Design and performance of an erbium doped silicon waveguide detector operating at 1.5 μm ," *IEEE Journal of Lightwave Technology*, vol. 20, pp. 862–867, 2002.
- [136] A. Shakoore, "Silicon nanocavity light emitters at 1.3-1.5 μm wavelength," Ph.D. dissertation, University of St Andrews, 2013.
- [137] M. W. Geis, S. J. Spector, M. E. Grein, R. T. Schulein, J. U. Yoon, D. M. Lennon, S. Deneault, F. Gan, F. X. Kaertner, and T. M. Lyszczarz, "CMOS compatible all si high speed waveguide photodiodes with high responsivity in near infrared communication band," *IEEE Photonics Technology Letters*, vol. 19, pp. 152–154, 2007.
- [138] Y. Xu, Y. Li, R. K. Lee, and A. Yariv, "Scattering theory analysis of waveguide resonator coupling," *Physical Review E*, vol. 62, p. 7389, 2000.
- [139] T. Tanabe, H. Sumikura, H. Taniyama, A. Shinya, and M. Notomi, "All silicon sub Gb/s telecom detector with low dark current and high quantum efficiency on chip," *Applied Physics Letters*, vol. 96, pp. 101 103–101 103., 2010.
- [140] R. Hayakawa, N. Ishikura, H. C. Nguyen, and T. Baba, "Two photon absorption photodiodes in Si photonic crystal slow light waveguides," *Applied Physics Letters*, vol. 102, p. 031114, 2013.
- [141] D. F. Logan, P. Velha, M. Sorel, R. D. L. Rue, A. P. Knights, and P. E. Jessop, "Defect enhanced silicon on insulator waveguide resonant photodetector with high sensitivity at 1.55 μm ," *IEEE Photonics Technology Letters*, vol. 22, pp. 1530–1532, 2010.
- [142] D. Marpaung, C. Roeloffzen, R. Heideman, A. Leinse, S. Sales, and J. Capmany, "Integrated microwave photonics," *Laser & Photonics Reviews*, 2013.
- [143] J. F. Buckwalter, X. Zheng, G. Li, K. Raj, and A. V. Krishnamoorthy, "A monolithic 25Gb/s transceiver with photonic ring modulators and Ge detectors in a 130 nm CMOS SOI process," *IEEE Journal of Solid-State Circuits*, vol. 47, pp. 1309–1322, 2012.
- [144] D. A. B. Miller, "Energy consumption in optical modulators for interconnects," *Optics Express*, vol. 20, pp. A293–A308, 2012.
- [145] W. Bogaerts, S. K. Selvaraja, P. Dumon, J. Brouckaert, K. D. Vos, D. V. Thourhout, and R. Baets, "Silicon on insulator spectral filters fabricated with CMOS technology," *IEEE Journal of Selected Topics in Quantum Electronics*, vol. 16, pp. 33–44, 2010.
- [146] W. A. Zortman, A. L. Lentine, D. C. Trotter, and M. R. Watts, "Low voltage differentially signaled modulators," *Optics Express*, vol. 19, pp. 26 017–26 026, 2011.

- [147] H. Y. Ryu, M. Notomi, and Y. H. Lee, “High quality factor and small mode volume hexapole modes in photonic crystal slab nanocavities,” *Applied Physics Letters*, vol. 83, pp. 4294–4296, 2003.
- [148] T. Chu and N. F. nad M. Ishizaka, “Compact, lower power consumption wavelength tunable laser fabricated with silicon photonic wire waveguide microring resonators,” *Optics Express*, vol. 17, pp. 14 063–14 068, 2009.

List of Figures

- 1.1 World internet penetration rates by geographic regions [3]. 2
- 1.2 (a) Cross sectional SEM image of the Intel 45 nm technology process. The interconnect layers are divided into three regions: (a) Local, (b) intermediate and Global (reproduced from [9]). (b) Comparison of delays due to gate and interconnects at different technology nodes (data taken from [10]). The gate delay, also called propagation delay, corresponds to the time required for the output of a logic gate to make a transition from one stable state to another. With each successive technology nodes, as the device size and the gap between devices shrink, the gate delay and the delay due to local interconnect reduces. In contrast, the delay due to the global interconnect increases superlinearly. Global interconnects with repeaters can be incorporated to mitigate the delay but at the cost of more power consumption and chip area. (c) Dynamic switching power breakdown versus interconnect length (reproduced from [11]). Over 50 % of the dynamic power consumption results from the capacitance associated with the metal interconnection, whereas capacitance of the CMOS circuit (gate capacitance) contribute another 34 % and rest comes from the diffusion capacitance of the source and drain. The plot also reveals that the contribution of the interconnection to the total dynamic power consumption increases with increasing length of the interconnect. There are two power peaks, correlated with the total wiring. The peak at the shorter length is dominated by the gate and diffusion capacitance, while the second peak is mainly dominated by the interconnect capacitance. 4
- 1.3 Fabrication process of SOI: (a) SIMOX, (b) BESOI, (c) SmartCut 9
- 1.4 Sketch showing the relative size of a single mode fiber core (blue), wide access waveguides (yellow) and single mode photonic wires (red) in different materials. 12
- 1.5 (a) Grating coupler to an SOI wire waveguide, (b) Holographic lens coupler (reproduced with permission of the IEEE from [51], Copyright 2006), (c) Inverse taper to an SOI wire waveguide, (d) Cantilever coupler [54]. 13

1.6	(a) MZI modulator: when the refractive index difference between the two arms corresponds to π destructive interference occurs and as a result no light transmits to the output port (Off state), on the other hand when the refractive index difference is zero, constructive interference occurs and all the incoming light is transmitted to the output port (On state). (b) Resonance based modulator: when the resonance wavelength of the ring matches with the wavelength of the incoming light, light coupling to the drop port through the ring and no transmission occurs at the out put port (Off state). If the resonance wavelength of the ring is shifted by changing the refractive index, no coupling takes place and all the incoming light is transmitted to the output port (On state).	14
1.7	WDM system based on (a) broadband modulators, (b) ring resonator modulator [81].	17
1.8	Optical interconnect based on the vertically coupled photonic crystal cavity-waveguide system.	20
2.1	Photolithography process flow: (a) Sample is spun with photoresist (PR). (b) Sample is then exposed under UV light through a photomask. (c) In the case of positive photoresist, the exposed part is dissolved during the development. (d) For negative photoresist, the exposed part remains after development.	24
2.2	(a) Relationship between write field (WF) and minimum resolution. (b) Relative positions of the write fields with no stitching error and with stitching error, caused by imprecise positioning of the sample stage, respectively. (c) SEM image of a section of a bus waveguide with large stitching error.	26
2.3	Monte Carlo simulations of the electron distribution during (a) 10kV and (b) 20kV electron beam lithography (both reproduced with permission of the AIP from[90], Copyright 1975). (c) Example of proximity error correction for a photonic crystal cavity structure.	28
2.4	(a) Schematic of the RIE chamber. The gate valve connects the RIE chamber to a turbo pump and the butterfly valve controls the chamber pressure during the etch process. (b) SEM image of a photonic crystal etched with the optimized parameters. Observe the low side wall roughness and the straight side walls. (c) SEM image of a photonic crystal etched with increased RIE chamber pressure. Observe the angled side walls.	29
2.5	Lift-off process flow: (a) Sample is spun with LOR followed by S1818 photoresist. (b) Sample is exposed under UV light through a photomask. (c) Sample is developed in MF319, which washes away the exposed resist as well as the LOR creating an undercut. (d) Aluminium is evaporated onto the sample. (e), (f) S1818 and LOR is stripped of using solvent 1165 and acetone respectively.	31
2.6	Schematic of the thermal evaporator chamber	32

-
- 3.1 (a) A sinusoidal distribution of ε , where red denotes the higher ε region and blue denotes the lower ε region. Two possible mode distributions at $k = \pm\pi/a$ relative to the structure are also shown. Lower frequency tends to concentrate in the higher ε region and higher frequency tends to concentrate in the lower ε region. (b) Dispersion relation between ω and wavenumber k of a homogeneous one dimensional medium (solid blue lines), any assumed periodicity will replicate the dispersion relation at $k' = k + 2m\pi/a$ (dashed blue lines). (c) Dispersion relation of a real periodic variation of ε , where a photonic band gap (yellow region) is opened due to the splitting of the degeneracy at $k = \pm m\pi/a$. 36
- 3.2 Band diagram of a triangular lattice structure with background material index $n=2.8$ and hole index $n=1$. The band diagram is calculated for the wave vectors lying on the sides of the irreducible Brillouin zone (highlighted by yellow). The red and blue bands correspond to TE and TM polarizations respectively. 38
- 3.3 (a) A point defect cavity formed by removing one hole from an otherwise perfect two dimensional triangular lattice structure. (b) Due to the introduction of the defect, a new photonic band appears inside the band gap, which corresponds to the localized mode in the cavity. The bands corresponding to the perfect lattice are shown in green and the defect mode is shown in red. The dashed lines (known as light line) denotes the boundary between bound modes and radiation modes for a three dimensional structure (c) This point defect cavity has three trivial degenerate modes, corresponding to the three symmetry axes of the triangular lattice, one of them is shown here. 39
- 3.4 (a) Electric field distribution inside a cavity with rectangular envelope function and (b) spatial Fourier transform of the electric field. (c) Electric field distribution inside a cavity with Gaussian envelope function and (d) the spatial Fourier transform of the electric field. The blue area indicates the leaky region ($0 < k < n_{clad}2\pi/\lambda_o$). 41
- 3.5 Magnetic field (H_z) distribution of (a) the first order mode and (b) second order mode of an L3 cavity. (c) Profile of (a) along the center line of the cavity (red curve) and the profile of an ideal Gaussian envelope (dashed curve). (d) Profile of (b) along the center line of the cavity. 42
- 3.6 (a), (b) Electric field (E_y) distribution of the fundamental mode of an L3 cavity without and with displacement of air holes at both edges. (c), (d) The profile of (a) and (b) along the center line of the cavity (red curves) and the Gaussian fit (dashed curve). (e) and (f) 1D Fourier transform of the field profiles (red curves) with Gaussian fit (dashed curve). (reproduced with permission of the OSA from [103], Copyright 2005) 43

-
- 3.7 (a) A line defect in a triangular lattice formed by a missing row of air holes in the Γ -J direction. (b) The calculated band structure of (a). (c) Double heterostructure formed by assembling the basic PhC structures I and II with different lattice constants. (d) Schematic of the band diagram along the waveguide direction. (reproduced with permission of Macmillan Publishers Ltd: Nature Materials from [95], Copyright 2005). 45
- 3.8 (a) A line width modulated cavity created by shifting holes outwards in a W0.98 waveguide, where shift $d_A = x$, $d_B = 2x/3$ and $d_C = x/3$. (b) Shift in resonance wavelength and calculated Q-factors and mode volume for different values of x . The maximum Q-factor is achieved at about $x = 9\text{nm}$ with decreasing mode volume. (Reproduced with permission of the AIP from [73], Copyright 2006). 45
- 3.9 Dispersion adapted (DA) cavity with confined first order mode (E_y field). The shifted holes are denoted by green circles. Hole-shifts starting from h_0 in the first section to h_n in the last section (in this case 5 sections are used). The waveguide continues as a W1 after the last section. (b) Intensity profile of the first order mode $y=0$ with a Gaussian envelope function (red) overlaid. (c) Measured quality factors as a function of the standard deviation of the deliberate hole-diameter disorder for dispersion adapted cavity and heterostructure cavities. (Reproduced with permission of the IEEE from [96], Copyright 2012) 47
- 3.10 (a) k-space distribution of the first order cavity mode of an L3 cavity. The white and yellow circles correspond to the boundaries of the leaky region corresponding to the air- and oxide-cladding respectively. (b) Cross-sectional schematic of a completely SOG-clad photonic crystal structure (c) Cross-sectional schematic of a partially SOG-clad photonic crystal structure (d) SEM image of the same structure as in (c). 48
- 3.11 (a) The side coupling case, where a resonator is side coupled to a waveguide. (b) The resonant coupling case, where two waveguides are coupled by a resonator. 50
- 3.12 (a) A single mode resonator is coupled to a single mode waveguide. The dashed line represents the mirror symmetry axis. The solid lines represent the input and output reference plane. (b) The reflection (red) and transmission (blue) coefficients at resonance wavelength as a function of Γ_o/Γ_c 51
- 3.13 (a) An L3 cavity coupled to a photonic crystal waveguide. (b) K-space distribution along $ky=0$ before (blue) and after (red) the introduction of the waveguide. The gray region represents the leaky region. 53
- 3.14 (a) Schematic diagram of the optical filter, where a bus waveguide is vertically coupled to a photonic crystal cavity, b) Cross sectional view at the cavity region 55

-
- 3.15 Dominant electric field (E_y) profile of (a) the waveguide, (b) the photonic crystal cavity. K-space distribution of the dominant field (c) the waveguide, (d) the photonic crystal cavity. 56
- 3.16 (a) A standard triangular photonic crystal lattice with inter-hole spacing along the x-direction x and inter-hole spacing in y-direction y . (b) Real space field profile of a L3 cavity when the stretching/squeezing factor f is varied. (c) K-space distribution for different values of f . The yellow ellipses denotes the position of the high intensity regions of the waveguide mode. 57
- 3.17 Fabrication process: (a) A sample of SOI is cleaved from the wafer and covered in e-beam resist. (b) The resist is exposed with the photonic crystal pattern. (c) The pattern is transferred into the top silicon layer using a RIE etch and the remaining resist is removed. (d) The sample is covered in FOx and the FOx thickness is reduced to 200nm. (e) The sample is either spin coated with ZEP, or Si_3N_4 is deposited onto the sample. (f) ZEP/ Si_3N_4 waveguides are formed. 59
- 3.18 SEM image of (a) Dispersion adapted cavity. Although most of the field intensity of the cavity mode is confined inside the cavity region, extra 10 lattice periods are added on each side of the cavity to avoid any small leakage of light into the bulk silicon or air mode. (b) Cross-section of the device in the cavity region. 59
- 3.19 Experimental setup for measuring transmission and reflection spectra. OL: Objective lens, BS: polarization beam splitter, DUT: device under test, C: circulator, M: mirror, IR: infrared camera. 60
- 3.20 (a) Normalized transmission spectrum of the optical filter comprising a DA cavity and a ZEP waveguide. The two dips in the transmission spectrum correspond to the first two modes of the cavity. The inset shows the infrared images of the intensity distribution of the two modes. (b) Transmission and reflection spectra of the same system around the first cavity mode. (c) Normalized transmission spectrum of the optical filter comprising a linewidth modulated cavity and a Si_3N_4 waveguide. 62
- 3.21 K-space distribution of the dominant electric field (E_y) of (a) mode1, (b) mode2. Extinction ratio (blue squares) and k-space overlap intensity (red line) for different waveguide dimensions for (c) mode1, (d) mode2. 63
- 3.22 Overall quality factor (Blue circles) and intrinsic quality factor (Red squares) for different waveguide dimensions for (a) mode1, (b) mode2. (c) Resonance wavelength of the optical filter for different waveguide effective index. 64
- 3.23 Measured extinction ratio of the optical filter comprising of a DA cavity and Si_3N_4 waveguide as a function of stretch factor f . Inset shows the k-space distribution for different values of f . 65

- 3.24 (a) Five DA cavities in a single photonic crystal lattice. (b) The resonance wavelengths of each cavity are varied by tuning the position of the four innermost holes. (c) Normalized transmission spectrum at the Si_3N_4 waveguide output. Five dips in transmission correspond to the modes of the five cavities. 66
- 4.1 (a) A schematic representation of Off-state (no transmission) and On-state (complete transmission) in a resonance based modulator. (b) Transmission spectra of the filter when the refractive index is unperturbed (solid) and perturbed (dotted). 71
- 4.2 (a) Schematic of the device. The photonic crystal cavity and the Si_3N_4 waveguide are vertically coupled through an oxide layer. (b) Cross section of the device, consisting of a pin diode embedded into a photonic crystal cavity. (c), (d) Relative position of the intrinsic region of the pin diode with respect to the field distribution (E_y) of the first and second order modes respectively. 74
- 4.3 (a) Relative position of the photonic crystal cavity and the p^+ and n^+ doping regions. The green region shows the position of the vias. (b) The position of the metal electrodes with respect to the vias. (c) Dispersion adapted cavity. The shifted holes are represented by green circles. All five cavity designs are identical, except for the positions of the four innermost holes of each cavity, which were tuned to achieve the required resonance wavelength. (d) Dimension of the Si_3N_4 waveguide. (e) A complete view of the device containing all layers. 76
- 4.4 Fabrication process: (a) A sample of SOI is cleaved from the wafer. (b) The sample is selectively ion-implanted through doping windows in the photoresist. (c) The sample is annealed to activate both types of implanted ions. (d) Using e-beam lithography and dry etching, photonic crystal patterns are transferred to the silicon layer. (e) The sample is covered in FOx and the FOx thickness is reduced to 200nm. (f) Si_3N_4 waveguides are fabricated using e-beam lithography. (g) Electrical vias are etched through the FOx layer. (h) Electrical contacts are formed using lift-off. (i) Top view of the cascaded PhC cavity based modulator set, where five cavities are coupled to a single silicon nitride waveguide. 78
- 4.5 Experimental setup for optical measurements. OL: Objective lens, BS: polarization beam splitter, DUT: device under test, M: mirror, IR C: infrared camera, PMF: Polarization maintaining fiber. 80
- 4.6 Experimental setup for DC measurements. OL: Objective lens, BS: polarization beam splitter, DUT: device under test, M: mirror, PMF: Polarization maintaining fiber. 81
- 4.7 Experimental setup for the high speed data rate measurements. OL: Objective lens, BS: polarization beam splitter, DUT: device under test, M: mirror, Amp: Amplifier. 82

-
- 4.8 (a) Normalized transmission spectrum of the Si_3N_4 waveguide vertically coupled to five PhC cavities, where each dip corresponds to a different cavity (b) Resonance wavelength shift due to the tuning of four central holes of the cavities with respect to the reference cavity. (c) Change in extinction ratio (yellow triangles) and quality factor (green squares) due to the tuning of the four central holes of the cavities. 83
- 4.9 (a) IV characteristics of all the five cavity modulators. Since we are operating in injection mode, only region above 0V is shown. (b) Normalized transmission spectra around the resonance wavelength of the fifth cavity for different bias voltages. 84
- 4.10 Eye diagrams of the modulated optical output of the second modulator at (a) 0.5Gbit/s and (b) 1.0Gbit/s respectively. Horizontal scale: 1ns/div for 0.5Gbit/s and 200ps/div for 1 Gbit/s. 85
- 4.11 Eye diagrams at 0.5Gbit/s for all the five cavity modulators. Open eyes were observed for each channel. Horizontal scale: 1ns/div 86
- 4.12 (a) Normalized transmission spectrum of the bus waveguide with a tunable laser when each cavity is actively tuned to match the comb laser spectrum, (b) normalized transmission spectrum of the bus waveguide with the comb laser when cavity resonances are not aligned with the comb laser spectrum, (c) normalized transmission spectrum of the bus waveguide with the comb laser when cavity resonances are aligned with the comb laser, inset shows the comb laser spectrum 87
- 5.1 (a) Generation of an electron-hole pair when a photon with energy equal to or more than the bandgap energy is absorbed. (b) Process of electron-hole pair generation using a defect state within the bandgap when a sub bandgap energy photon is absorbed. Open and filled circles represent hole and electron respectively. 91
- 5.2 (a) Schematic of the device, where the defect implanted photonic crystal cavity and the bus waveguide are vertically coupled through a buffer layer. An arbitrary photonic crystal cavity is shown in the schematic for illustration purposes. The design of [96] is used in our experiment. (b) Theoretical plot of transmittance (T), reflectance (R) and optical loss (L) against Γ_o/Γ_c at resonance wavelength, using coupled mode theory. 94
- 5.3 Fabrication process: (a) A sample of SOI is cleaved from the wafer. (b) The sample is selectively ion-implanted through doping windows in photoresist. (c) The sample is annealed to activate both types of implanted ions. (d) Using e-beam lithography and dry etching, photonic crystal patterns are transferred to the silicon layer. (e) The sample is covered in FOx and the FOx thickness is reduced to 200nm. (f) Si_3N_4 waveguides are fabricated using e-beam lithography. (g) Electrical vias are etched through the FOx layer. (h) Electrical contacts are formed using lift-off. (i) Selective silicon implantation is done for creating the defect states. 95

- 5.4 Experimental setup for DC measurements. OL: Objective lens, BS: polarization beam splitter, DUT: device under test, CMP: coplanar metal probe, PMF: Polarization maintaining fiber. 96
- 5.5 The blue dashed curve shows the theoretical relationship between transmittance and optical loss of the system on resonance. The red dots show the measured photocurrents for five different detectors with different transmittances. The level of the red dots has been normalised to its maximum value, i.e. the graph highlights qualitative rather than a quantitative agreement. 97
- 5.6 Estimated optical spectra in the Si_3N_4 waveguide immediately after the cavity (blue) and measured photocurrent at photocurrent at 0V (red) and -10V (yellow) for the device with transmittance of 0.30. 98
- 5.7 (a) Measured photocurrent spectra for different input optical power at 0 V reverse bias. (b) Measured photocurrent peaks as the absorbed optical power increases. The solid line corresponds to a 7 mA/W responsivity and the dashed line shows the trend in photocurrent as the input power increases. (c) Shift in resonance wavelength as the absorbed optical power increases. (d) Measured photocurrent spectra for different applied reverse bias, when the input optical power is $55 \mu\text{W}$. (e) Measured responsivity (red circle) at resonance and dark current (blue square) as the reverse bias increases. (f) Shift in resonance wavelength as the applied reverse bias increases. 99
- 5.8 (a) Top view of the cascaded photonic crystal cavity based detector set, where two cavities are coupled to a single silicon nitride waveguide. (b) Normalized transmission spectrum (blue) of the system and measured photocurrent from detector 1 (red) and detector 2 (yellow dashed). 101
- 6.1 Electrical design for the depletion type modulator (a) simple pn junction, (b) interleaved pn junction 108

-
- 6.2 (a) Transmission spectra of a vertically coupled system for different input optical power taken under wavelength upswEEPing condition using a tunable laser. Dotted line shows the transmission spectrum for a “cold” cavity, i.e. the input power is small. Solid curve shows the transmission spectra for a “hot” cavity. Relatively large and asymmetric transmission dip in case of a hot cavity is an artifact of self-tuning effect. Process of temperature stability using self-tuning effect: (b) When the laser is set to a wavelength slightly longer than λ_C , see (c), a small amount of light is coupled into the cavity, resulting in a small amount of TPA and FCA. This redshifts the resonance (λ_H , the “hot” resonance) increasing the coupling of light into the cavity, resulting in further redshifting of the resonance. This continues until the resonance matches the laser wavelength (λ_L), see (d) and TPA and FCA are at a maximum. The resonance continues to redshift but now the amount of TPA and FCA starts to decrease as less and less light is coupled to the cavity. The system will quickly reach a steady state, with the heat produced by TPA and FCA matching the heat dissipated from the cavity. Should the resonance be red shifted further (due to change in temperature of the cavity environment), the heating effects will reduce and the cavity will experience a net cooling returning to the steady state. The electro-optic modulation, see (e), which happens at a nanosecond time scale, will not affect this steady state. 109
- 6.3 Schematic diagram showing the laser built around a reflective SOA and a narrow line-width Photonic Crystal reflector. A passive ring resonator is added on the output waveguide to enable direct modulation. 110

List of Tables

2.1	Spin coating recipe for different e-beam resists.	25
2.2	Development recipe for different e-beam resists. For SU-8 a post-exposure bake at 100°C for 2 minutes is necessary.	26
2.3	RIE recipes for different substrates.	30
3.1	Design parameters for the photonic crystal cavities (all the numbers in nm)	58
3.2	Design parameters for Y-stretched cavities	65
4.1	Description of the mask layers used for fabrication	75
6.1	A comparison of different low power WDM modulator techniques. For the channel numbers and spacings, in order to show the full potential of the various systems, the best case numbers are taken from the respective papers. Microdisk modulators are a powerful option, intermediate between the ring resonators and photonic crystal cavities in terms of mode volume and FSR. However, to our knowledge, cascadeability has not yet been demonstrated. *This is the area of each resonant component (with an allowance for trenches etc) or the total device area divided by the number of channels. **Defined here as the sum of the coupling loss and the loss in the demux/mux elements. Losses in the modulator are generally in the 3-5dB range [85], but strongly depend on the extinction ratio and energy/bit values used thus making a comparison based on this number difficult. NB For the non-resonant approaches, this loss is calculated assuming both a demultiplexing and multiplexing element. Losses in interfacing between the demux/mux and the modulators are also ignored in this case.	105